NASA TECHNICAL MEMORANDUM

NASA TM X- 64917

AN ANALYSIS OF SPACE ENVIRONMENT EFFECTS ON PERFORMANCE AND MISSIONS OF A SOLAR ELECTRIC PROPULSION STAGE (SEPS)

By Dave M. McGlathery
Preliminary Design Office
Program Development

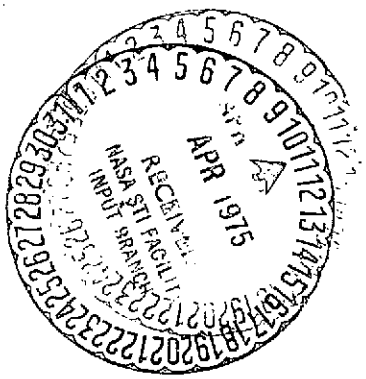

February 17, 1975

NASA

George C. Marshall Space Flight Center

Marshall Space Flight Center, Alabama

TECHNICAL REPORT STANDARD TITLE PAGE

1. REPORT NO.	2. GOVERNMENT ACCESSION NO.	3. RECIPIENT'S CATALOG NO.
NASA TM X- 64917		

4. TITLE AND SUBTITLE	5. REPORT DATE
An Analysis of Space Environment Effects on Performance and Missions of a Solar Electric Propulsion Stage (SEPS)	February 17, 1975
	6. PERFORMING ORGANIZATION CODE
7. AUTHOR(S)	8. PERFORMING ORGANIZATION REPORT #
Dave M. McGlathery	
9. PERFORMING ORGANIZATION NAME AND ADDRESS	10. WORK UNIT NO.
George C. Marshall Space Flight Center Marshall Space Flight Center, Alabama 35812	11. CONTRACT OR GRANT NO.
	13. TYPE OF REPORT & PERIOD COVERED
12. SPONSORING AGENCY NAME AND ADDRESS	Technical Memorandum
National Aeronautics and Space Administration Washington, D. C. 20546	14. SPONSORING AGENCY CODE

15. SUPPLEMENTARY NOTES

Prepared by Preliminary Design Office, Program Development

16. ABSTRACT

This report documents the development of an analysis which addresses the problems of degrading space environmental effects on the performance and missions of a Solar Electric Propulsion Stage (SEPS). A detailed study concerning the degrading effects of the Van Allen Belt charged-particle radiation on specific spacecraft subsystems is included, along with some of the thermal problems caused by electromagnetic radiation from the sun. The analytical methods used require the integration of two distinct analyses. The first, shown in Appendix A, is a low-thrust trajectory analysis which uses analytical approximations to optimum steering for orbit raising, including three-dimensional plane change cases. The second is the conversion of the Vette (NASA/Goddard Space Flight Center) time-averaged differential energy spectra for protons and electrons into a 1-MeV electron equivalent environment as a function of spatial position and thickness of various shielding materials and solar-cell cover slides. The analytical techniques, methods, and data presented in this report should be useful to SEPS mission and vehicular trade studies, with the objective being to arrive at an optimum vehicle design and mission model for a SEPS.

17. KEY WORDS	18. DISTRIBUTION STATEMENT
Earth orbital SEPS Planetary SEPS Low-thrust trajectories Radiation damage effects 1-MeV electron equivalent flux Shadowing effects	Unclassified-Unlimited Dave M. McGlathery

SECURITY CLASSIF. (of this report)	20. SECURITY CLASSIF. (of this page)	21. NO. OF PAGES	22. PRICE
Unclassified	Unclassified	99	NTIS

TABLE OF CONTENTS

LIST OF ILLUSTRATIONS

LIST OF ILLUSTRATIONS (Continued)

LIST OF ILLUSTRATIONS (Continued)

LIST OF ILLUSTRATIONS (Concluded)

LIST OF TABLES

TECHNICAL MEMORANDUM X-64917

AN ANALYSIS OF SPACE ENVIRONMENT EFFECTS ON PERFORMANCE AND MISSIONS OF A SOLAR ELECTRIC PROPULSION STAGE (SEPS)

INTRODUCTION

Solar electric propulsion development technology has demonstrated the potential use of a low-thrust Solar Electric Propulsion Stage (SEPS) as a key auxiliary spacecraft in providing economical and reliable space exploration and transportation during the next decade. The SEPS may be used to augment and enhance the payload delivery and retrieval capability of the Space Shuttle and Space Tug systems. Using high specific impulse ion thrusters and lightweight solar arrays for primary power, the SEPS has the potential to perform certain interplanetary space missions that are currently beyond the range of conventional chemical high-thrust rockets. Examples of some of these difficult missions include out-of-the-ecliptic flights, close probe missions, comet and asteroid rendezvous, and planetary orbital missions.

Earth-orbital applications for a SEPS include payload delivery and retrieval missions from intermediate Shuttle and Tug orbits (low earth orbit and geosynchronous missions), geosynchronous platform stabilization and payload maneuvering missions, and possibly (though less attractive) such missions as space debris collection and disposal.

Although the time required to perform low-thrust missions is greatly increased when compared with missions using conventional vehicles, and other operational and vehicle performance problems are encountered for some probable missions, solar electric propulsion technology and mission analysis studies strongly support the development and use of a solar electric propulsion vehicle.

A. Purpose and Scope

The purpose of this report is to analyze the performance of a SEPS while it is being subjected to the degrading effects of the natural space environments over a range of possible SEPS missions. A detailed and extensive analysis

concerning the degrading effects of the Van Allen Belt charged-particle radiation on specific spacecraft subsystems is included, along with some of the thermal problems caused by electromagnetic radiation. Other environments which may impact the performance of the SEPS are magnetic fields, solar wind, solar flares, micrometeoroids, and planetary environments, as well as some of the induced environments created by the spacecraft.

Most of the data included was developed as referenced from Marshall Space Flight Center (MSFC) in-house solar electric propulsion studies and activities. Some of the data was obtained during a NASA tri-center [MSFC, Lewis Research Center (LeRC) and Jet Propulsion Laboratory (JPL)] Solar Electric Propulsion/Advanced Systems Technology (SEP/AST) development activity. Other NASA contractual solar electric propulsion studies were an additional source for some of the data included herein.

This report is not intended to impose performance and/or environmental design requirements on either the SEP/AST development programs or other specific SEPS preliminary design activities. However, the information, data, and analyses included should be extremely useful to the development of a preliminary design of a SEPS.

Since a defined probable mission set for the SEPS is tentative and subject to further changes, this report will focus on a wide range of possible SEPS missions, both earth-orbital and interplanetary. Considerable attention is given to presenting the performance and environmental data in a form that is specifically applicable to SEPS design trade analyses. For instance, the effects of the natural environment on the SEPS is strongly mission-dependent. Consequently, it is necessary to integrate unique environmental modeling and trajectory analyses to assess possible degradation effects of the natural space environment on the SEPS solar arrays and thruster subsystem components during specific missions.

Using these methods, mission and vehicle trade studies may be performed to aid in arriving at an optimum vehicle design and mission model for a SEPS.

Techniques and methods employed for analytical approximations to optimum low-thrust steering for the SEPS earth-orbital applications are presented in Appendix A.

B. SEPS Mission Model

The environmental design and performance data will cover the following tentative or preliminary mission model:

1. Earth Orbital Mission Options
   a. Earth Orbital Engineering Test Flight (1982)
   b. Geosynchronous delivery and retrieval
   c. Geosynchronous satellite servicing
   d. Low-orbit delivery and retrieval
   e. Low-orbit satellite servicing
2. Planetary Mission Options
   a. Encke Slow Flyby (1979)
   b. Out-of-Ecliptic (1979)
   c. Encke Rendezvous (1981)
   d. Jupiter and Mercury Orbiter (1982 and 1987)
   e. Venus Radar Mapper (1983)
   f. Saturn Orbiter/Probe (1985)
   g. Asteroid Rendezvous (1986)

SECTION II. APPLICABLE ENVIRONMENTS

The predicted space environments for the SEPS are grouped into two basic categories:

1. Cruise Environments
   a. Natural
   b. Induced
2. Planetary Encounter Environments
   a. Natural
   b. Induced

A. Cruise Environments

1. NATURAL CRUISE ENVIRONMENTS

Natural cruise environments are of concern to the SEP/AST development and mission design programs and have been singled out to receive extensive attention in this report. This is because the SEP/AST efforts deal primarily with new and, in many cases, undemonstrated technology areas with regard to reliability and performance which meet projected baseline requirements imposed by certain mission design considerations. For instance, the SEPS solar arrays as presently configured are especially sensitive to a charged-particle environment with regard to the degradation rates of the solar cells. Thermal problems that affect operating and survival temperature extremes are also of primary concern for some missions. An additional challenge is offered by the fact that low-thrust mission, performance, and trajectory optimization analyses which must proceed concurrently with vehicle design concepts are a significantly more complex problem than analyses required for high-thrust conventional space vehicles. Consequently, each additional parameter, for which optimization methods have to be considered, add to an analysis problem which is already time consuming.

The following sections will focus on those natural cruise environmental parameters impacting the performance of a SEPS and will provide specific preliminary inputs for vehicle design/mission/performance trade studies and analyses. The specific natural cruise environment addressed will include

a. Charged Particles

b. Electromagnetic Radiation and Thermal Control

c. Pressure

d. Cometary and Asteroidal Meteoroids

e. Magnetic Fields

a. Charged Particles. The charged particles include magnetically trapped electrons and protons, solar flare proton events, solar wind, and galactic cosmic radiation.

(1) Magnetically Trapped Electrons and Protons.

(a) Damaging effects of Van Allen radiation. Magnetically trapped protons and electrons are always present and their effects upon astronauts, spacecrafts, and payload will have to be considered, to a greater or lesser degree, dependent upon the configuration of the spacecraft, the nature of the payloads, and various mission and orbital parameters. Some of the references used for this study contain certain analyses and data which address the effects of these environments on previous and future NASA-sponsored missions. This section will include some general data as required for a cursory appreciation of the total problem but will focus primarily on how these charged-particle environments impact the SEP/AST development programs and other SEPS preliminary design and payload/mission study activities.

The direct applicability of any presented data is determined by whether it is in the form required by the user. Radiation analysis data are available in a variety of forms and, in many instances, one needs only to be aware of the pertinent reference. Because of the new technology areas employed by the development and use of a SEPS, much of the radiation analysis data needed for spacecraft design and mission planning is not available in the form that provides the most beneficial and efficient use of the data. The data presented in this section should improve upon the solution but are not complete enough to solve the problem because the state-of-the-art in some of the analysis areas is still being improved.

Some examples of the available forms of magnetically trapped space radiation as a function of various orbit parameters include (1) flux intensities at a point, (2) differential and integral energy spectra at a point, (3) time-averaged differential and integral spectra over the mission, (4) total number

of particles encountered above specified energies, (5) dose rates behind various thicknesses of materials and geometric configurations, and (6) 1 MeV electron equivalence conversion of the proton and electron environment as a function of varying cover slide (shield) thicknesses and orbit parameters. Thus, it is obvious that the user will have to know in what form he requires the data. Specific graphs, tables, and references are included in this section with details and explanations of the above-listed forms.

Electronic instruments, film, solar arrays, thermal and adhesive coatings, and other fabrication materials are sensitive to and adversely affected by the magnetically trapped charged-particle environments. Most conventional electronic devices can tolerate very large doses before serious degradation of performance results for mission lifetime up to 1 year. However, the kind of mission lifetimes considered for the SEPS range up to 5 years. Consequently, all components of the stage will have to be designed with these possible degradation effects in mind.

(b) Methods used in laboratory evaluation of damaging effects to solar cell. The charged-particle environment, as it affects the preliminary design of hardware development and mission planning, is the primary interest of this section. The behavior of solar cells in a radiation environment as discussed in Reference 1, can be described in terms of the changes in the designed engineering output parameters of the cells such as current, voltages, and efficiencies of the devices. Laboratory evaluation of the effects of space radiation on solar cells requires charged-particle accelerators such as the Van de Graaff electrostatic dynamatron, linear electron, and cyclotron accelerators. All electron energy ranges of interest and proton energy ranges of up to 600 MeV may be obtained with these accelerators. Accelerator use in some instances may represent an "overkill" as far as testing is concerned and some real-time irradiation of solar cells has been done using beta emitting sources, which generate a spectrum of electron energies and fluxes similar to that of some space environments.

The major types of radiation damage phenomena in solids which are of interest to the solar-array designer are ionization and atomic displacement. The intensity of ionization is measured in terms of the roentgen. Ionizing radiation may also produce darkening effects in cover slide coatings and adhesives, which results in a reduction in the light transmittance properties of these materials. The use of silicon dioxide as surface coatings and the presence of dielectric materials in silicon used in solar cell manufacturing are the reasons for a wide range of ionization-related radiation effects in solar cells. The development of trapped charges in these oxides may cause increased

leakage currents, decreased gain, and surface channel development in bipolar transistors and increased threshold voltage in metal oxide semiconductor (MOS) field effect transistors. Radiation damage by atomic displacement results in permanently degraded silicon solar cells. Damage is due to the displacement of silicon atoms from their lattice sites by fast charged particles. The usual practice in the study of solar-cell damage is to monitor changes in the output parameters of cells such as short-circuit current, open-circuit voltage, and maximum power while the cell is being irradiated with known spectra of charged particles.

Laboratory testing of irradiated solar cells using various energy spectra of electrons and protons has produced a wide variation in the relative damage effects on measured cell output parameters. For example, if a given 10-MeV electron fluence degrades a solar cell to a specific state of damage, then a 1-MeV electron fluence 16 times greater may be required to produce the same specific state of damage. Thus, the concept of damage-equivalent 1-MeV electron fluence is used and may be extended to define the relative effects of proton irradiation. The problem is more complex with protons, however, since the range of proton energies below 5 MeV is less than the thickness of most solar cells. As a result, low-energy protons are deposited in the cells, providing greater and more nonuniform damage than the higher-energy protons which pass through the cells. The type of solar cell to be considered first in these analyses is an N/P-type conventional silicon cell. The N/P has reference to specific characteristics of the silicon semiconductor whether positive or negative with regard to the relative concentration of conduction electrons and holes as charge carriers. Protons in the energy range from 1.5 to 3 MeV produce a maximum in relative radiation damage in N/P silicon solar cells as shown in Figure 1, which is taken from Reference 1. The importance of a cover slide several mils thick becomes apparent, since the proton energies that do the most damage are effectively removed from the environment by the stopping power potential of the cover slide.

A further complication of the problem would occur with the SEPS operating in a Van Allen radiation environment where there is a high intensity of protons greater than 5 MeV. Depending upon cover-slide thickness and the time spent in such an environment, these higher-energy protons are slowed as they traverse the shielding materials, thus becoming low-energy protons with a higher degradation potential as they reach the active region of the cell proper. Work is continuing on this complicated analysis problem and as results are obtained, the radiation models used at present will be updated.

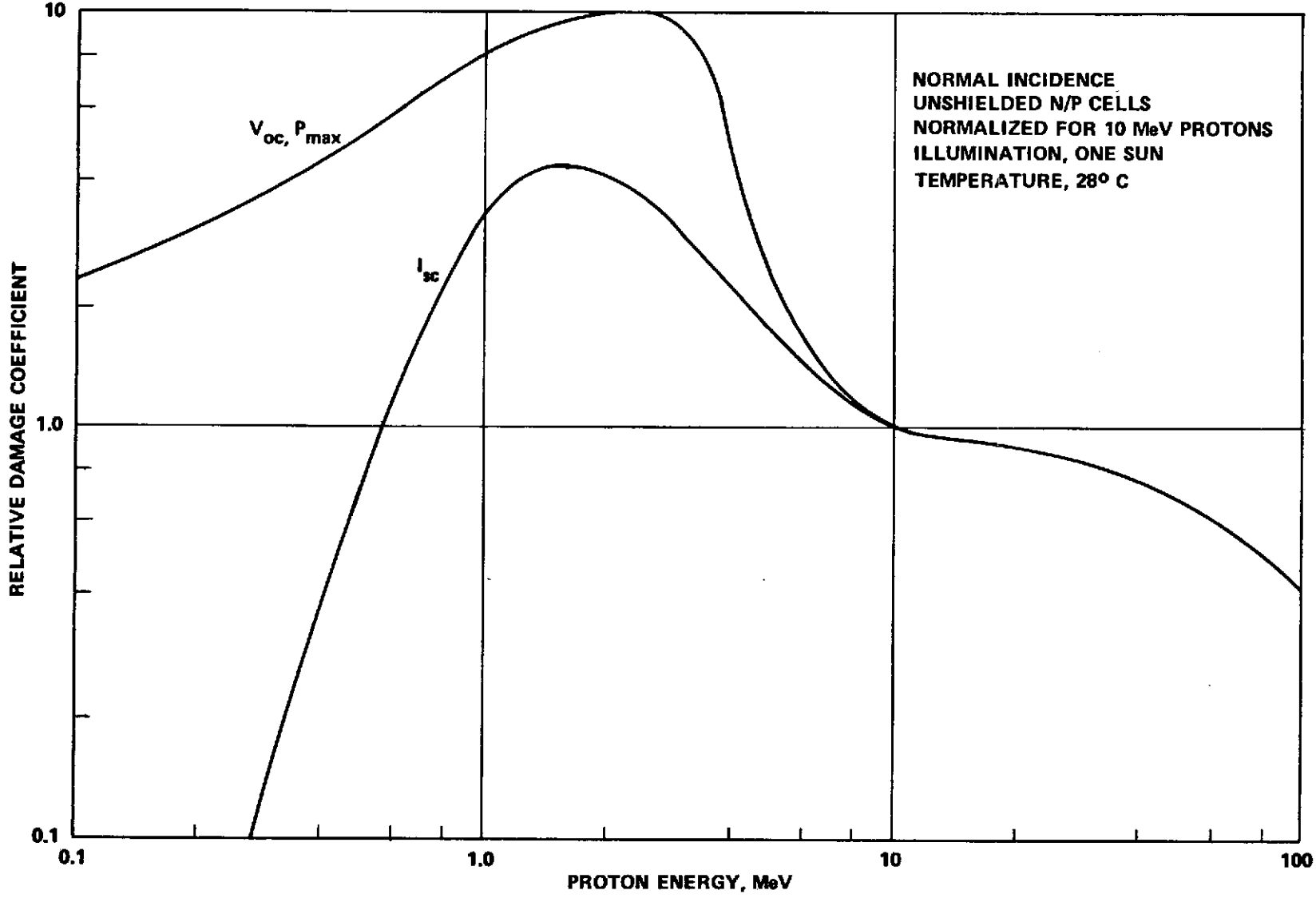

Figure 1. Relative damage coefficient for proton irradiation of N/P silicon solar cells (V_{oc} — open-circuit voltage, I_{sc} — short-circuit current, P_{max} — maximum power).

(c) Conversion of space radiation to a laboratory-determined 1-MeV electron equivalent fluence. To assess the probable damage to solar cells caused by space radiation encountered on a specific SEPS mission, it is necessary to be able to equate various spatial charged-particle energy spectra to radiation environments which can be produced under laboratory conditions. Thus, the concept of space radiation damage equivalence arises. The use of damage equivalent fluence methods involves two separate problems. One is to adequately describe the degradation of an unshielded silicon solar cell undergoing 1-MeV electron irradiation under laboratory conditions, i.e., normal incidence. The second problem is to reduce the effects of magnetically trapped protons and electrons with varying energy spectra and isotropic incidence to a normal incidence 1-MeV electron damage equivalent fluence. This transformed composite 1-MeV electron equivalent fluence produced by the Van Allen radiation belts, solar flare protons, solar winds, and galactic cosmic rays also becomes a function of various cover-slide or shield thicknesses which cover the silicon solar cells. As newer, more efficient, radiation-resistant solar cells are developed, these analyses and laboratory experiments will have to be updated accordingly.

Other factors which are significant in determining the performance of a solar cell in a radiation environment are cell thickness (not cover-slide thickness) and base resistivity of the particular cell. Current N/P solar-cell usage is confined to base resistivity ranges of 1 to 3 Ω•cm and 7 to 13 Ω•cm. Cells in the base resistivity range of 1 to 3 Ω•cm have greater initial maximum power output. However, 7- to 13-Ω• cm cells have greater maximum power output after high-electron fluences are reached. Notwithstanding, the 1- to 3-Ω•cm cells produce greater maximum power at lower fluences. Solar-cell thickness has been known to have a strong effect on the output parameters of irradiated cells. A thin solar cell (8 mils or less) degrades less at lower electron fluences with regard to retention of initial maximum power but is less efficient than the thicker 10- and 12-mil cells. Consequently, while it is desirable from a weight standpoint to use thin solar cells for the SEP/AST solar-array development programs, baseline requirements are subject to tradeoffs with regard to weight, efficiency, and other performance factors for a SEPS operating in a charged-particle environment.

(d) Relative performances of the high-efficiency violet solar cells and other conventional silicon cells. The COMSAT violet solar cell [2] and other higher-efficiency cells being developed and tested by the Centralab and Heliotek Corporations should be considered as candidate baseline cells for the SEPS solar array. Some of these cells have been flight-qualified, and their relative performances as compared with conventional silicon cells are now being monitored by NASA/Goddard Space Flight Center (GSFC), NASA/LeRC, Hughes Aircraft Company, and the Naval Research Laboratory (NRL).

The violet cell is manufactured using a refined silicon and responds to a shorter wavelength range (below 0.4 μm) than do conventional cells. Laboratory tests have demonstrated an average efficiency of 12.84 percent compared with an average of 10.0 percent for conventional cells and a power output of up to 20 percent more than a conventional panel.

Actual flight data[1] from the GSFC experiment, Interplanetary Monitoring Platform (IMP-J), launched in October 1973, show an initial 12.5-percent power increase for the violet cell panel compared with the conventional cell panel. Through June 1974, the violet panel shows a degradation from all causes of 3.4 percent whereas the conventional panel shows a degradation of 3.9 percent. Through January 1975, no significant further degradation had been observed in either of these experiments. The orbit of the IMP-J experiment is circular at approximately 200 000 km (100 000 n.mi.). The charged-particle radiation environment is quite soft at this distance, especially during quiet sun conditions where there is an absence of significant solar-flare activity. Consequently, actual flight data concerning violet-cell performance in a hard charged-particle environment are not available from this experiment. The initial degradation was probably caused by the solar ultraviolet spectrum.

During laboratory testing the violet cell seems to maintain much of its superior performance in most categories, i.e., humidity tests, thermal soaks and cycling, tape peel, etc. However, the violet cells degrade faster under conditions of electron and proton irradiation.

According to data presented in Reference 3 which compares the performance of the COMSAT violet cell with the performance of conventional INTELSAT IV cells, the COMSAT cells lose a significant percentage of their relative initial power increase under high electron fluences. An initial power advantage of 16 percent by the COMSAT cells is reduced to 14 percent for an electron irradiated fluence of 3×10^{14} e/cm^2 on both types of cells. At an electron fluence of 10^{15} e/cm^2, the violet-cell power output is only 12-percent better than the conventional cells, and at a fluence of 5.4×10^{15} e/cm^2, the power output advantage of the violet cell is reduced to 7.5 percent. This means that for spacecraft operations at the same altitudes in the Van Allen radiation belts, the COMSAT violet cell could lose a great deal of its performance advantage in a relatively short time.

---

1. Information received through private communication from NASA/GSFC.

Recent preliminary data taken from actual flight experiments onboard the NRL's Timation III-A satellite[2] tend to confirm the theoretical and laboratory evaluation of the expected performance of various types of conventional and high-efficiency violet cells while operating in a charged-particle environment. These results are summarized in Table 1. The Timation satellite is a retrograde near-circular orbit at an altitude of approximately 14 000 km (7500 n.mi.) and an inclination of 125 deg (analogous to a 55-deg inclination for Van Allen radiation data projections). Solar-cell performance data from this particular orbit should be useful in projecting the expected performance of SEPS solar arrays because the 7500 n.mi. altitude is also an estimated minimum changeover altitude for combination Tug-SEPS missions to geosynchronous orbit [35 784 km (19 322 n.mi.)].

An interesting phenomenon is observed from Table 1, which shows that after 10 days in orbit the magnitude of power levels per cell are significantly higher than the laboratory projections of these power levels. This is partially explained by the differences in the sun's actual electromagnetic spectra and the laboratory solar simulator. It is also possible that initial charged-particle bombardment will cause some short-term fluctuations or pulsations in the monitored output parameters of these cells. Consequently, if the power degradation rates are computed with respect to the laboratory-simulated power levels, the relative degradation in performance for these cells would not show such a steep decline.

Data from the IMP-J experiment and other similar experiments, including the NRL Timation III-A experiment and other related studies, will continue to be monitored for definitive trends in relative solar-cell performance.

(e) Computer software utilization associated with performing trade studies to determine optimum trajectory/mission/vehicle concepts for a SEPS operating in a charged-particle environment. Trajectory and orbital analyses associated with data-generation techniques depicting the effects of the trapped charged-particle environment on space flights and spacecraft vary between investigators. This section will focus on those techniques employed at MSFC to generate preliminary mission-dependent environmental data useful to the SEP/AST development programs and other SEPS in-house and contractual preliminary design and mission analyses activities.

The geomagnetic field around the earth forms a "magnetic pocket" known as the magnetosphere, whose boundary is determined by the solar wind, which is assumed to be a radial expansion of the sun's corona. A distortion in this

2. Information received through private communication from the NRL.

TABLE 1. PRELIMINARY PERFORMANCE DATA FOR CONVENTIONAL VERSUS HIGH-EFFICIENCY VIOLET SOLAR CELLS FROM ACTUAL FLIGHT EXPERIMENTS ONBOARD THE NRL TIMATION III-A SATELLITE

	Relative Power Output			
Solar-Cell Type	Maximum Expected Normalized* Power per Cell from Laboratory Simulation	Normalized Power After 10 Days In Orbit	Normalized Power After 105 Days In Orbit	Percent Power Degradation After 105 Days In Orbit
Conventional 2-Ω·cm 12-mil Fused Silica Cover Slide	1	1.07	0.93	12.5
Spectralab (Helios) 6-mil Fused Silica Cover Slide	1.22	1.20	1.12	6.6
COMSAT Violet 6-mil Ceria-Doped Microsheet Cover Slide	1.30	1.46	1.27	12.6
Centralab Violet 6-mil Ceria-Doped Microsheet Cover Slide	1.19	1.28	1.17	8.2

*Normalized to a maximum power output of 1.0 (57.0 mW per cell) for the conventional 2-Ω·cm solar cell obtained from laboratory simulation of the sun's electromagnetic spectra.

geomagnetic field results in a low-altitude region called the South Atlantic Radiation Anomaly where relatively high trapped particle fluxes exist. For low earth orbiting spacecraft, damage will be caused by continuously passing through this anomaly. Methods used to model this environment are shown in References 4 and 5. To shorten the data illustrations, the proton environment will be emphasized since in most instances those particles produce the greatest amount of concern for the SEPS. Similar data may be generated for the trapped electron environment as referenced above and, in fact, the composite 1-MeV electron equivalent space radiation modeling by Burrell and Wright[3] includes contributions from both the electron and proton environments.

Figure 2 shows the proton isoflux contours, which expand with altitude, at a distance of 926 km (500 n.mi.). Particle flux intensity over all space is a function of altitude and inclinations. Since this anomaly remains essentially stationary with respect to the rotating earth, the amount of time spent in this region and the number and flux intensities of protons encountered are a function of the particular orbital parameters of the spacecraft or payload. Using trajectory generation methods depicted in Reference 5, Figure 3 shows the increased particle accumulation rate as a function of circular orbit altitude at a constant inclination of 28.5 deg.

For relatively low earth orbits, it is possible to significantly reduce the encountered flux intensities by varying the inclinations and/or altitude of an orbit or by reorienting orbits of constant semimajor axes and inclinations with respect to the location of the perigee and apogee points of the orbit. Figure 4 shows the effects of such a reorientation. The purpose is to place the perigee point in the southern hemisphere where the anomaly will intersect an orbit at a lower altitude. When the altitude is greatest, the spacecraft or payload will not be in hot regions very long. The point is to be able to increase the altitudes of eccentric orbits without increasing the damaging effects of constant passes through the South Atlantic Anomaly. This type of orbit is more advantageous when the perigee motion is negligible.

When the long-term effects of hazardous space radiation are assessed, time-averaged fluxes and energy spectra may be more meaningful than instantaneous data at a point. These time-averaged data may be generated as shown in References 4 and 5. Curve A of Figure 5 shows time-averaged values for

3. M. O. Burrell and J. J. Wright, Radiation Environment and Solar Cell Degradation Data, MSFC technical letters S&E-SSL-NR (ES44), Sept. 28, 1973, and May 6, 1974; (shown in Figures 8 through 11).

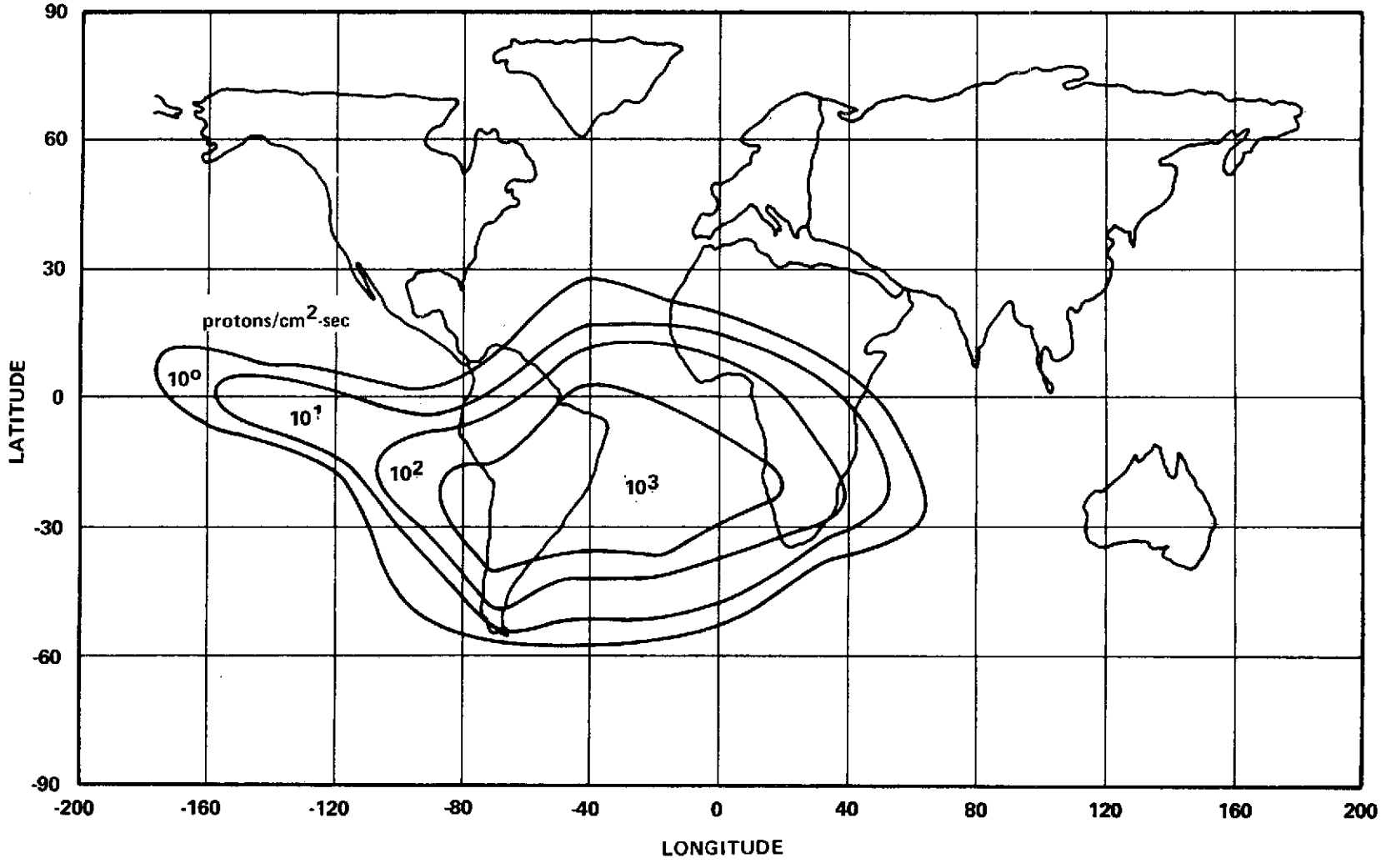

Figure 2. Proton isoflux contours at altitude of 926 km — South Atlantic radiation anomaly producing total proton flux greater than 50 MeV (AP7 data).

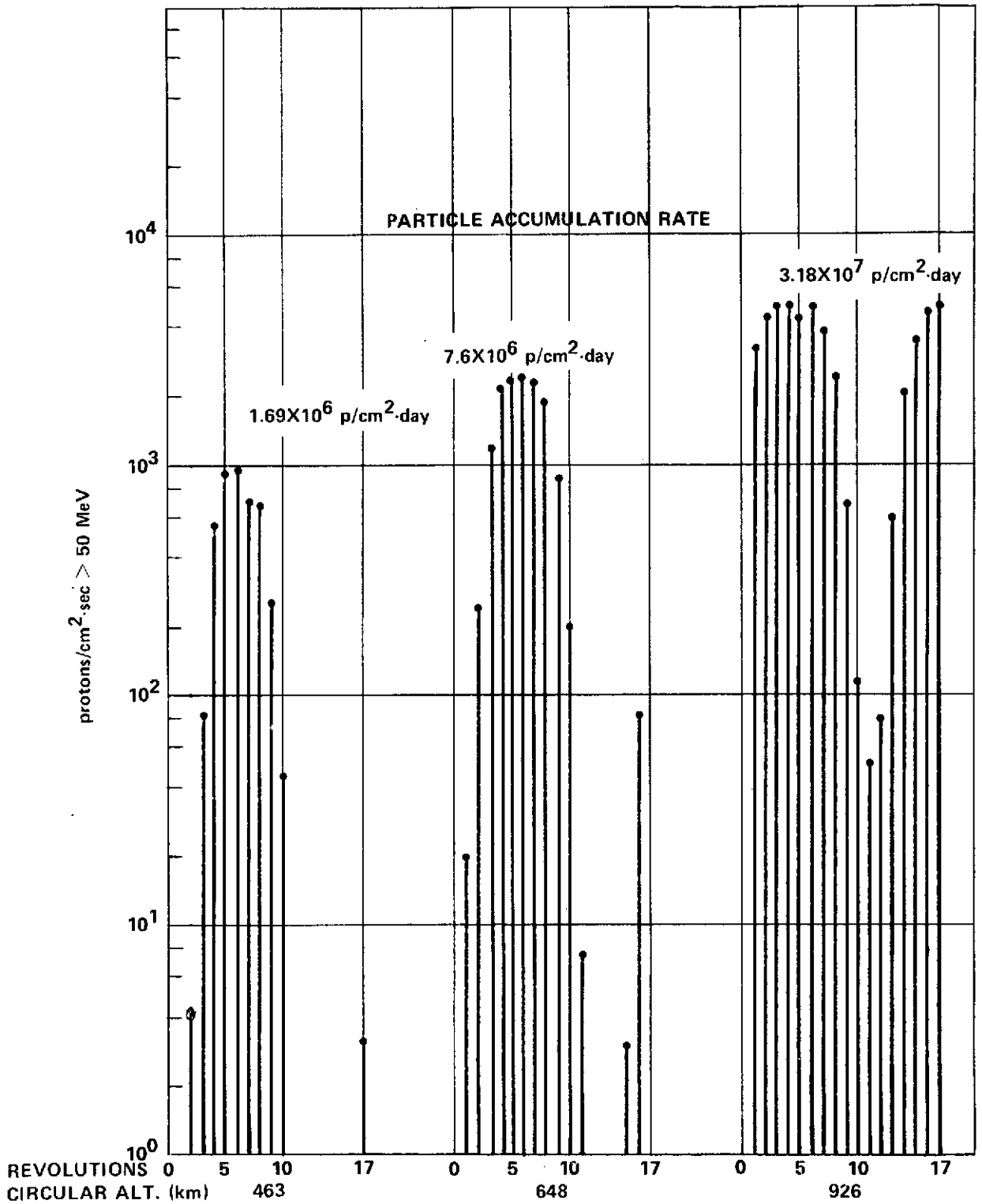

Figure 3. Maximum proton flux intensities encountered per revolution and particle accumulation rate for indicated altitudes at 28.5-deg inclination (AP7 > 50 MeV).

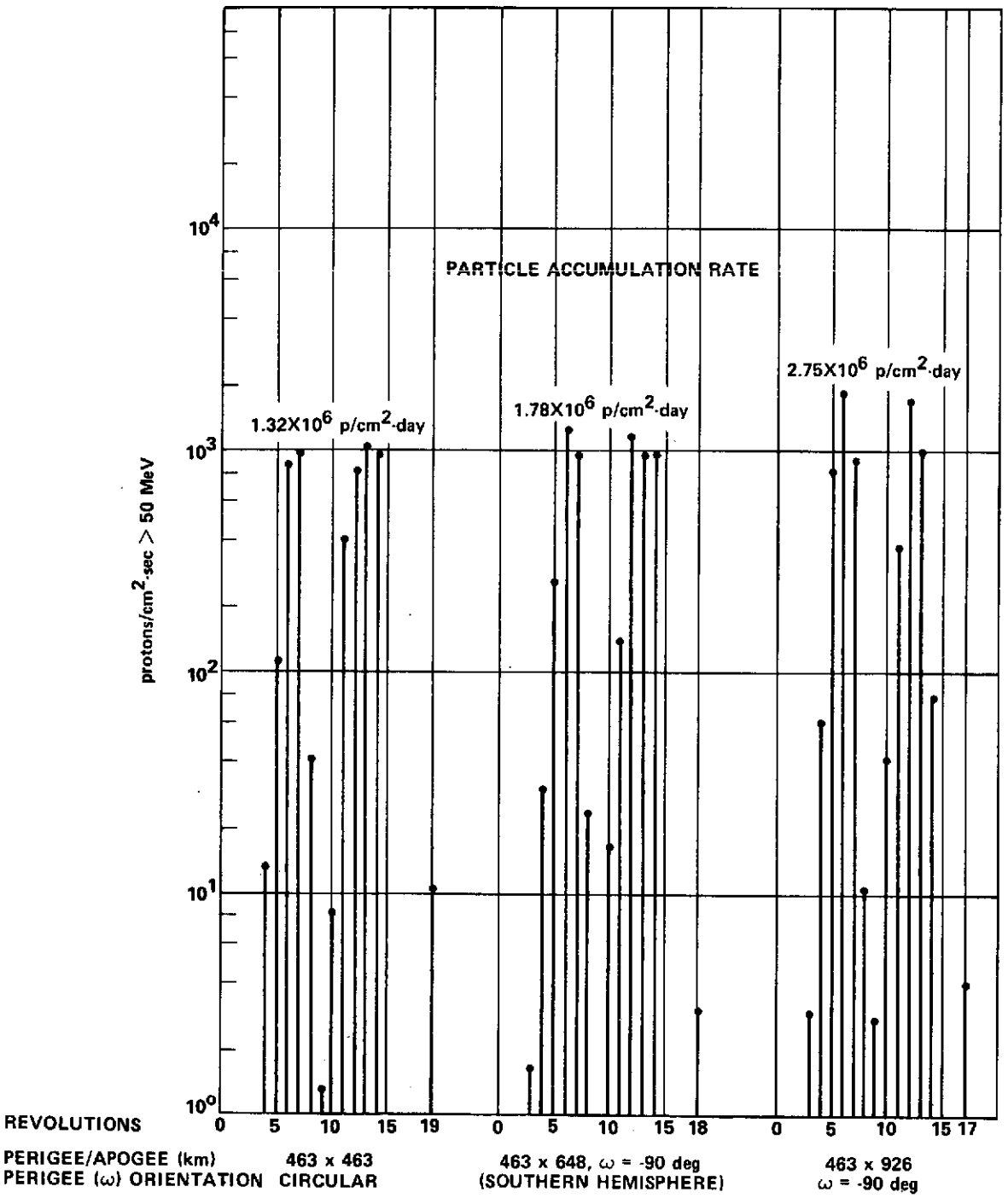

Figure 4. Maximum proton flux intensities encountered per revolution and particle accumulation rate for indicated orbital parameters and 56-deg inclinations (AP7 > 50 MeV).

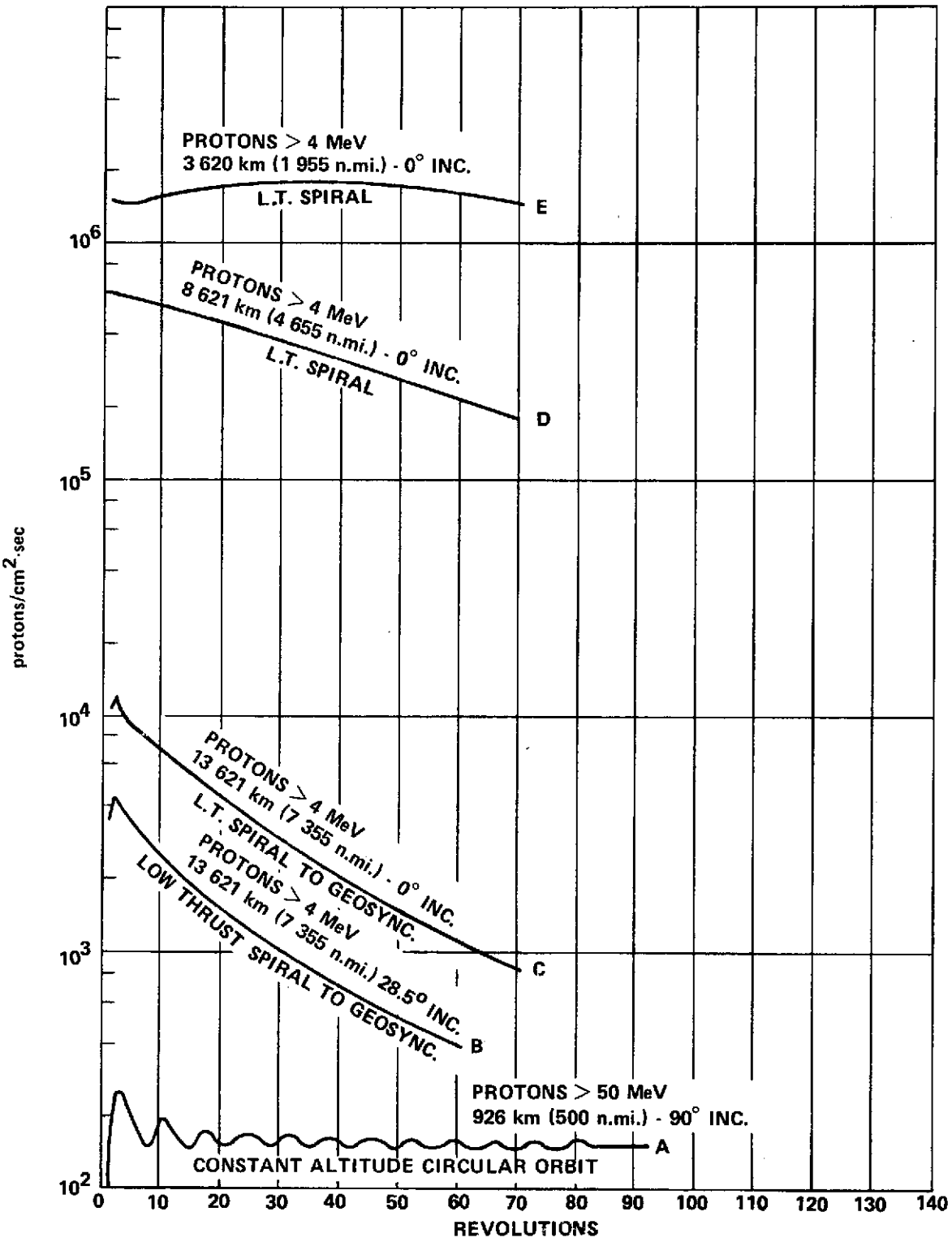

Figure 5. Time-averaged proton flux encountered for typical low-thrust (SEPS) trajectories beginning with initial conditions as indicated (AP6 > 4 MeV and AP7 > 50 MeV proton data).

protons greater than 50 MeV for a constant circular polar orbit altitude of 926 km (500 n. mi.). Over an adequate number of revolutions, these values converged as shown and from such data time-averaged differential and integral energy spectra may be extracted.

(f) Unique problems and solutions associated with low-thrust vehicle performance evaluation. Low-thrust spiraling SEPS trajectories do not readily adhere to the conventional analyses employed for circular coasting orbits with regard to generating time-averaged energy spectra of incident particles. One obvious reason is that at least the altitude and perhaps other orbital parameters of the spiral are not constant long enough for these time-averaged values to converge. This is particularly true for higher initial orbits and lower payload weights, in which case the rate of altitude increase is relatively high.

Using methods and analyses illustrated in Reference 5, an MSFC letter by this author,[4] and Appendix A, curves B, C, D, and E of Figure 5 show the effects of attempting to generate time-averaged proton energy spectra for a simulated SEPS low-thrust trajectory starting from various initial altitudes. The following are the reasons that curve E of Figure 5 seems not to vary as rapidly as the others: (1) at lower altitudes, the rate of orbit raising is slower, and (2) the proton environment peaks in intensity in this region. This type of data could be segmented for a given number of revolutions and reasonable approximations to time-averaged data possibly could be obtained.

Figure 6 shows time-averaged differential and integral energy spectra for protons greater than 50 MeV using the conventional circular-orbit constant-altitude method extracted from the results of curve A, Figure 5. These spectra are explained in detail in References 4, 5, and 6. After a representative time-averaged differential spectrum is obtained as illustrated in Figure 6, these data are then applicable to a charged-particle radiation transport analysis, explained in Reference 4, to arrive at dose rates (rads or roentgens) as a function of material densities and measured thickness for specific altitudes and inclinations.

For some specific increments of altitudes and inclinations, these time-averaged differential fluxes were tabulated, as used in References 4 and 5, by Dr. James I. Vette, et al., of the GSFC [6, 7]. These may be used directly as input into the transport analysis codes, discussed in Reference 4, to produce a dose rate table as shown in Figure 7.

4. D. M. McGlathery, Earth Orbital SEPS Performance Data Considering Trajectory Interaction with Solar Cell Degradation from Van Allen Radiation, MSFC technical letter S&E-AERO-GA-73-75, Jan. 4, 1974.

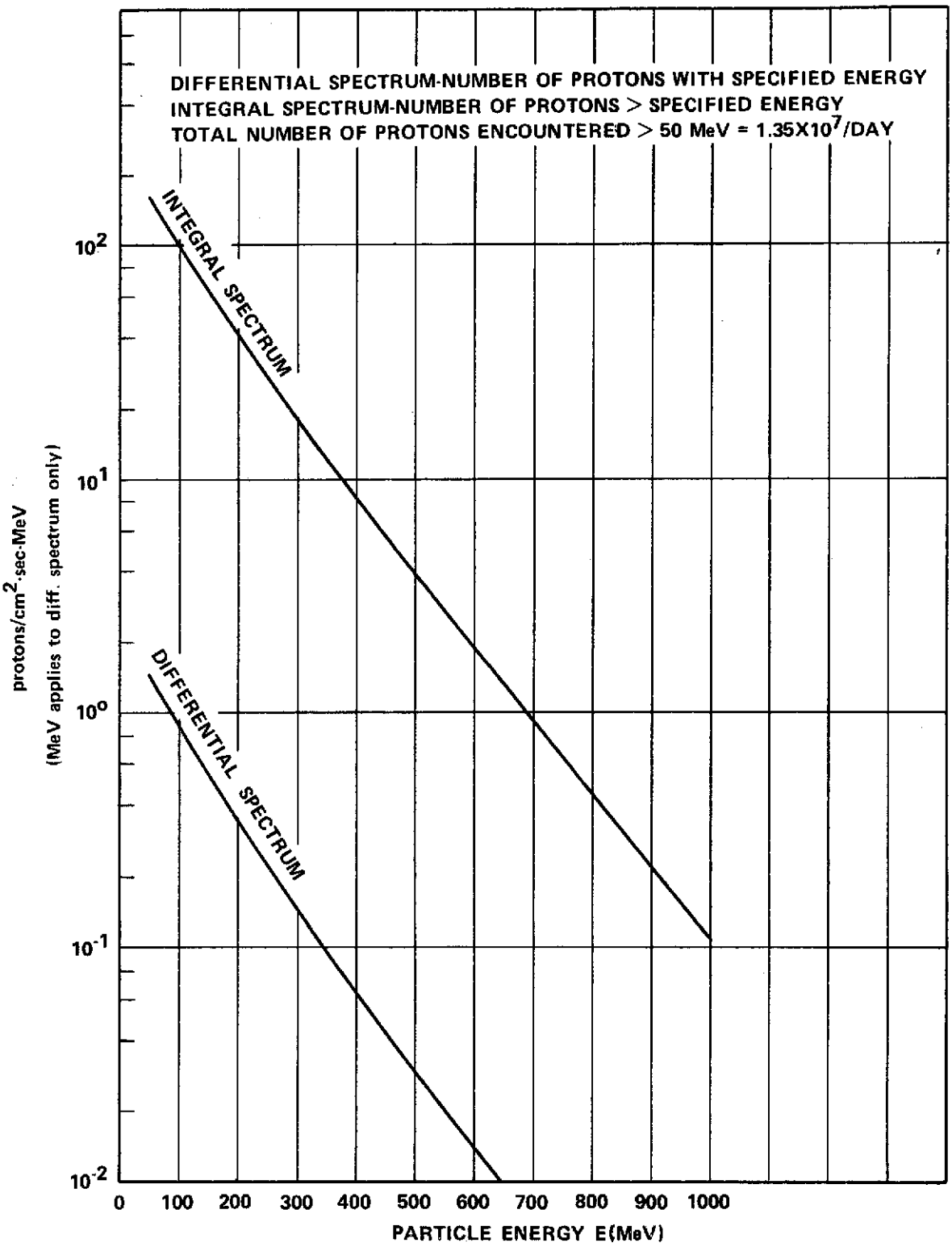

Figure 6. Time-averaged energy spectra for protons greater than 50 MeV at constant circular orbit altitude of 926 km (500 n.mi.) and 90-deg inclination.

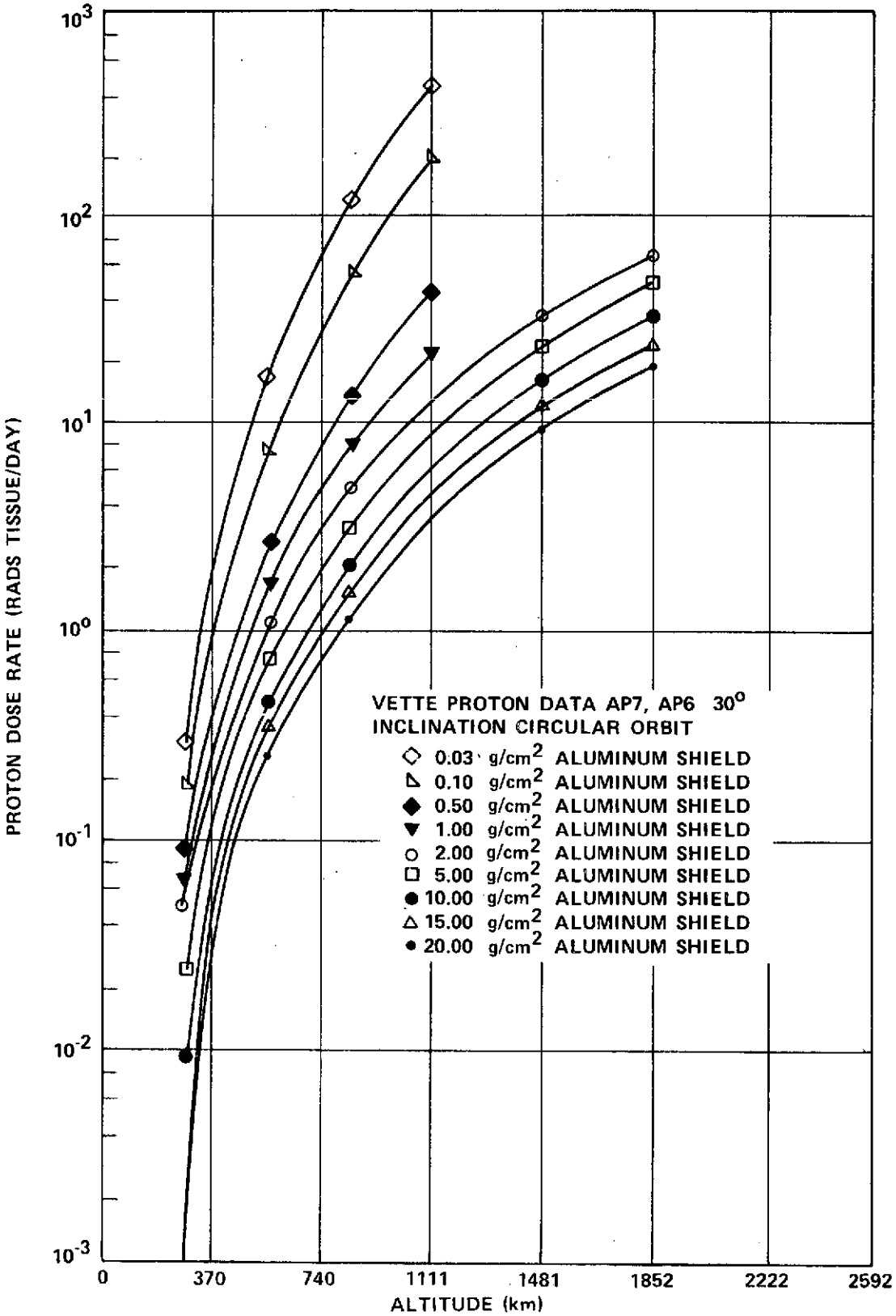

Figure 7. Proton dose rates vs shield thickness for 30-deg orbit inclination.

Some of the problems associated with assessing possible damage and degradation effects of space radiation to low-thrust orbiting spacecraft and components have been detailed earlier in this document. This section will discuss some of the solutions arrived at that provide preliminary spacecraft and mission design criteria for the SEP/AST development programs and other SEPS studies.

It should be kept in mind that the uncertainty factor, in the best available raw data from References 6 and 7, is from two to four. Therefore, all further techniques used to apply these data to a specific problem introduce other uncertainty factors, which means that the primary objective of any analysis using these data should be to minimize these uncertainty factors. When they are indeed minimized, they represent the state-of-the-art at the time and must be used until other methods represent a significant improvement.

Since the time-averaged calculations appear to be inadequate for low-thrust trajectory analyses, other techniques have been derived and used to aid in solving the problem. The techniques are explained in detail in Reference 5, the work referred to in footnote 4, and Appendix A.

Briefly, the methods used required the integration of two distinct analyses. The first method, shown in Appendix A, is a low-thrust trajectory analysis independent of a radiation environment, which used analytical approximations to optimum steering, including three-dimensional cases. The second analysis is the conversion of the Vette (GSFC/NASA) time-averaged differential energy spectra for protons and electrons into a 1-MeV electron equivalence environment, as explained in the work referenced in footnote 3.

The refined and updated space radiation modeling included the use of the latest available Van Allen radiation environments for protons and electrons from NASA/GSFC. For protons these data included AP7, AP6, and AP5 covering all energy ranges greater than 0.4 MeV. The electron data are AE4 and AE5 for all energy ranges greater than 0.5 MeV.

The outside isotropic differential energy spectra are transported through various shield or cover-plate thicknesses of fused silica, obtaining new normal incidence differential energy spectra at the active region of the solar cell. A differential damage factor is then applied to the internal differential spectra, arriving at a normal incident 1-MeV electron equivalence environment for both the proton and electron. These data are stored in the appropriate subroutines

of a computer program developed by the author (see footnote 4) as a function of three variables — shield thickness, altitude, and inclination — which cover the whole space of possible orbit parameters through geosynchronous altitudes. A 1-MeV equivalent electron damage factor rate is thus defined at each spatial point along the SEPS trajectory. The total accumulated particles are then summed at each step along the orbit and applied as a variable in a solar-cell power degradation function.

These methods represent a significant improvement over the use of time-averaged data while trying to assess the possible damaging effects of space radiation to spacecraft and components. They further allow the calculation of earth-orbital SEPS performance data considering the effects of possible power losses on trajectory-shaping analyses. The payoff for vehicle and mission designers is that preliminary mission-dependent environmental criteria may be economically generated for all possible earth orbital SEPS missions. Thus, a maximum allowable degradation factor may be assessed with respect to vehicle configuration and a defined mission set. Also, forbidden operating ranges for a SEPS become obvious from such an analysis.

Figures 8 through 11 show a composite proton and electron environment reduced to 1-MeV electron equivalent damage factors as a function of varying cover-slide (shield) thicknesses for all space through geosynchronous altitudes. Note that the highest degradation rates for a nominal 6-mil cover-slide thickness occur at approximately 5185 km (2800 n.mi.).

Figure 12 shows the results of various modelings for a solar-cell power degradation function based on a combination of laboratory test results and analytical procedures as referenced earlier. The cells considered are all silicon types and include data for the high-efficiency violet cell. The function is designed for use in a low-thrust trajectory program, which is documented in Reference 5 and the work referenced in footnote 4.

The total accumulated 1-MeV equivalent electrons may be referenced both to a laboratory 1-MeV electron fluence and a conversion of the natural space-radiation environment, encountered on a specific low-thrust SEPS trajectory, to an accumulated 1-MeV equivalent electron fluence as discussed earlier. The evaluation of SEPS power losses may then be computed at different points or orbit increments and applied as a trajectory-shaping effect for low-thrust spiraling orbits. Indeed, hazards abound for this kind of modeling and there are considerable disparities among opinions of the investigators working on

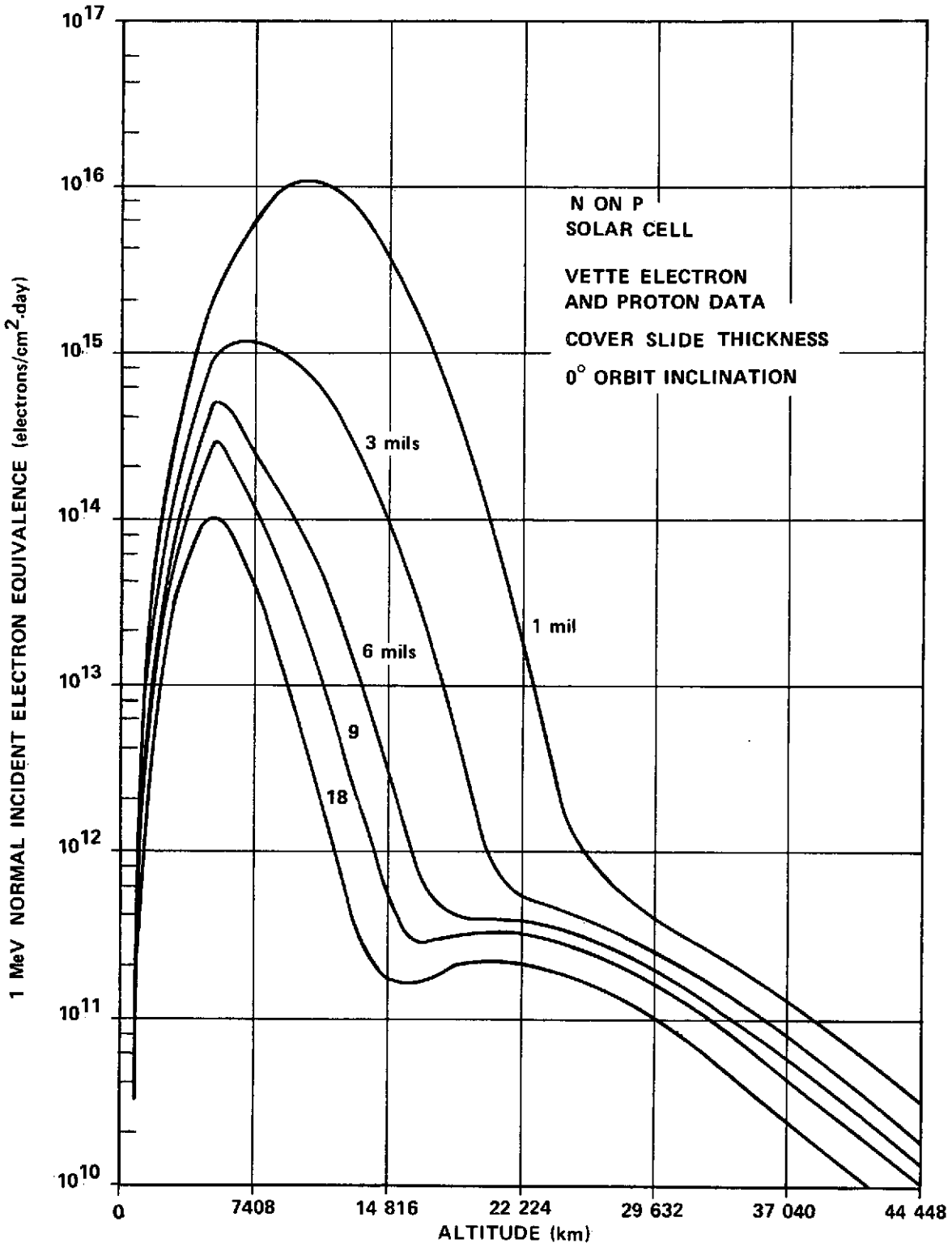

Figure 8. Composite proton and electron space radiation environments converted to 1-MeV electron equivalent fluence/day as a function of varying cover slide thickness for a 0-deg orbit inclination.

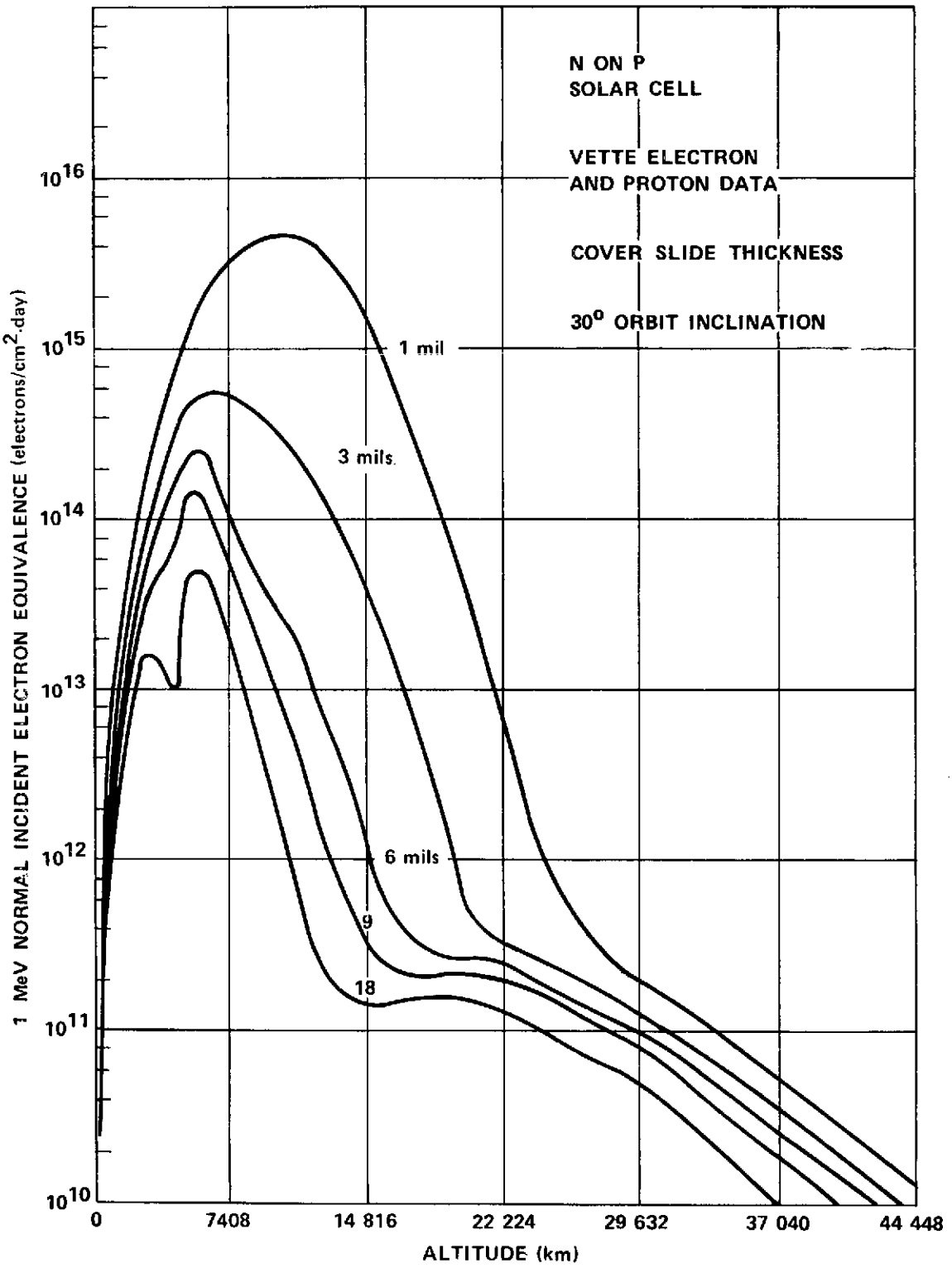

Figure 9. Composite proton and electron space radiation environments converted to 1-MeV electron equivalent fluence/day as a function of varying cover-slide thickness for a 30-deg orbit inclination.

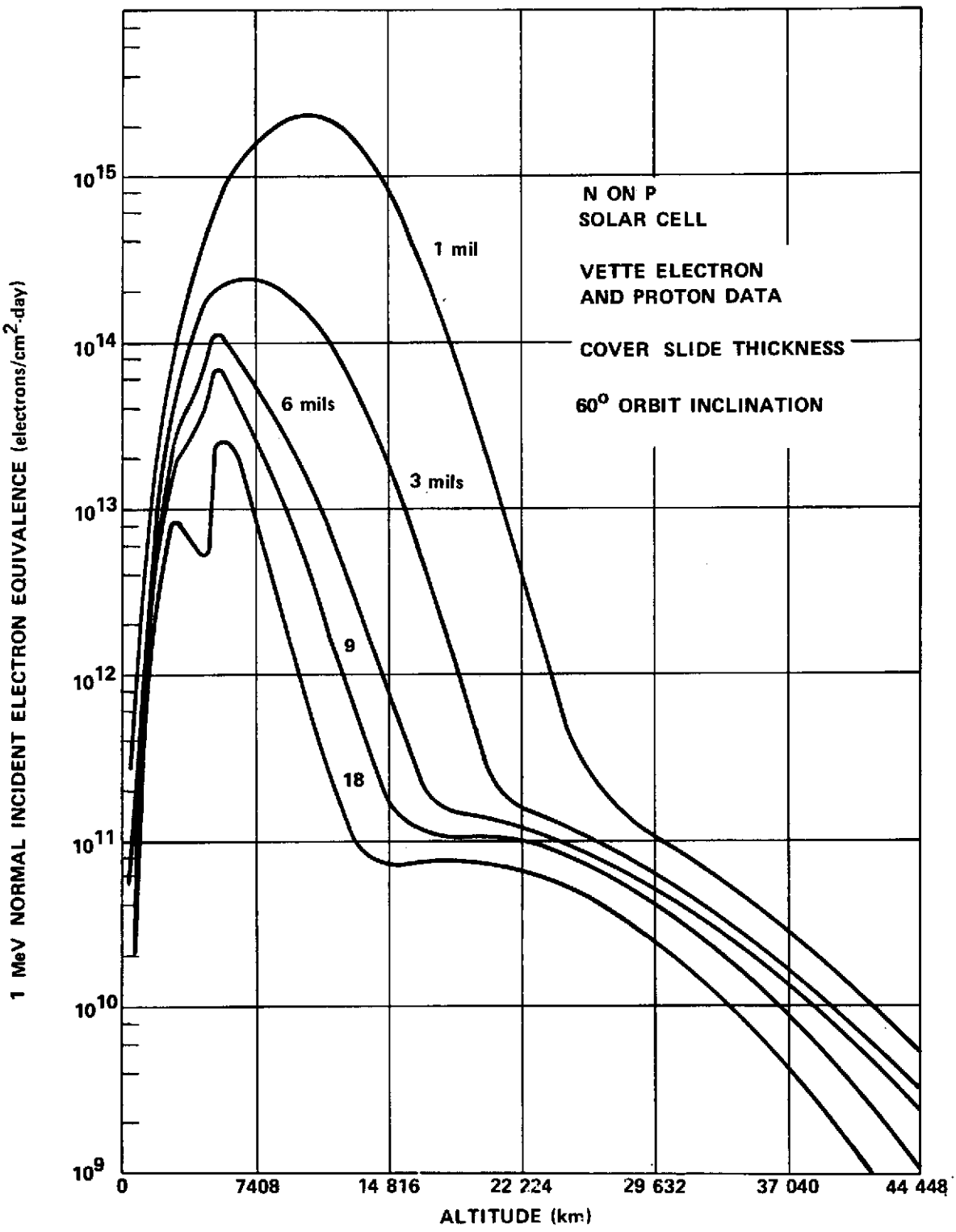

Figure 10. Composite proton and electron space radiation environments converted to 1-MeV electron equivalent fluence/day as a function of varying cover slide thickness for a 60-deg orbit inclination.

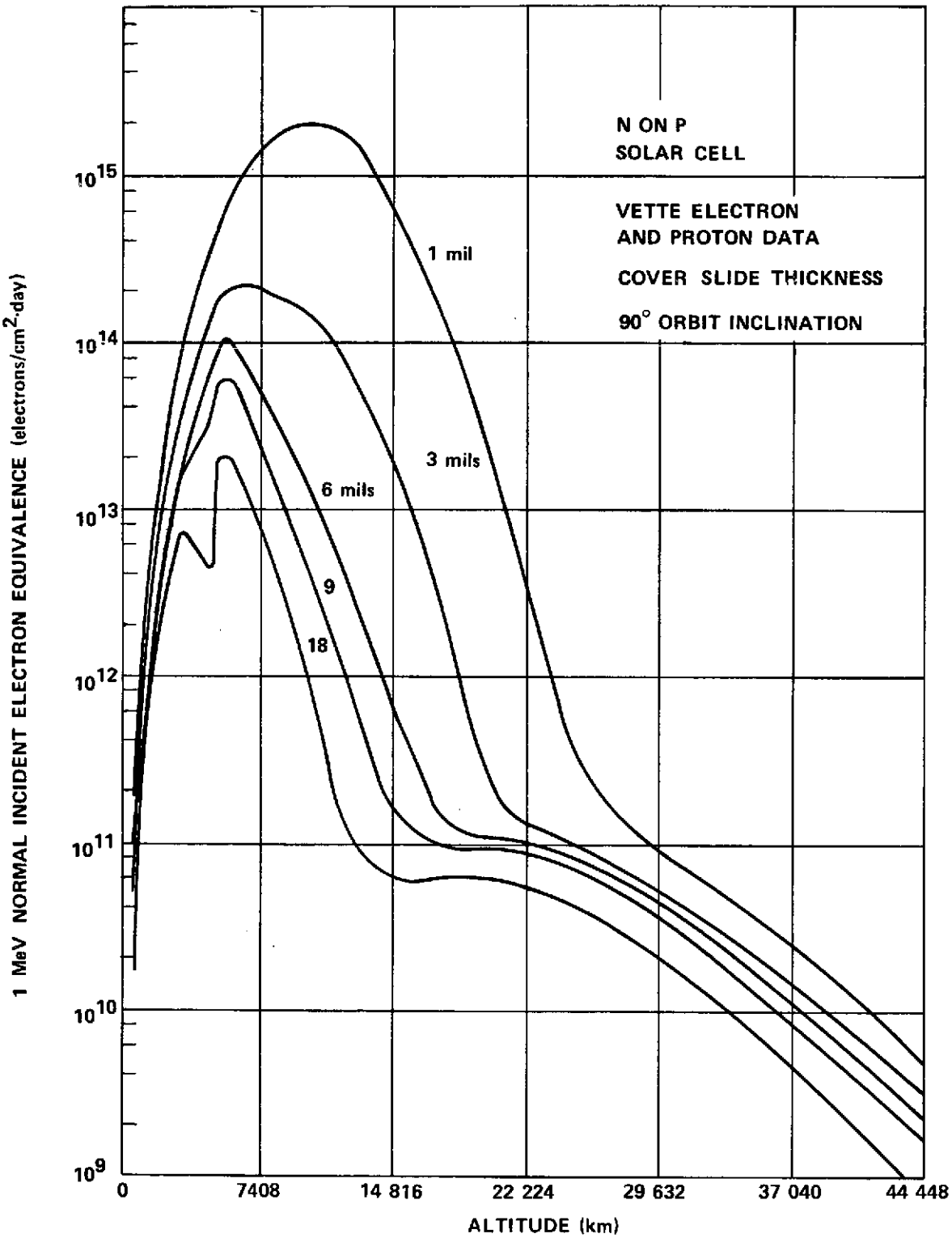

Figure 11. Composite proton and electron space radiation environments converted to 1-MeV electron equivalent fluence/day as a function of varying cover-slide thickness for a 90-deg orbit inclination.

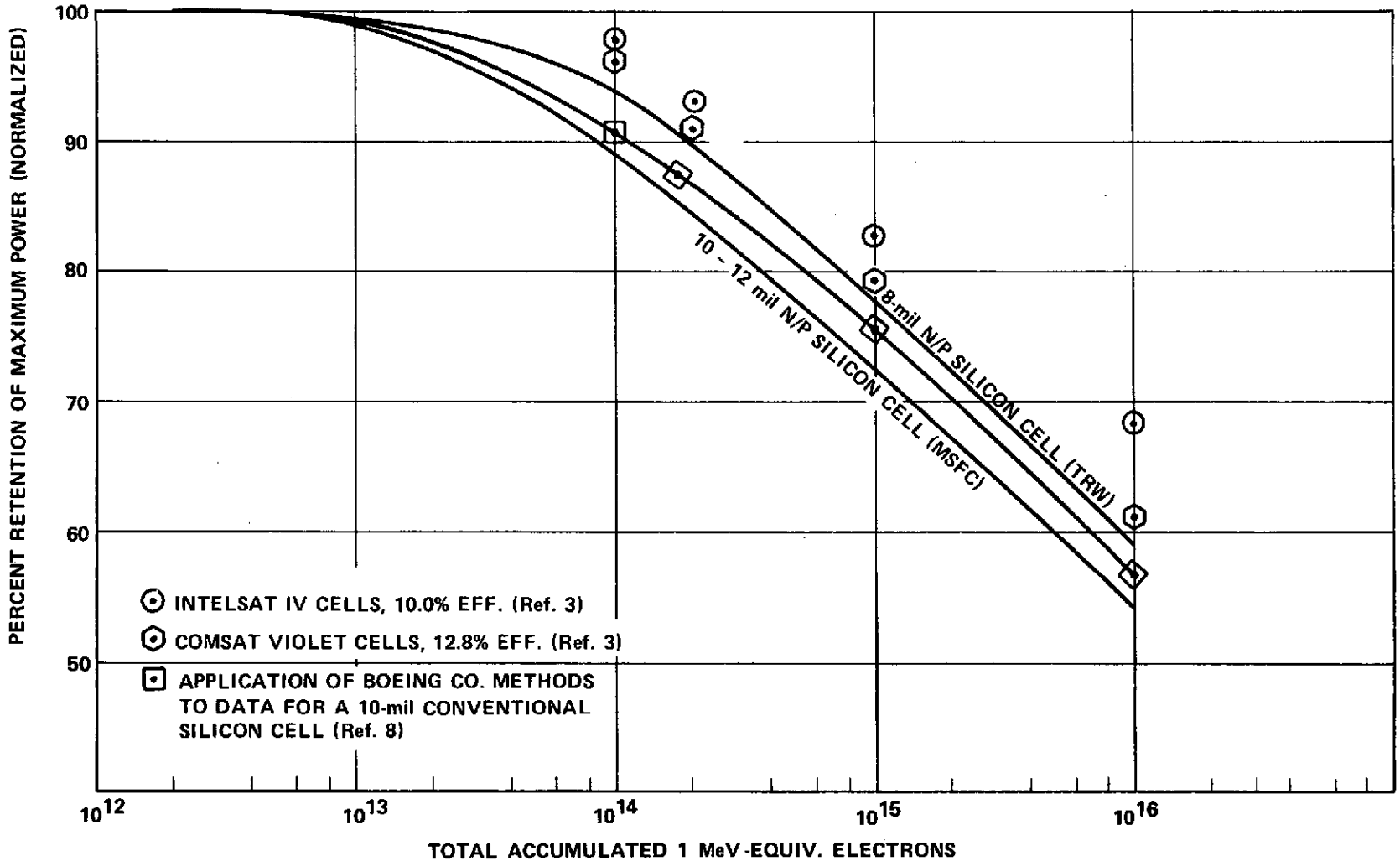

Figure 12. Silicon solar-cell power degradation functions vs accumulated 1-MeV electron equivalent fluence for 8-, 10-, and 12-mil-thick cells.

this problem. However, because of the nature of this mission analysis problem, an average curve of the modeling may be assumed without undue compromising of preliminary design studies for a solar electric propulsion vehicle.

Horne and Wilkinson of The Boeing Company [8] recently reported a comparative analysis of improved solar-cell performance predictions versus conventionally employed methods. They found that low-energy proton damage is underestimated at high fluences; general proton degradation is underestimated at high fluences because of the damage gradients, and electron degradation is overestimated by the simplified angular dependence treatment. As more accurate degradation modeling for solar cells becomes available, these models should be put into a data form that would render them directly applicable and usable in a low-thrust trajectory program. A recommendation is that the Horne and Wilkinson results be converted into such a format for solar cells of various types and thicknesses.

Figure 13 gives the computational results of the aforementioned analyses. Shown are the total accumulated 1-MeV equivalent electrons for near-optimum SEPS trajectory simulations for geosynchronous missions which start at indicated initial altitudes of 13 621, 11 121, 8621 and 3620 km (7335, 6005, 4655, and 1955 n.mi.) and inclinations of 0.0 deg. A constant thrust level equivalent to seven electric thrusters, each generating a constant propulsive force of 0.1334 N (0.03 lb), is assumed, along with a total propellant flow rate of 0.33 g/sec. Figure 14 illustrates the effects of varying the solar array cover-slide thicknesses on the retention of initial maximum power at the target altitude for potential SEPS geosynchronous missions as specified in Figure 13. Of particular significance here is the fact that a relatively thin shield of several mils will reduce these power losses drastically. This is because the most damaging low-energy protons are effectively removed from the cell environment.

Figure 15 gives insight as to how drastically the effects of the magnetically trapped space radiation may influence trip times for these same geosynchronous missions. The number of days in parentheses for each mission represents mission times required if no radiation degradation effects were considered. A tabular form of the data generated for these four geosynchronous missions is shown in Table 2, arbitrarily designated as missions 1 through 14.

Figures 16 and 17 show SEPS performance data generated for low earth orbit [up to 3704 km (2000 n.mi.)]. Observe that several mils of cover-slide thickness did not greatly influence the mission time for the delivery leg of a single sortie with an initial starting altitude of 555 km (300 n.mi.). This is partly because the high damage factor rates were not encountered until near the

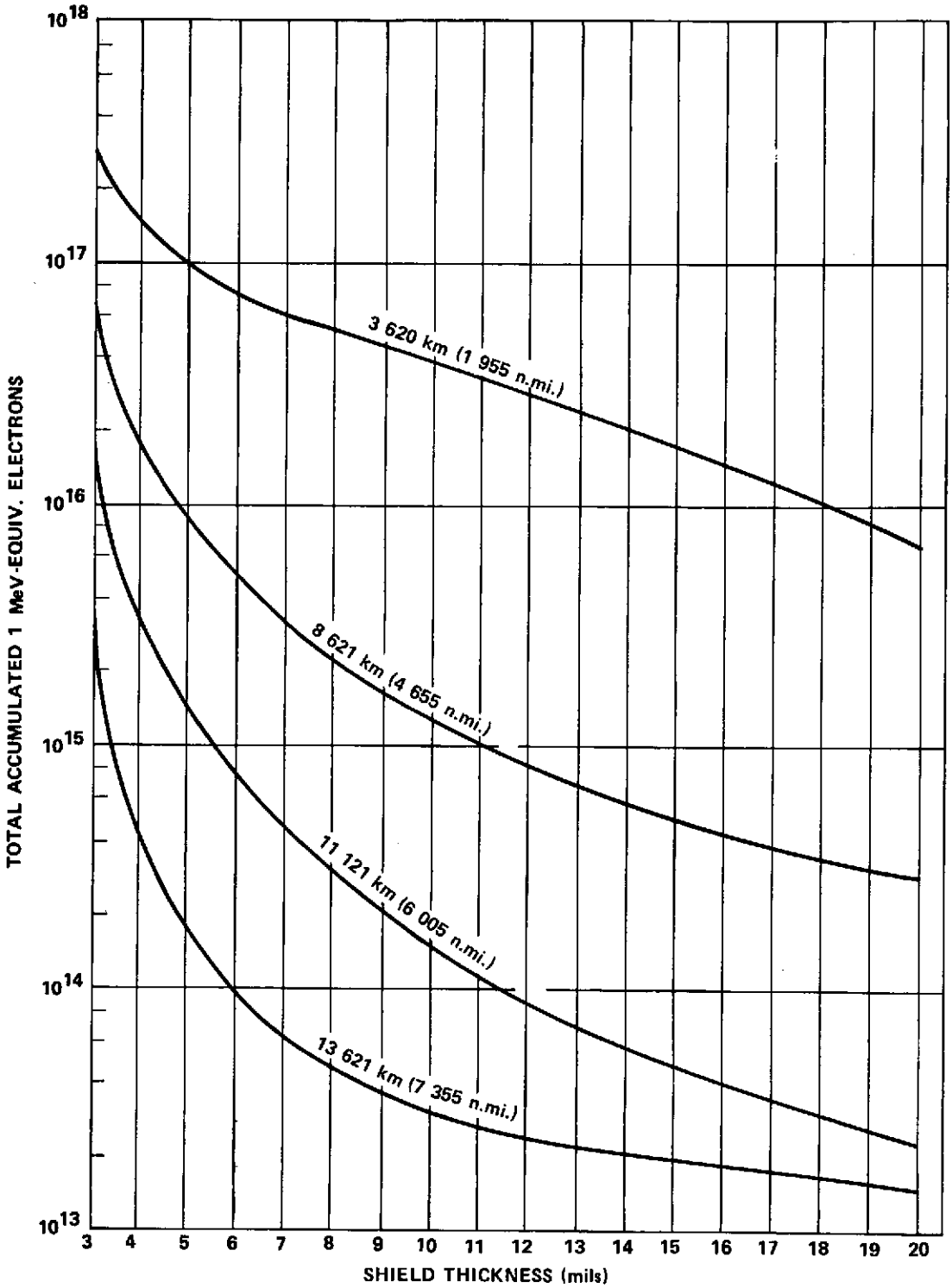

Figure 13. Total accumulated 1-MeV equivalent electrons vs cover-slide thickness for specific SEPS starting from initial changeover orbits of 13 621, 11 121, 8621, and 3620 km and 0-deg inclination.

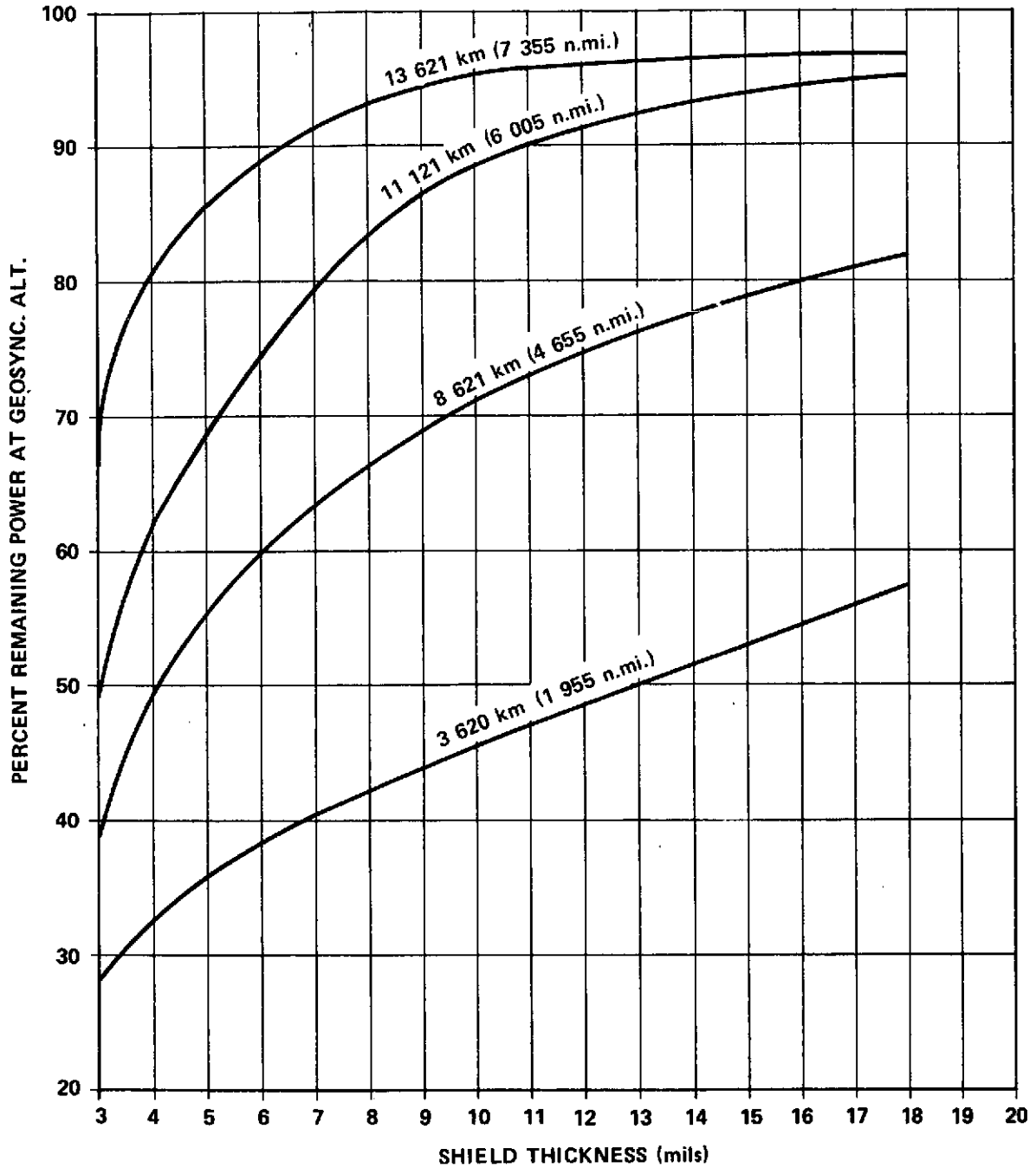

Figure 14. Percentage of initial power remaining at the target altitude for the specific SEPS geosynchronous missions indicated in Figure 13.

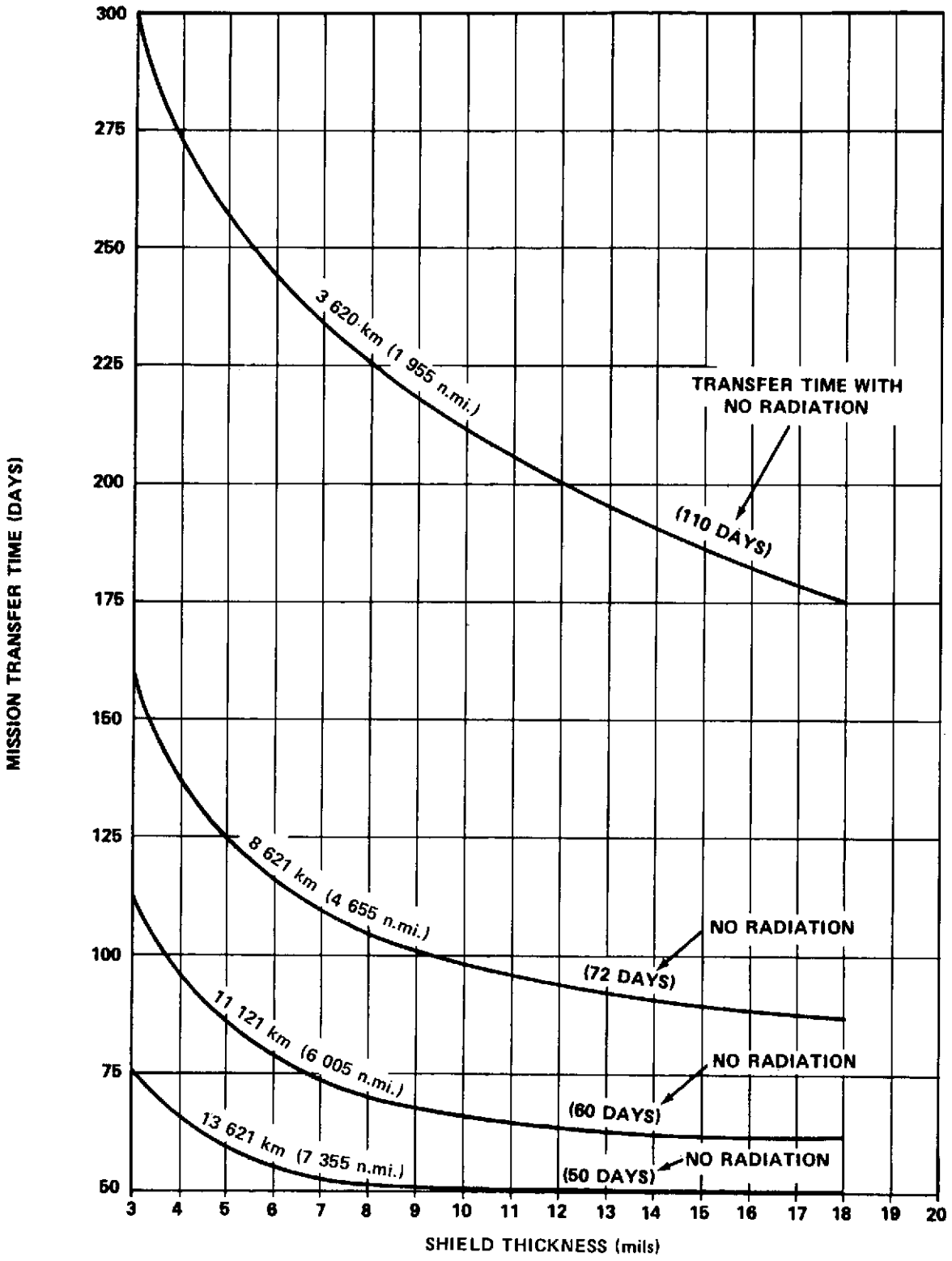

Figure 15. Relative spacecraft trip times as a function of varying array cover-slide thickness for SEPS geosynchronous missions as indicated.

TABLE 2. EARTH-ORBITAL SEPS PERFORMANCE DATA CONSIDERING TRAJECTORY INTERACTION WITH SOLAR-CELL DEGRADATION FROM VAN ALLEN RADIATION FOR SEPS GEOSYNCHRONOUS MISSIONS

	Mission 1					Mission 2					Mission 3					Mission 4				
Initial r_p/r_a (km)	20 000/20 000					17 500/17 500					15 000/15 000					10 000/10 000				
Initial Alt. (km)	13 621					11 121					8 621					3 620				
Initial Incl. (deg)	0.0 [No plane change (NPC)]					0.0 (NPC)					0.0 (NPC)					0.0 (NPC)				
Initial Mass (kg)	3 000					3 000					3 000					3 000				
	SEPS Performance with Radiation																			
Cover-Slide Thickness (mils)	No Rad*	3	6	9	18	No Rad*	3	6	9	18	No Rad*	3	6	9	18	No Rad*	3	6	9	18
Mission Time (days)	50.06	76	55.05	51.14	50.1	60.24	114.02	78.61	68.49	61.82	72.5	166.49	115.07	101.02	86.73	110.45	304.25	241.13	218.06	174.97
Number of Revs.	95	144	104	97	95	131	247	170	148	134	186	420	293	257	221	445	1 142	928	840	680
Final Alt. (km)	35 784	35 784	35 784	35 784	35 784	35 784	35 784	35 784	35 784	35 784	35 784	35 784	35 784	35 784	35 784	35 784	35 784	35 784	35 784	35 784
Final Mass (kg)	2 858	2 783	2 844	2 855	2 857	2 829	2 674	2 776	2 805	2 824	2 793	2 523	2 671	2 711	2 753	2 684	2 126	2 308	2 374	2 498
Final Power (% of initial)	100	63.09	89.06	94.87	97.61	100	48.85	74.13	86.34	95.33	100	38.9	59.67	69.04	81.98	100	27.92	38.74	43.73	57.13

* SEPS performance without power degradation due to radiation.

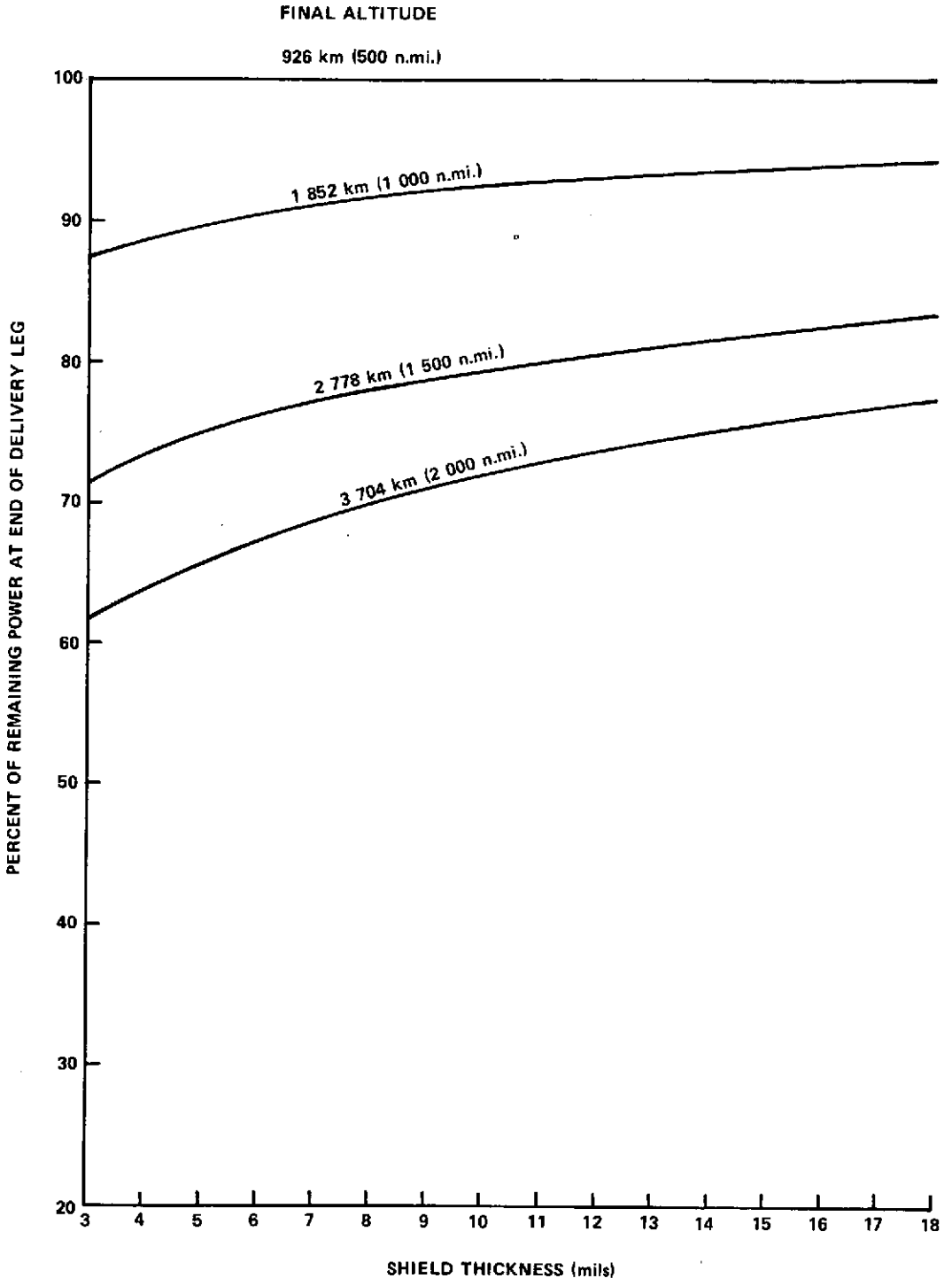

Figure 16. Percentage of initial power remaining at the target altitude for SEPS low earth-orbital missions from an initial 555 km circular orbit to final altitudes of 926, 1852, 2778 and 3704 km — 28.5-deg inclination.

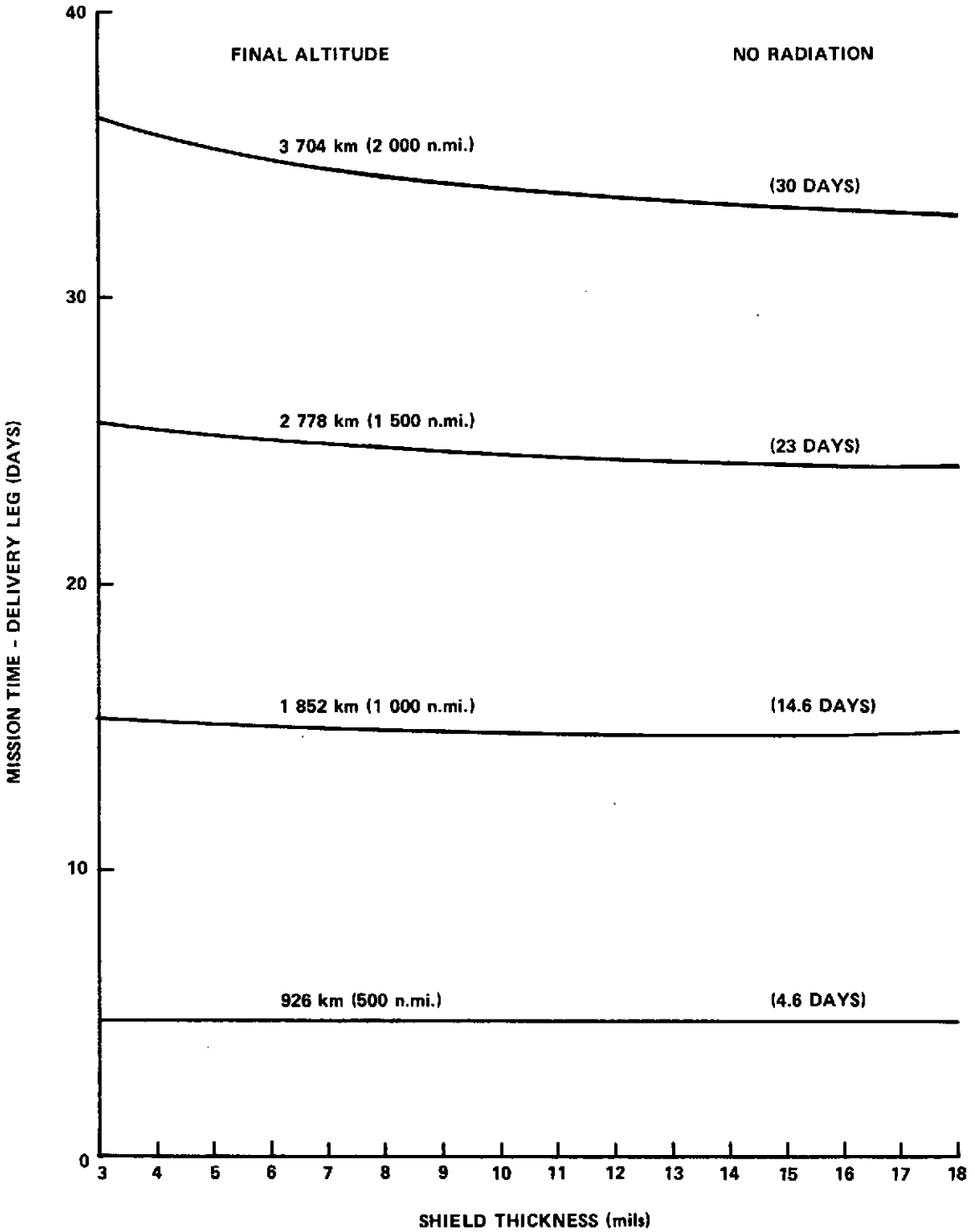

Figure 17. Relative spacecraft trip times as a function of varying array cover-slide thickness for SEPS low earth-orbital missions shown in Figure 16.

end of the delivery leg. However, SEPS operations for projected 5-year lifetimes may result in power losses of more than 50 percent, depending on the altitudes at which most of the spacecraft's idle time is spent. Returning to lower altitudes for waiting purposes requires using extra propellant and reduces thruster lifetime allocations needed for actual payload delivery and retrieval. These missions are summarized in Table 3.

Another factor that was evident from the performance data generated was that whereas the most damaging low-energy protons (0.4 to 4 MeV) at higher altitudes were effectively removed by relatively thin shielding, the proton population at the lower altitudes had higher initial energies (a harder spectra) and can penetrate the range of shield thicknesses considered in these analyses. A nominal 6-mil cover slide is generally baselined for a SEPS solar array at present. However, from the data presented in Figures 13, 14, and 15, an optimum cover-slide thickness may be arrived at considering mission parameter trade studies with regard to the additional weight penalties of increased thicknesses. If a comparison is made between the effects of 6-mil-thick and 12-mil-thick cover slides for the 11 121-km (6005-n.mi.) initial altitude case, the following relative parameters are noted: (1) an increase by an order of magnitude in the number of 1-MeV equivalent electrons accumulated for the 6-mil thickness as compared to the 12-mil thickness, (2) an increase in mission transfer time of 20 days for the 6-mil case as compared to an increase of only 2 days for the 12-mil case, and (3) an increase in the beginning of life power degradation from 8 percent for the 12-mil-thick cover slide to 26 percent for the 6-mil-thick cover slide. The actual weight differences of the 6-mil-thick and 12-mil-thick cover slides were not factored into these analyses but could possibly become a factor to be considered for some missions with regard to the amount of payload weight at the target altitude. Based on a present baseline SEPS solar array configuration with a total surface area of 250 m^2, these shield weights would be approximately 4.98 kg (11 lb) per mil (fused silica) of thickness. This means a weight difference of about 29.9 kg (66 lb) for a 6-mil-thick and a 12-mil-thick cover slide. The effects of this weight difference will be investigated in subsequent studies.

Table 4 summarizes the performance data generated for four other possible SEPS missions which include simultaneously changing the plane of the orbit while the orbital altitude is being raised.

(2) Solar-Flare Proton Events.

(a) SEPS geosynchronous missions considerations. When SEPS geosynchronous operations and missions in a space-based mode are being considered, possible hazards to successful missions caused by the cyclic and

TABLE 3. EARTH-ORBITAL SEPS PERFORMANCE DATA CONSIDERING TRAJECTORY INTERACTION WITH SOLAR-CELL DEGRADATION FROM VAN ALLEN RADIATION FOR LOW EARTH-ORBITAL MISSIONS

	Mission 5					Mission 6					Mission 7					Mission 8				
Initial r_p/r_a (km)	6933/6933					6933/6933					6933/6933					6933/6933				
Initial Alt. (km)	555					555					555					555				
Initial Incl. (deg)	28.5 [no plane change (NPC)]					28.5 (NPC)					28.5 (NPC)					28.5 (NPC)				
Initial Mass (kg)	2000					2000					2000					2000				
	SEPS Performance with Radiation																			
Cover-Slide Thickness (mils)	No Rad.[a]	3	6	9	18	No Rad.[a]	3	6	9	18	No Rad.[a]	3	6	9	18	No Rad.[a]	3	6	9	18
Mission Time (days)	4.69	4.69	4.69	4.69	4.69	14.66	15.15	14.99	14.91	14.74	23.04	25.69	24.97	24.70	24.24	30.09	36.33	34.84	34.15	33.03
Number of Revs.	68	68	68	68	68	195	201	199	198	197	285	314	306	303	298	350	412	397	390	379
Final Alt. (km)	926	926	926	926	926	1852	1852	1852	1852	1852	2778	2778	2778	2778	2778	3704	3704	3704	3704	3704
Final Mass (kg)	1986	1988	1986	1986	1986	1957	1956	1957	1957	1957	1933	1926	1928	1929	1930	1913	1895	1899	1901	1905
Final Power (% of initial)	100 100[b]	100 99[b]	100 100[b]	100 100[b]	100 100[b]	100 100[b]	87.32 82.60[b]	90.34 86.25[b]	92 89[b]	94.17 90.7[b]	100 100[b]	71.30 64.75[b]	76.11 70.06[b]	78.63 73.0[b]	83.43 78.26[b]	100 100[b]	61.93 56.50[b]	66.70 62.15[b]	71.09 64.5[b]	77.74 71.83[b]

a. SEPS performance without power degradation due to radiation.
b. Percentage of initial power remaining for round-trip mission.

TABLE 4. EARTH-ORBITAL SEPS PERFORMANCE DATA CONSIDERING TRAJECTORY INTERACTION WITH SOLAR-CELL DEGRADATION FROM VAN ALLEN RADIATION FOR SEPS MISSIONS WHICH INCLUDE A SIMULTANEOUS PLANE CHANGE ALONG WITH ORBIT RAISING

	Mission 9					Mission 10					Mission 11					Mission 12				
Initial r_p/r_a (km)	6 933/6 933					17 500/17 500					15 000/30 000					10 000/2 000				
Initial Alt. (km)	555					11 121					8 621/23 620					3 620/13 621				
Initial Incl. (deg)	28.5 (NPC)					10 deg Plane Change (10 deg – 0 deg)					10 deg Plane Change (10 deg – 0 deg)					15 deg Plane Change (0 deg – 15 deg)				
Initial Mass (kg)	2 000					3 000					3 000					5 000				
	SEPS Performance with Radiation																			
Cover-Slide Thickness (mils)	No Rad*	3	6	9	18	No Rad*	3	6	9	18	No Rad*	3	6	9	18	No Rad*	3	6	9	18
Mission Time (days)	100.6		164.28	153.11	135.27	69.83			78.02		66.84		80.63	73.56	68.90	166.25		After 14.94		
Number of Revs.	629		901	855	780	150			167		100		120	110	103	385		After 68		
Final Alt. (km)	35 784		35 784	35 784	35 784	35 784			35 784		35 784		35 784	35 784	35 784	35 784		2402/ 7881		
Final Mass (kg)	1 713		1 529	1 561	1 613	2 801			2 778		2 810		2 769	2 789	2 802	4 523		4 957		
Final Power (% of initial)	100		48.63	53.54	63.78	100			87.33		100		81.11	89.16	95.64	100		60		

* SEPS performance without power degradation due to radiation.

sporadic solar-flare activity become a factor in spacecraft design and operations. For high-changeover Tug/SEPS orbits above 12 964 km (7000 n.mi.), the damaging effects of the magnetically trapped charged particles are reduced to a level equal to that of very low earth-orbital missions. This means that for 5-year operational SEPS lifetimes, total degradation of the system's beginning-of-life (BOL) power may be easily held to less than 10 percent with a nominal coverslide thickness of about 6 mils when considering this environment alone. Unfortunately, at geosynchronous altitudes, the magnetic field protection from solar-flare proton activity breaks down during magnetic storms which accompany solar flares and significant numbers of damaging lower-energy protons are able to reach the spacecraft and its components. Consequently, the effects of just one large solar flare may produce the equivalent damage caused by the steady-state charged-particle environment over a 5-year SEPS life span, considering no array retraction capability.

A detailed explanation and modeling of this cyclic solar-flare activity may be found in Reference 9, along with dose rates behind certain material thicknesses for tabulated solar-flare data from the 19th cycle (1954-1964). This section will emphasize statistical modeling and 1-MeV electron equivalent damage and will explore ways to possibly minimize the degradation effects of solar-flare protons. The need for statistical modeling of such phenomena is evident if an acceptable risk probability is to be arrived at for certain proposed SEPS missions.

The magnetically trapped charged-particle environment is more or less steady state while the solar-flare activity is cyclic and sporadic. It is not a simple task to adequately model this activity, nor is it easy to decide upon the degree of accuracy of such modeling. Many solar prediction models are available, with a wide disparity in comparative results. The Poisson distribution probability model used in Reference 9 and modified in the work referenced in footnote 3, seems to be a more practical approach to the problem of determining the long-term performance variations of a SEPS operating in a solar proton environment. Solar-flare protons present more hazards to SEPS geosynchronous and interplanetary missions than those associated with performing these missions with conventional spacecraft. As discussed in earlier sections, low-energy protons are quite damaging to solar cells and lower-energy proton flares (< 10 MeV) occur more often than higher-energy ones. Consequently, most solar-flare activity will cause some degradation of the SEPS initial power levels, depending on the size and energy spectra of the flares and the relative position of the vehicle. It is probably worth mentioning that the period of time projected for possible SEPS missions, 1980 to 1990, happens to include the most severe years in the 11-year solar activity cycle.

(b) Characteristics and frequency of solar-flare proton events. The radiation intensity from solar-flare activity follows an approximate 11-year cycle with enormous flux variations ranging from about 10^5 protons/cm^2 at solar minimum to approximately 10^9 protons/cm^2 per flare at solar maximums for protons with energy above 30 MeV. The solar-radiation intensity also varies with distance from the sun. Because lower-energy protons are more damaging to solar cells than high-energy ones, any statistical modeling for the SEPS application should include the full spectrum of protons that might reach the spacecraft. It appears that this should include consideration of all particles greater than 3 MeV for the SEPS geosynchronous operations. It is significant to note that during intense solar magnetic storms, solar protons in the electron-volt range have been detected at geosynchronous altitudes.

The basic objective of the modeling in this report is not to predict when a solar flare is most likely to occur, as in the case for statistical studies of sunspots and recorded flare data, although these kinds of analyses, depending on their relative accuracy, may be extremely useful for SEPS operations in knowing when to consider retracting solar arrays for additional protection. Rather, the objective is to provide a long-term (up to 5 years) prediction, using a representative solar cycle, of possible damage and degradation to spacecraft functions for various operating modes during which time the probability is quite large (> 50 percent) that an integral number of flares will occur.

Although the modeling here is concerned with expected solar-proton activity at 1 AU, relative flux intensities vary with heliocentric distance and position. This means that specific interplanetary trajectories and mission duration times may also be a significant factor in assessing probable encountered flux and subsequent damage to spacecraft functions. These problems are discussed to an extent in Reference 10; however, a considerable reduction of the presented data is necessary to put the data in a form that is most applicable to a mission-dependent radiation damage effects analysis. Using the data as presented, one may arrive at a crude approximation of 1-MeV electron equivalent conversions and dose rates expected on specific interplanetary missions.

(c) SEPS solar-array baseline functional requirements for 1-AU operations. A baseline functional requirement for the MSFC Solar Array Technology development is that the power degradation due to all causes must be no more than 16 percent, i.e., from 25 kW BOL to no more than 21 kW end of life (EOL) after 5 years of operation in free space at 1 AU. A further requirement is that no more than 10 percent of this degradation be directly attributable to the charged-particle environment at this distance. It was stated earlier that the

magnetically trapped charged-particle environment could possibly cause this kind of degradation, regardless of the solar-flare proton activity. Thus, if such a requirement is to be met, trade studies involving array design, expected missions, and operational procedures must be carried out to arrive at an acceptable risk probability that the mission will be successful.

According to an interpretation of the JPL modeling of the probable solar-proton environment for the SEPS Encke flyby mission[5] which covers a time period of 1080 days, there is at least a 50-percent chance of incurring a power loss of no more than 5 percent, i.e., retaining a relative power (P/P_0) of 95 percent. Furthermore, there is a 16-percent probability that power losses may go as high as 15 percent and a 3-percent chance that these power losses due to solar-flare protons may go higher than 20 percent. Two obvious questions are apparent from such an analysis: (1) what is an acceptable level of degradation for the mission? and (2) what is an acceptable risk factor that this requirement be met? The environmental modeling covered only 700 days and some linear-type extrapolation was necessary in this crude attempt to extend the presented data to a radiation damage effects analysis.

(d) Solar-flare proton events model and data presentation. The Poisson distribution probability model for solar-flare proton activity at 1 AU, as discussed in detail in Reference 9, has been selected as the representative model for this document. The probability of N large events occurring during a time of t weeks of exposure is given by the Poisson distribution:

$$P(N,t) = \frac{e^{-\lambda t}(\lambda t)^N}{N!} \quad , \quad N = 0, 1, 2, \ldots .$$

The events considered for solar-cell degradation analysis are given by the spectrum,

$$J(>P) = N_0 \, e^{-p/p_0}$$

5. Thrust Subsystem Integration Technology Development Program Control Document; Section 6, Environmental Design Requirements, Jet Propulsion Laboratory, CIT, Pasadena, Calif., Feb. 21, 1974.

where p is in units of million volts and

$$\lambda = 0.02,\ N_0 = 1 \times 10^{11},\ p_0 = 91\ \text{MV},\ E > 3\ \text{MeV} \quad .$$

The differential spectrum in million electron volts units for the preceding integral spectrum is

$$J(E) = \frac{N_0}{p_0} \quad \frac{E + 938}{\sqrt{E^2 + 1876\ E}} \quad \exp \frac{\left(-\sqrt{E^2 + 1876\ E}\right)}{p_0}$$

where J(E) is in units of particles/cm^2·MeV·event.

Table 5 shows the total 1 MeV electron equivalence (e/cm^2·flare) assuming an initial half-space isotropic proton environment behind fused silica cover slides of various thicknesses for the solar flare spectrum described above and the corresponding event rate λ. Table 6 gives the probability of solar-flare events based on the Poisson formula. Shown is the probability of having exactly N events (P) and also the probability of having more than N events. These data are for the event rate (λ) of 0.02 events/week for 260 weeks or a 5-year SEPS lifetime operation. Figure 18 shows the 1-MeV electron equivalence conversion for one flare behind various thicknesses of fused silica cover slides.

Now such data may be applied to the expected solar array and other spacecraft component performances while operating in such an environment. The probability of having a certain number of flares over a 5-year period may be obtained from Table 6. The million electron volts electron-equivalent damage rate per flare behind various shield thicknesses is obtained from Table 5. If for thin solar cells (8 mils) it is assumed that nearly as much contribution comes from the back side as from the front, the equivalence fluence per flare may be doubled.

The possible effects on solar-array power degradation for various array configurations using an event rate of $\lambda = 0.02$ events/week for 260 weeks are shown in Table 7. However, we observe from Table 6 that the probability of 10 flares occurring using this model is only 2.19 percent. Notwithstanding,

TABLE 5. SOLAR-FLARE SPECTRA CONVERSION TO 1-MeV ELECTRON EQUIVALENT FLUENCE (e/cm^2-flare) AS A FUNCTION OF COVER SLIDE THICKNESS

Fused Silica Cover-Slide Thickness (mils)	Total Equivalence[a] (1 flare)
3	1.59×10^{14}[b]
6	1.10×10^{14}
8	9.60×10^{13}
12	7.70×10^{13}
18	6.00×10^{13}
25	4.90×10^{13}
35	4.00×10^{13}

a. Half-space isotropic.

b. $\lambda = 0.02$ events/week, $\phi\ (> p) = 1 \times 10^{11}\ e^{-p/91}$ $(E > 3$ MeV).

TABLE 6. POISSON PROBABILITY MODEL OF OCCURRENCE OF SOLAR-FLARE EVENTS

Number of Events, N	Probability of Exactly N Events, P ($\lambda = 0.02$)	Probability of More Than N Events ($\lambda = 0.02$)
0	0.0055	0.9945
1	0.0287	0.9658
2	0.0746	0.8912
3	0.1293	0.7619
4	0.1681	0.5938
5	0.1748	0.4190
6	0.1515	0.2675
7	0.1125	0.1550
8	0.0731	0.0819
9	0.0423	0.0397
10	0.02196	0.0177
11	0.0104	0.0073

Note: $P = \dfrac{e^{-\lambda t}\ (\lambda t)^N}{N!}$;

$\lambda = 0.02$ (events/week), and

$t = 5$ years $= 260$ weeks.

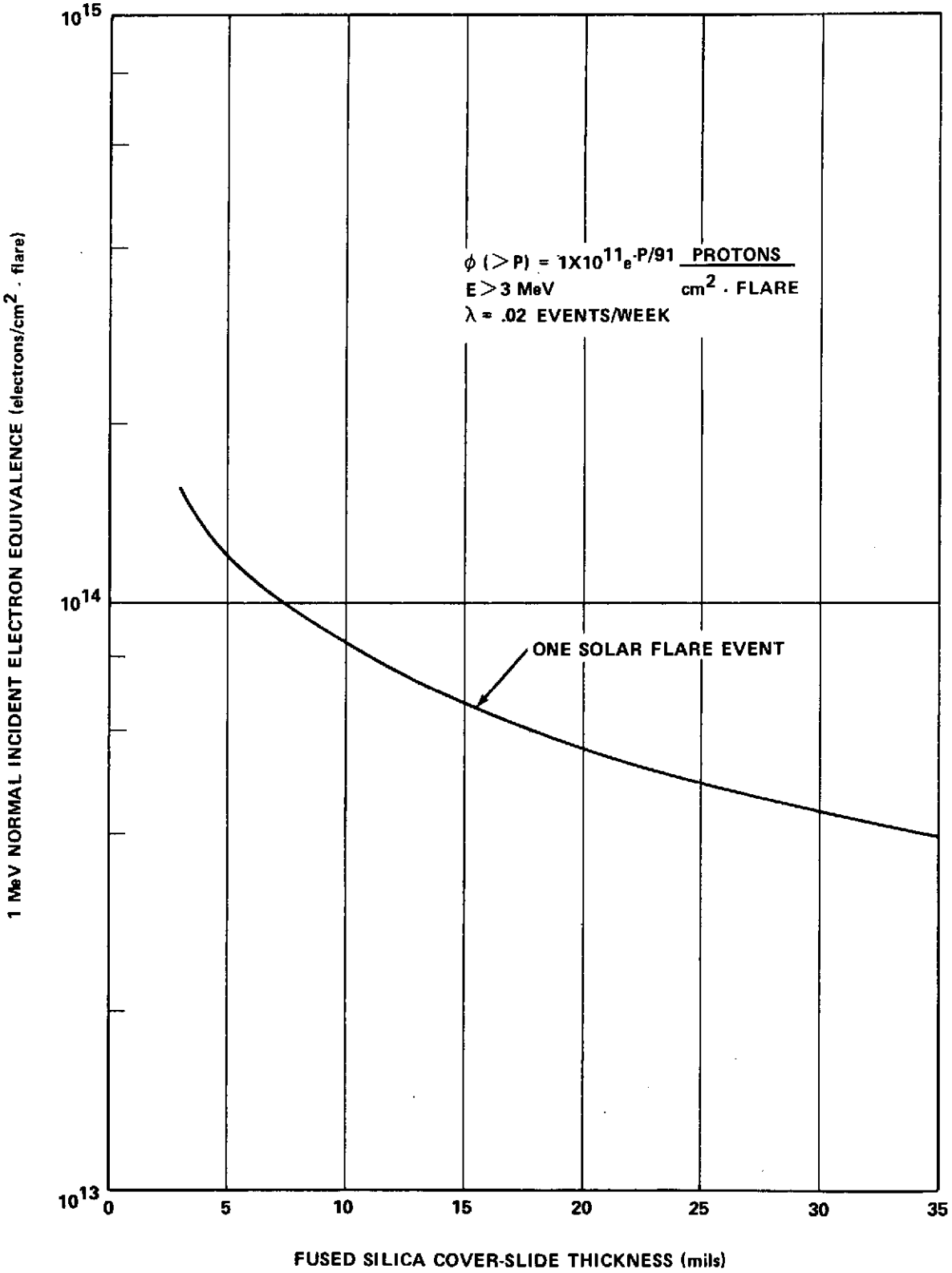

Figure 18. 1-MeV electron equivalence/flare conversion as a function of varying shield thicknesses.

TABLE 7. DEGRADATION EFFECTS OF VARIOUS SILICON SOLAR-CELL CONFIGURATIONS INCLUDING SEPS BASELINE AS A FUNCTION OF THE OCCURRENCE OF AN INTEGRAL NUMBER OF SOLAR FLARES

Fused Silica Cover-Slide Thickness (mils)	Cell Thickness (mils)	Total[a] 1-MeV Equiv. Electron (1 flare)	P/P_0[b] 10-Ω-cm Base Res. (%)	Total[a] 1-MeV Equiv. Electron (5 flares)	P/P_0[b] 10-Ω-cm Base Res. (%)	Total[a] 1-MeV Equiv. Electron (10 flares)	P/P_0[b] 10-Ω-cm Base Res. (%)
3	8 10-12	1.59×10^{14}	91.5 87.0	7.95×10^{14}	79.6 74.5	1.59×10^{15}	74.0 69.0
6		1.10×10^{14}	93.5 88.3	5.50×10^{14}	82.2 77.0	1.10×10^{15}	77.0 72.0
8		9.60×10^{13}	94.0 89.0	4.80×10^{14}	83.1 78.0	9.60×10^{14}	78.0 72.9
12		7.70×10^{13}	95.0 90.6	3.85×10^{14}	85.0 79.5	7.70×10^{14}	79.8 74.8
18		6.00×10^{13}	96.0 92.0	3.00×10^{14}	87.0 81.5	6.00×10^{14}	81.6 76.6
25		4.90×10^{13}	96.6 93.0	2.45×10^{14}	88.2 83.0	4.90×10^{14}	83.0 77.8
35		4.00×10^{13}	97.0 94.0	2.00×10^{14}	89.7 84.2	4.00×10^{14}	84.8 79.5

a. Half-space isotropic.

b. Normalized power retention P/P_0.

the probability of exactly five flares occurring is 17.48 percent and the probability of more than five flares is a relatively high 41.9 percent. Subsequent power losses if assessed from Figure 12 for the occurrence of five flares are on the order of 12 to 22 percent for SEPS baseline array candidates over a 5-year period if no retraction capability is considered. It is probable that a significant retraction capability for the solar arrays may serve to reduce power losses to acceptable levels. Trade studies considering such things as weight and performance penalties for various configurations of retractable cells are necessary to aid configuration and mission design concepts. Also, solar-flare detection analyses, if reasonably accurate, may provide early warning of impending solar activity, thus aiding the retraction operations.

The use of improved solar cells with initial high efficiencies and slower degradation rates in a charged-particle environment should improve the reliability and performance of a SEPS in meeting all specific mission objectives. Significant annealing or recovering from initial power losses has been evident even in lower-efficiency conventional silicon cells. These are some of the factors that should be considered in the long-term assessment of space-radiation hazards to a SEPS.

(3) Solar Wind. For a SEPS operating at maximum geosynchronous altitudes, the earth's magnetosphere affords protection from the low-energy solar-wind charged particles except during periods of magnetic storms associated with solar-flare activity. Even when these magnetic storms occur and the earth's magnetic rigidity cutoff is low enough to allow these particles to reach the spacecraft, the composition of the solar cosmic rays is such that the flux intensities of the higher-energy protons, as discussed earlier, will tend to dominate these short-term damage effects on the spacecraft and its components.

In the case of interplanetary missions for the stage, where prolonged exposure to solar-wind charged particles occurs, significant degradation in the power output of solar cells has been observed. The solar wind consists of approximately equal numbers of kilo-electron-volt protons and electron-volt electrons along with a few heavier ions. These particles are continuously emitted from the sun and at 1 AU the velocity at quiet sun is 300 km/sec, and the effective temperature has been observed to vary from 1 to 3×10^5 K. Since charged particles with these energy ranges are effectively stopped by less than 1-mil thickness of most materials, damage to the power output of solar cells is caused by pitting, darkening, or otherwise affecting the surface coating of transparent surfaces. This reduces the overall power output of solar cells and the efficiency of the cells. Thermal properties of surfaces may also be altered

by the darkening of white paint or other surface coatings. Fused silica cover slides have been found to provide significant improvement over other materials in maintaining its transparent properties. There are also some electrical interferences caused by the ever-present solar wind, which becomes more acute near the sun. Additional effort and data are needed in this area to fully appreciate and assess with greater accuracy the detrimental effects to be expected when the SEPS is operating in this environment. Further details on the solar-wind environment may be found in References 10 and 11.

(4) Galactic Cosmic Radiation. Galactic cosmic rays are a highly penetrating radiation originating beyond the solar system. They possess energies greater than 1 BeV and are capable of extraordinary interactions with matter in the upper atmosphere and in spacecraft materials, creating significant primary collision and secondary processes. Galactic particles consist of a low flux ($\sim$ 4 particles/cm^2.sec) of very high-energy protons (> 100 MeV), alpha particles, million-electron-volt electrons, and heavier nuclei isotropically present in space.

Galactic-particle collisions with matter produce many kinds of secondary radiation, including protons, neutrons, mesons, electrons, photons and other unidentified particles. The extremely high energy of these particles makes shielding impractical if not impossible, but fortunately their low population density renders them less a problem to projected missions involving the SEPS than the previously mentioned forms of charged-particle radiation.

Galactic cosmic-ray impact may cause some concern for prolonged manned spaceflights and can lead to interference and failure in some sensitive electronic components and subsystems. They also may cause spurious signals in solid-state detectors and affect photographic film and other emulsions. In short, galactic particles represent an uncontrollable space radiation environment that we can do very little about except be aware of its presence as a function of various mission parameters. Further details are found in References 10 and 11.

b. Electromagnetic Radiation and Thermal Control.

(1) Status of SEP/AST Thermal Modeling and Assumed Requirements for Component Testing of the Stage. The extensive treatment of the possible charged-particle radiation impact on the design and mission planning for a SEPS in the earlier section titled Charged Particles has probably made it appear that this represents the most serious challenge to SEPS missions. However, the problem

of electromagnetic radiation effects and temperature control analyses for the SEP/AST development programs and other SEPS preliminary design activities is probably the most pressing at this date. This is perhaps true because the analyses that have been performed were not in support of a defined and expressly agreed-upon baseline vehicle configuration and mission set. For example, the JPL studies referenced in footnote 5 were singly oriented to the Encke mission using an integrated spacecraft and science package configuration. Other studies are currently considering a 25-kW full-capability SEPS with as many as seven thrusters operating simultaneously. Thus, it is obvious that meaningful and supportive thermal analyses must be preceeded by agreed-upon mission-dependent performance expectations for the SEP stage. The available data covering this area at the moment are fragmented and support a wide variety of conclusions. For example, the minimum expected temperatures range from -30° C (-22° F) to -196° C (-320° F) and maximum temperatures from 100° C (212° F) to 159° C (315° F) for specific spacecraft components.

The MSFC Solar Array Technology development, the LeRC thruster and power processor development, and the JPL Advanced Systems Technology programs are currently coordinating and sharing pertinent component thermal analysis data; the objective is to arrive at adequate tesing facilities and procedures in addition to accurate computer software thermal modeling for the total spacecraft system and mission.

A defined mission set emerges as the most significant driver for complete thermal analyses for the SEPS. The expected thermal environment at low earth orbit [555 to 1852 km (300 to 1000 n.mi.)] is significantly different from the thermal environment for SEPS geosynchronous applications. For interplanetary missions there is also a strong dependence on minimum astronomical-unit distance for inbound missions and maximum astronomical-unit distance for outbound missions in the determination of a "worst-case" thermal environment for spacecraft and component design purposes.

Solar array structures, fabrication materials, adhesives, and surface coatings, as well as engineering output parameters such as current, voltage, and power, have a strong performance dependence on extreme variations in temperature. Thruster restarts and power processor performance from mission-dependent cold-soak temperatures (shadowing) are factors for mission design and analyses considerations. Changes in the maximum available power and consequent changes in thrust levels are experienced as the total solar flux is reduced for outbound missions.

The sun's electromagnetic radiation is an indispensable part of a solar electric propulsion system since it is the primary source of power; however, the effective utilization of this unique space transportation capability requires demanding vehicle and component design ingenuity for efficient and economical exploitation of such a system.

(2) Sources and Characteristics of Electromagnetic Radiation. The main sources of electromagnetic radiation in the solar system are the sun, the planets, and the stars. These speed-of-light protons may be divided into three major wavelength regions: X-rays ($\lesssim 0.1\ \mu m$); optical (0.1 to 10 μm), which may further be subdivided into ultraviolet (0.1 to 0.4 μm); visible (0.4 to 0.75 μm), and infrared (0.75 to 10 μm) wavelength regions. If we integrate over the major portion of the optical differential spectrum for the sun at 1 AU, i.e., over the range from 0.2 to 5 μm, we arrive at an effective solar density constant of 135.30 mW/cm^2 with a $1/R^2$ intensity variation.

Planetary albedo is defined as the ratio amount of electromagnetic radiation reflected by a body to the amount falling upon it. This albedo factor varies with planetary, atmospheric, surface, and seasonal properties and is a maximum of 0.30 of the solar constant for the earth. The albedo for the planet Mercury may be as high as 0.70. In addition to the albedo, the earth constantly emits longer-wave or infrared radiation amounting to approximately 23.7 mW/cm^2 for altitudes up to 3704 km (2000 n.mi.) with the greatest intensity at a wavelength of about 10 μm. This value falls off with altitude and at a geosynchronous altitude of 35 784 km (19 323 n.mi.) the intensity is effectively about 1.0 mW/cm^2. Thus, low earth orbital SEPS missions will have to contend with a total of about 200 mW/cm^2 of total energy flux. This will probably create significant vehicle and component design problems to minimize extreme temperature variations. For some components of the vehicle, this level of energy flux will impose the most severe maximum thermal requirement of the mission set with the possible exception of closer than 0.5-AU missions.

(3) Laboratory Testing of Silicon Solar Cells to Determine Response and Relative Efficiencies Under Various Thermal Conditions. Silicon solar-cell response is generally limited to the wavelength regions between 0.3 and 1.2 μm, for which the integrated differential spectrum results in an effective solar-power density of 104.4 mW/cm^2. As stated earlier, violet cells respond to shorter wavelengths in the ultraviolet range and require a cover sheet that permits a cut-on of approximately 0.35 μm instead of the usual 0.41 μm cut-on for conventional silicon cells. A 6-mil-thick ceria-doped microsheet is being tested with the violet cell with good results. Fused silica cover sheets are generally used with conventional cells.

Permitting the ultraviolet range of light into the cells also causes some concern as to ultraviolet degradation of some adhesive coatings. It is reported in Reference 2 that the total degradation of the cells' output parameters under a 4-sun ultraviolet irradiation for 5000 hours was only 2.6 percent. Therefore, it is expected that most mission-dependent ultraviolet degradation for a SEPS solar array will be relatively small when compared with the degradation concerns of hard charged-particle space radiation. A spacecraft operating power on the order of 25 kW requires a dual-winged configuration vehicle with a solar-panel area of approximately 100 to 120 m^2 (1100 to 1300 sq ft) per wing, depending on the relative efficiency of baseline cells. A significant point here is that a 1-percent increase in solar-cell efficiency results in an 8-percent reduction in the required array size necessary to produce 25 kW of power. With this sort of vehicle configuration and the total electromagnetic spectra as defined, one can begin to appreciate inherent thermal design problems. Specific thermal analysis and testing of the solar array, specific thruster configuration, and various sizes of power processors will have to be performed with the goal in mind of arriving at a total thermal model for the SEPS.

Laboratory testing of solar cells has employed a xenon arc lamp with appropriate filters which provide a close match to the solar spectrum. The response of the solar cells is a strong function of temperature and they must be in thermal equilibrium during measurements. The commonly used solar-cell output parameters of short-circuit current, open-circuit voltage, and maximum power vary linearly with temperature in the range of -50° C (-58° F) to 100° C (212° F). Consequently, the mission-dependent thermal properties of the SEPS become an important factor for performance and mission analyses. Studies have also shown that 1-MeV electron irradiation damage is independent of temperatures between -80° C (-112° F) and 130° C (266° F).

(4) Fundamental Thermal Approximations. Some representative mission-dependent vehicle component temperatures may be estimated by using the basic radiation-equilibrium skin temperature concept. This is the temperature that a thin skin or insulated surface would reach when either the aerodynamic heating or the relative normal incident energy flux applied to the skin surface is just balanced by the radiative heat transfer from the surface. This effect is approximately by the formula

$$\dot{q} = \sigma \epsilon T^4$$

where σ is the Stefan-Boltzmann constant and has a value of 5.66×10^{-8} W/m^2·K^4 (1.71×10^{-9} Btu/ft^2·hr·°R^4) and ϵ is the emissivity, having a value of 1.0 for a black body. Now, using an absorptivity/emissivity ratio of 0.95 and 0.38 for the front and back sides of the solar array, respectively, a close approximation to a relative solar-array temperature curve generated by Lockheed Aircraft Corp., California, (under NASA Contract NAS8-30315) may be obtained. Thus, considering the vehicle's distance from the sun, its proximity to a radiating planet, possible shadowing periods and absorptivity/emissivity properties of the components, preliminary estimates of the temperature variations may be computed as a function of the specific SEPS mission.

The definition of mission-dependent electromagnetic radiation, along with basic computational assumptions, provide methods for arriving at preliminary estimates of temperature variations in the components of the SEPS. In addition to the aforementioned need of stage design, these temperature data are helpful in assessing the performance capabilities and mission design and analyses for the SEPS. These preliminary thermal approximations cannot replace thorough and detailed thermal analyses and testing. However, it is hoped that these mission-dependent temperature estimates will establish some representative bounds of expected temperature variations for a defined mission set which will provide preliminary thermal requirements for on-going SEP/AST development program activities and other solar electric propulsion studies. Complete thermal testing and analyses are continuing at LeRC for the thrusters and power processors, at MSFC for the solar arrays and power processors, and at JPL in support of the Advanced Systems Technology programs.

(5) Thermal Data Presentation. For low earth-orbital missions [up to 1852 km (1000 n.mi.)], maximum solar-array temperatures should be on the order of 60°C with a minimum of -101°C for earth occultation or shadowing. For other components of the stage that generate heat, low earth and other planetary orbit missions impose severe heat-rejection design problems because of albedo and infrared radiation contributions to the thermal environment. For example, a baseline power processor for the SEPS which is being developed at LeRC may have serious difficulty staying within maximum component temperature constraints while operating during low earth-orbital missions.[6] Also, a

6. Some of the results of a power processor thermal analysis titled Earth Orbital Thermal Effects on Solar Electric Propulsion Stage (SEPS) Power Processor, MSFC technical letter EP01, by A. A. McCool and J. D. Moss, July 31, 1974, are shown later in Figure 27.

Mercury orbiter mission could produce solar-array temperatures in excess of 260°C considering a normal incident photon bombardment plus Mercury's high albedo factor. Tilt control for the solar arrays is being examined as a technique to control array temperature for missions that go closer to the sun than 0.6 AU. It is expected that this technique will limit maximum array temperatures to about 160°C. Problems and conditions associated with maximum array tilting will need to be examined also.

Minimum solar-array temperatures for general interplanetary travel do not seem to be a problem for distance as far away as 6 AU since they will be about -150°C. However, for geosynchronous eclipse conditions, array temperatures may plummet at the rate of -50°C/min to a low of about -196°C (Fig. 17). For spiral SEPS trajectories from an initial changeover orbit of 14 000 km (7559 n.mi.), 100 such occultations may occur, creating array temperature variations from 60°C to -185°C. Thermal shock cycles tests in the range of -130°C to 95°C for the COMSAT violet showed little degradation in the electrical properties of the cells although a significant number of 0.05-mm-thick silver interconnects failed. This kind of temperature causes possible thruster restart concerns, creating the need for heater elements for some components of the thruster subsystem. However, it is not practical to provide heaters for the large exposed solar arrays. Slow restarts can severely impact mission transfer times, especially in the cases of some low earth-orbital missions in which up to 15 restarts a day may be required. Thruster startup delays of from 15 to 18 min may increase thruster-off time because of shadowing on an average of 30 percent to 45 percent. Hence, conditions which are as close as possible to instantaneous startup are desirable. Methods used to compute the amount of time that an earth-orbital SEPS will spend in the earth's shadow per revolution as a function of specific orbital parameters are shown in Appendix B.

Figure 19 shows preliminary estimates of SEPS solar-array flexible substrate temperatures as a function of astronomical-unit distance from the sun as generated by Lockheed Aircraft Corp. From 0.6 AU and closer, temperature control is maintained by tilting the arrays to produce a constant solar-energy flux and thus constant temperatures. Many factors must be examined to determine whether this method is actually feasible. For instance, small errors in pointing accuracy of the arrays may produce excessively high temperatures and the application of thermocouples may aid in the alleviation of this problem. Extreme array tilt angles may affect other exposed surfaces. Vehicle control problems may arise and fabrication materials of the arrays may be degraded by unconstrained array tilting. Note also the extremely low expected geosynchronous eclipse array temperature on Figure 19.

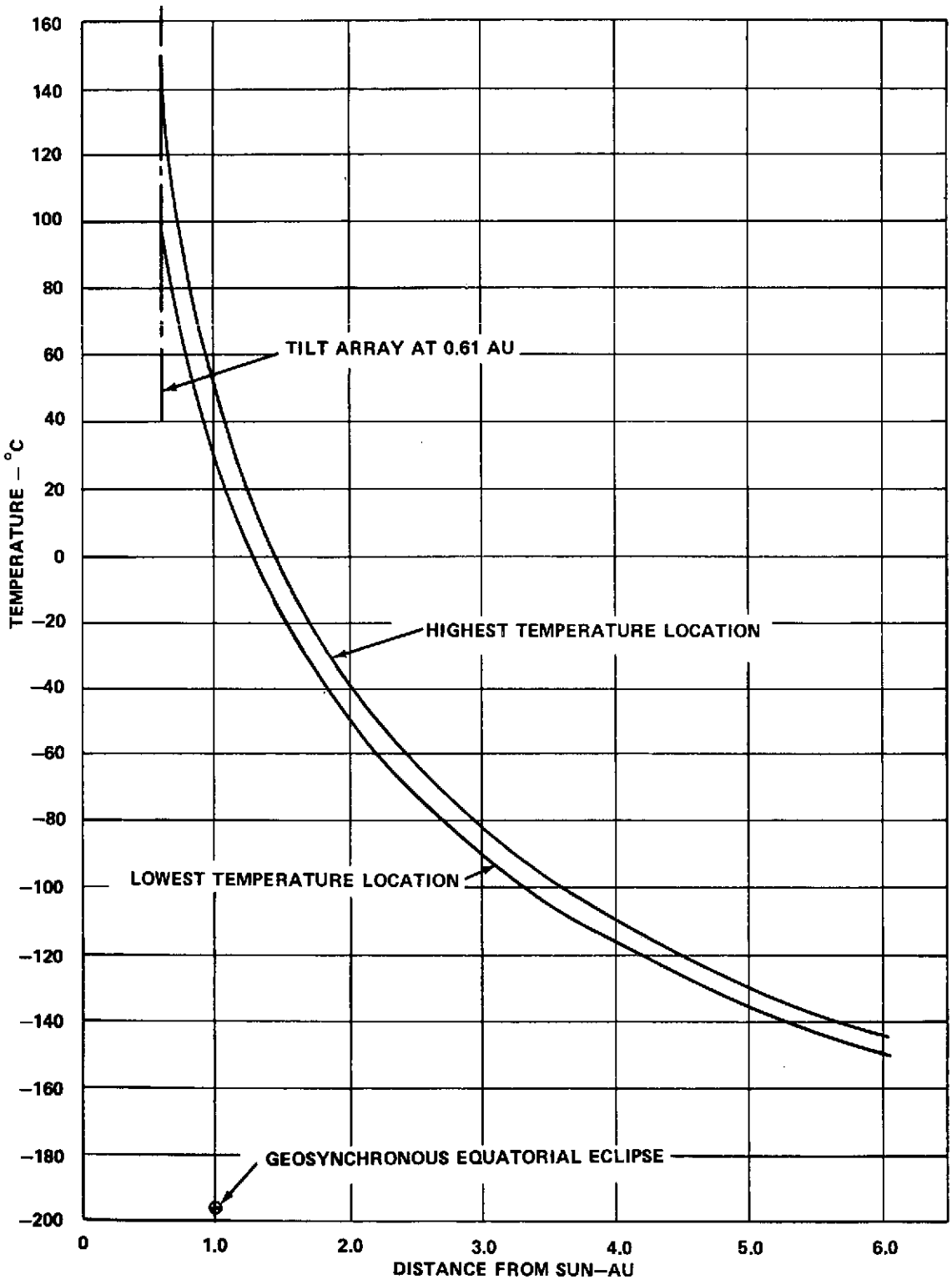

Figure 19. Preliminary estimates of the SEPS solar-array flexible substrate temperatures as a function of astronomical-unit distance from the sun.

Figure 20 shows a solar-array substrate temperature versus time profile for a SEPS comet Encke flyby mission.[7] Solar-array tilting techniques will be used to keep maximum temperatures for closest solar approach below 160° C (320° F). Figure 21 gives a solar-array substrate temperature versus time profile for a SEPS Mercury Orbiter. The line of constant temperature indicates array tilting. No consideration was given here to the high-albedo encounter environment or other planetary radiation. A planetary mission similar to the SEPS Mercury Orbiter mission should provide a worst-case maximum thermal environment. Figure 22 shows an array temperature versus time profile for an outbound SEPS Jupiter Flyby mission.

Figure 23 shows a preliminary power processor temperature variation as a function of astronomical-unit distance for a specific power processor (PP) surface area size and two solar-array distance configurations generated by North American Rockwell under NASA Contract NAS8-27360. Again, array tilting at a close solar distance will probably influence these temperatures. Figure 24 gives a power processor temperature versus time profile for the Mercury Orbiter missions for the power processor sizes and array configuration mentioned in Figure 23.

Figure 25 shows the dramatic falloff of solar array temperatures as a result of shadowing conditions for a 500-km (270-n.mi.) orbit and other parameters as shown. Notice also the rapid rise to normal operating temperatures within a few minutes after exiting the shadow. Specific temperatures at different points along the orbit are also a function of the orientation of the arrays. Figure 26 shows these eclipse conditions for a geosynchronous equatorial orbit which results in even lower temperatures for the solar array because the constantly emitted earth infrared radiation is essentially negligible at this altitude.

Figure 27 shows a worst-case parameterization of radiator surface temperatures (see footnote 6) for a 1.0-m^2 surface area baseline power processor operating at low earth-orbital altitudes through geosynchronous altitudes of approximately 35 784 km (19 322 n.mi.). All basic assumptions for the data presented in Figure 27 are detailed in the work referenced in footnote 6. The assumptions include (1) no direct solar radiation on the radiator, (2) a constant

7. Trajectories for the planetary and interplanetary missions were obtained from the Systems Analysis and Integration Laboratory (EL23) at MSFC.

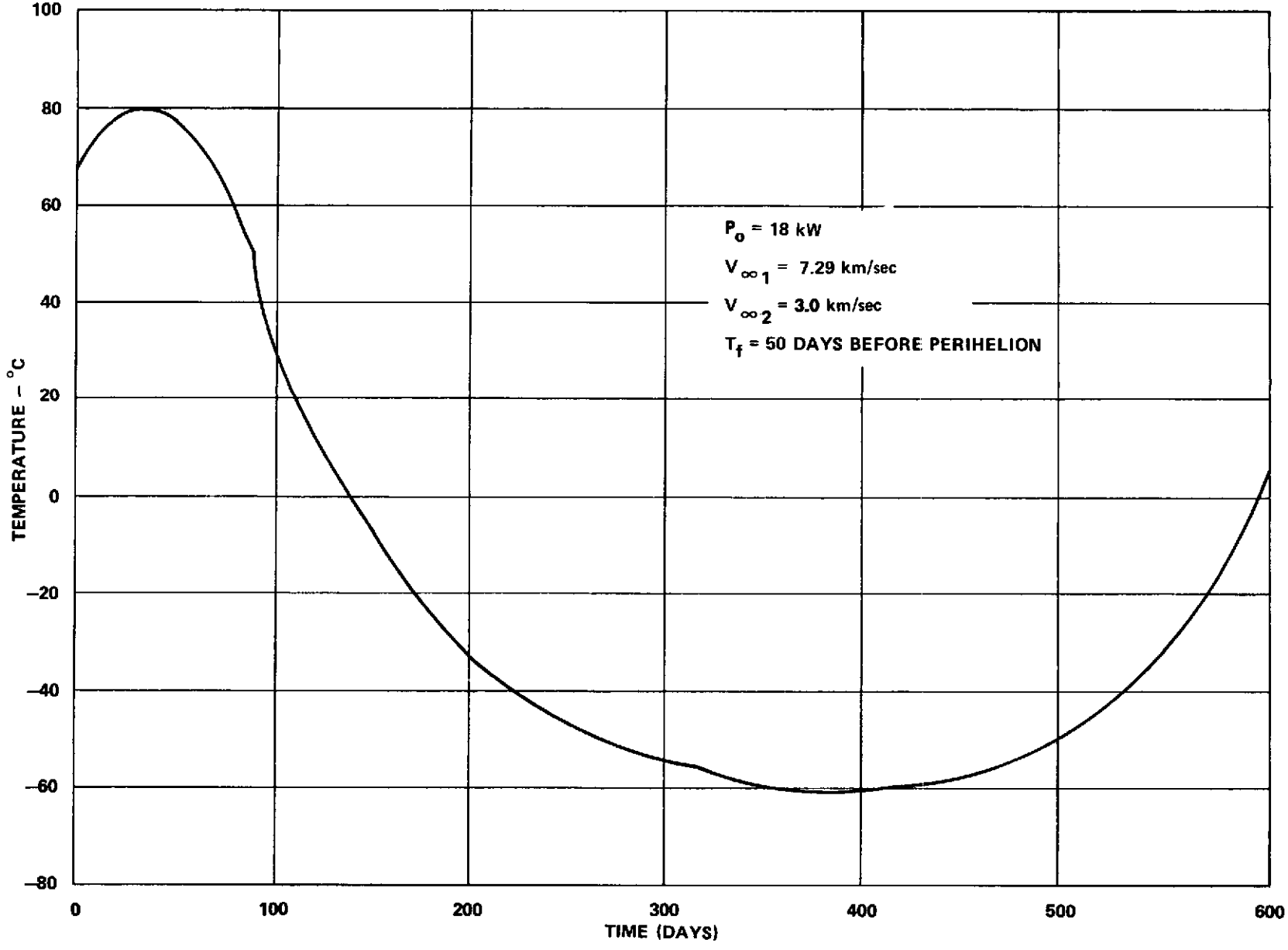

Figure 20. Solar-array substrate temperature vs time for a SEPS comet Encke flyby mission (preliminary).

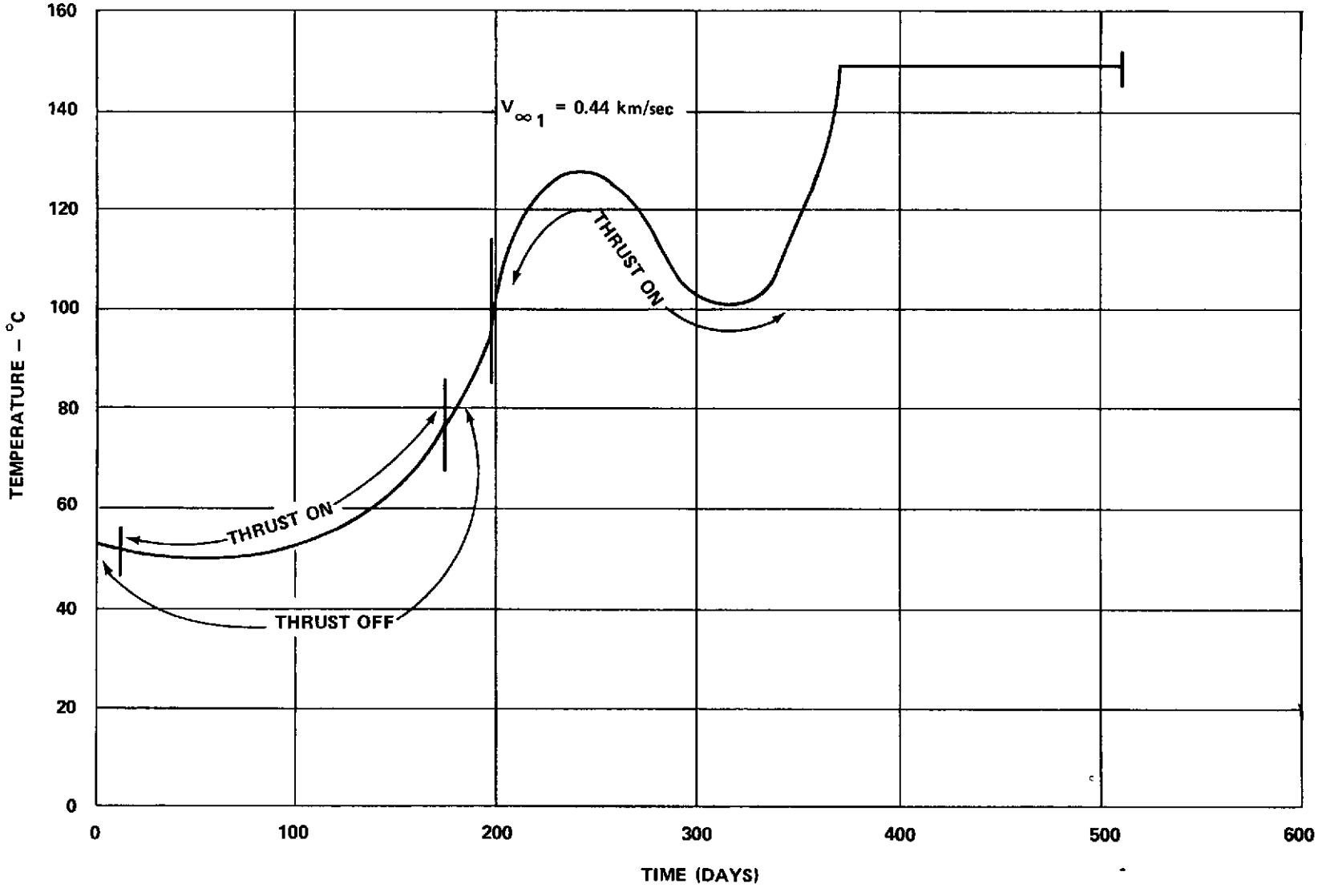

Figure 21. Solar-array substrate temperatures vs time for a SEPS Mercury orbiter mission (preliminary).

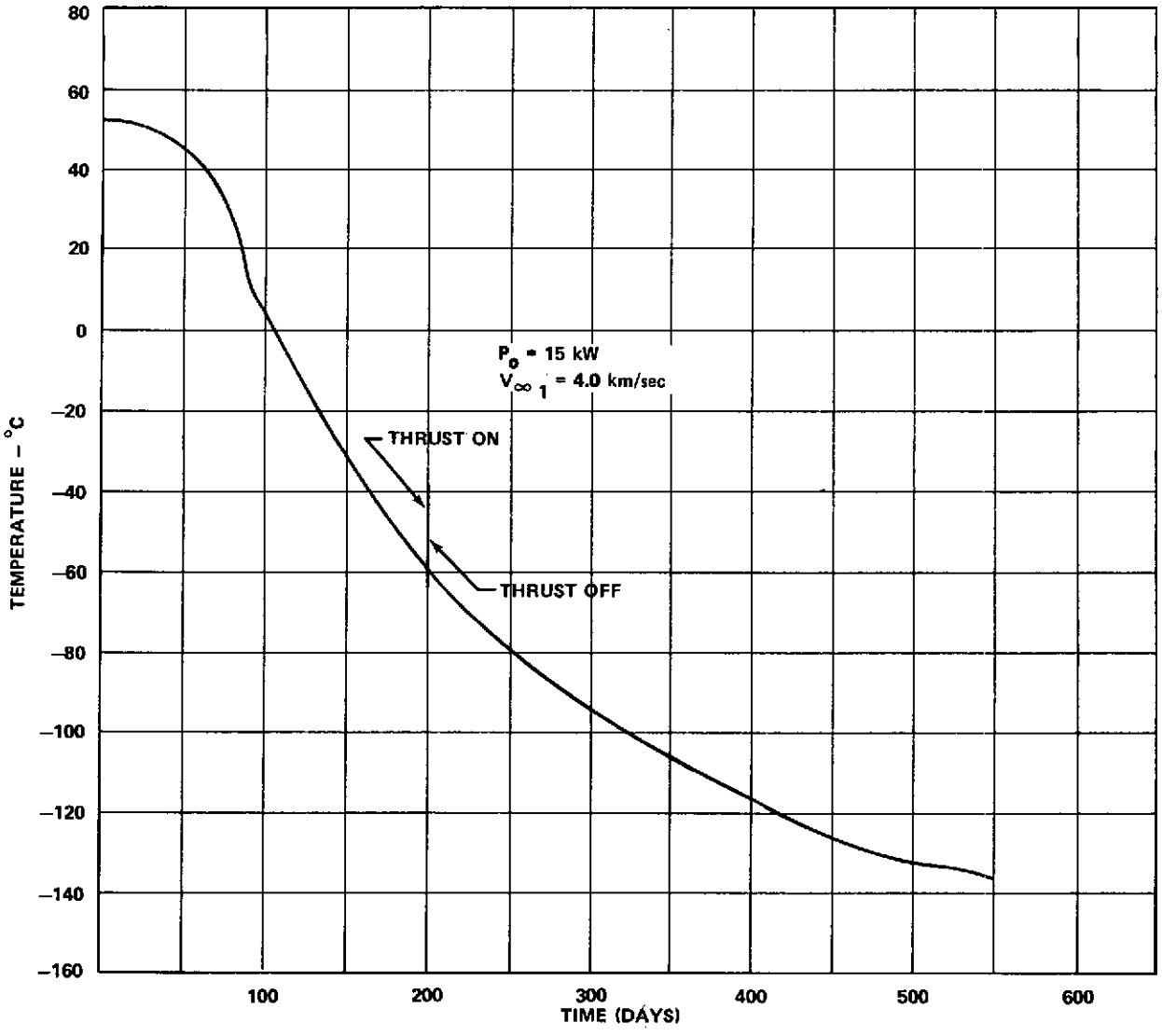

Figure 22. Solar-array substrate temperatures vs time for a SEPS Jupiter flyby mission (preliminary).

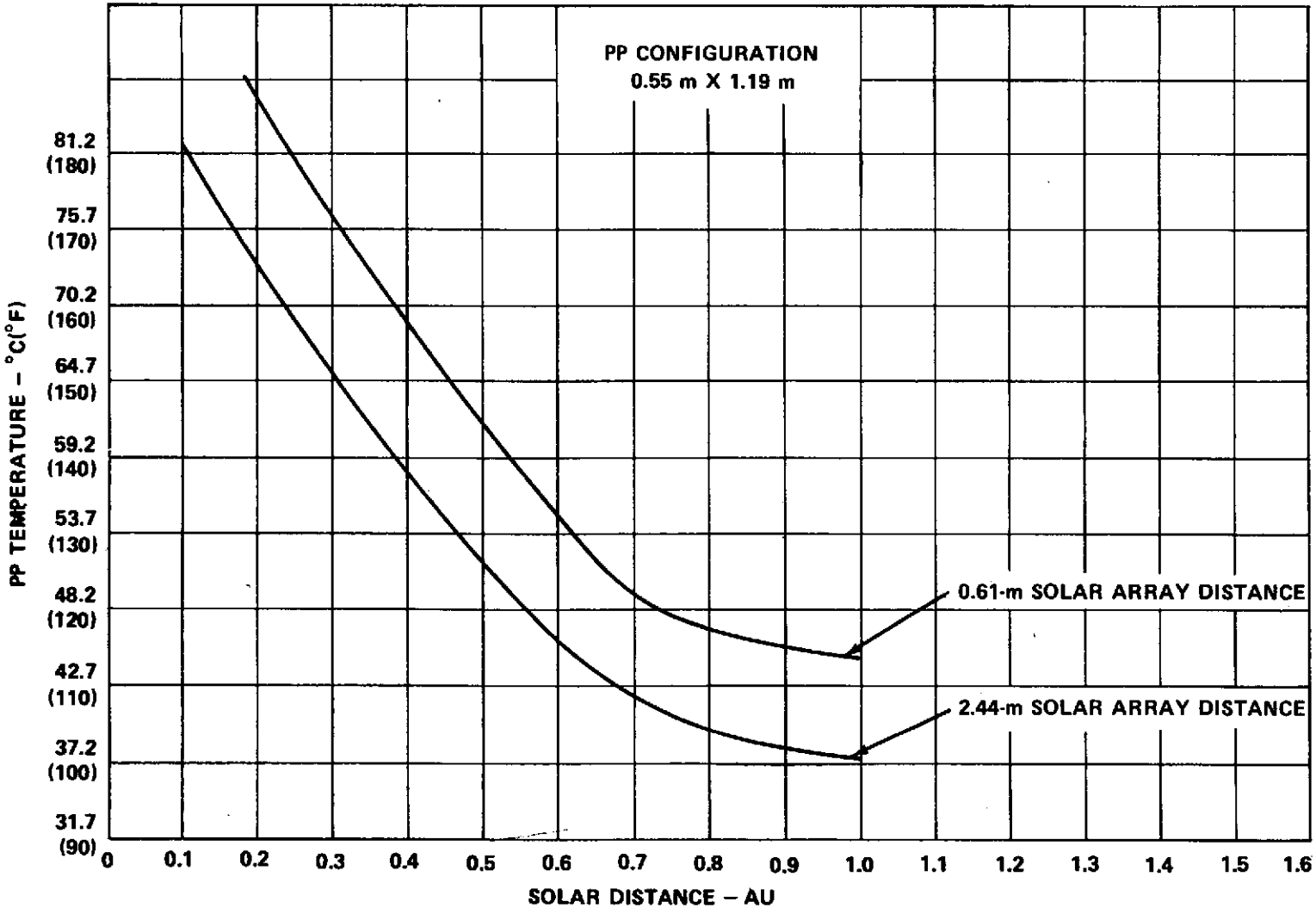

Figure 23. Preliminary power processor (PP) temperatures for a fixed-size surface area (0.65 m^2) and varying solar-array distances from PP as a function of spacecraft distance from the sun.

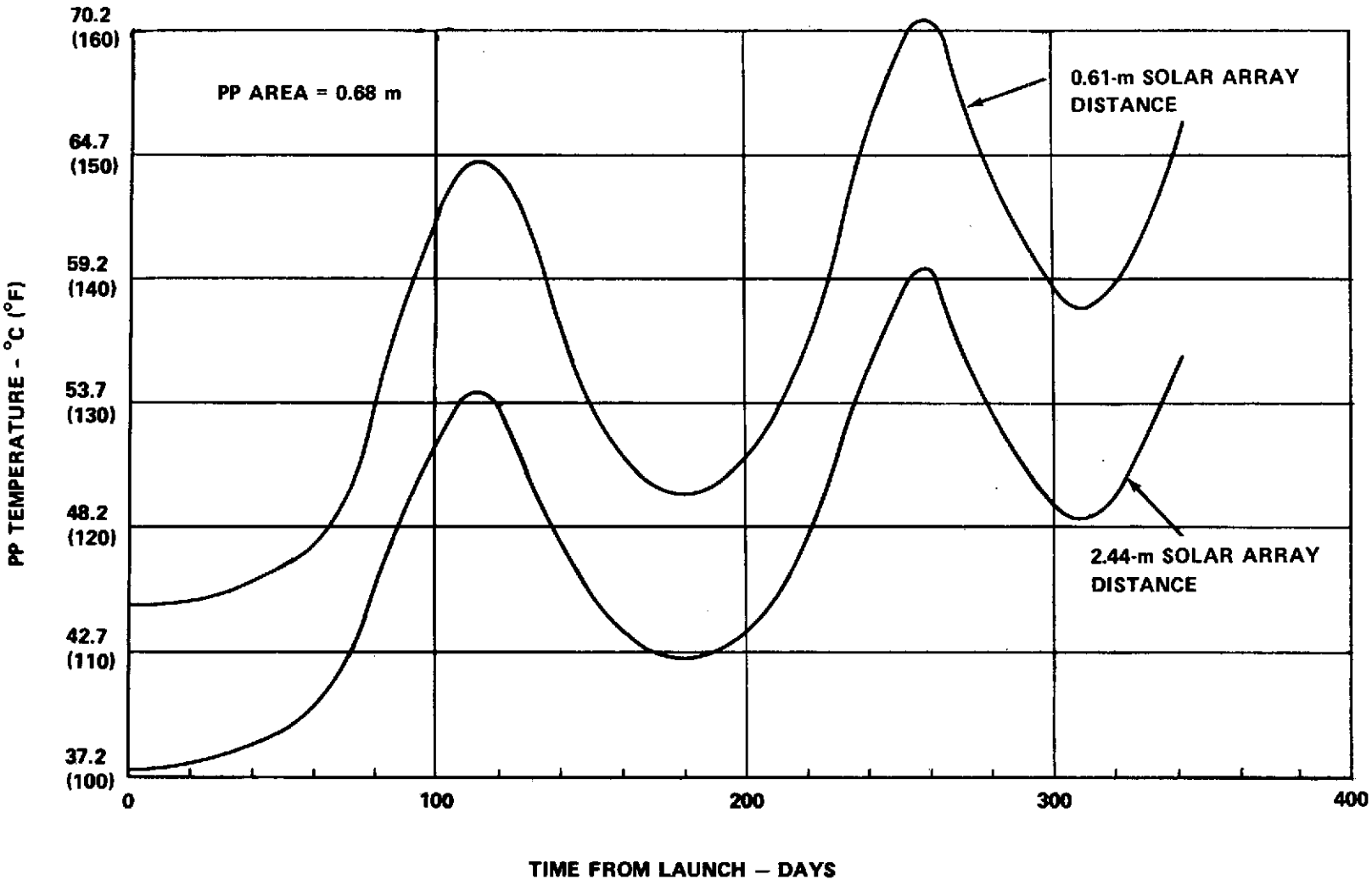

Figure 24. Preliminary power processor (PP) temperatures as a function of time for a SEPS Mercury orbiter mission using PP configuration specified.

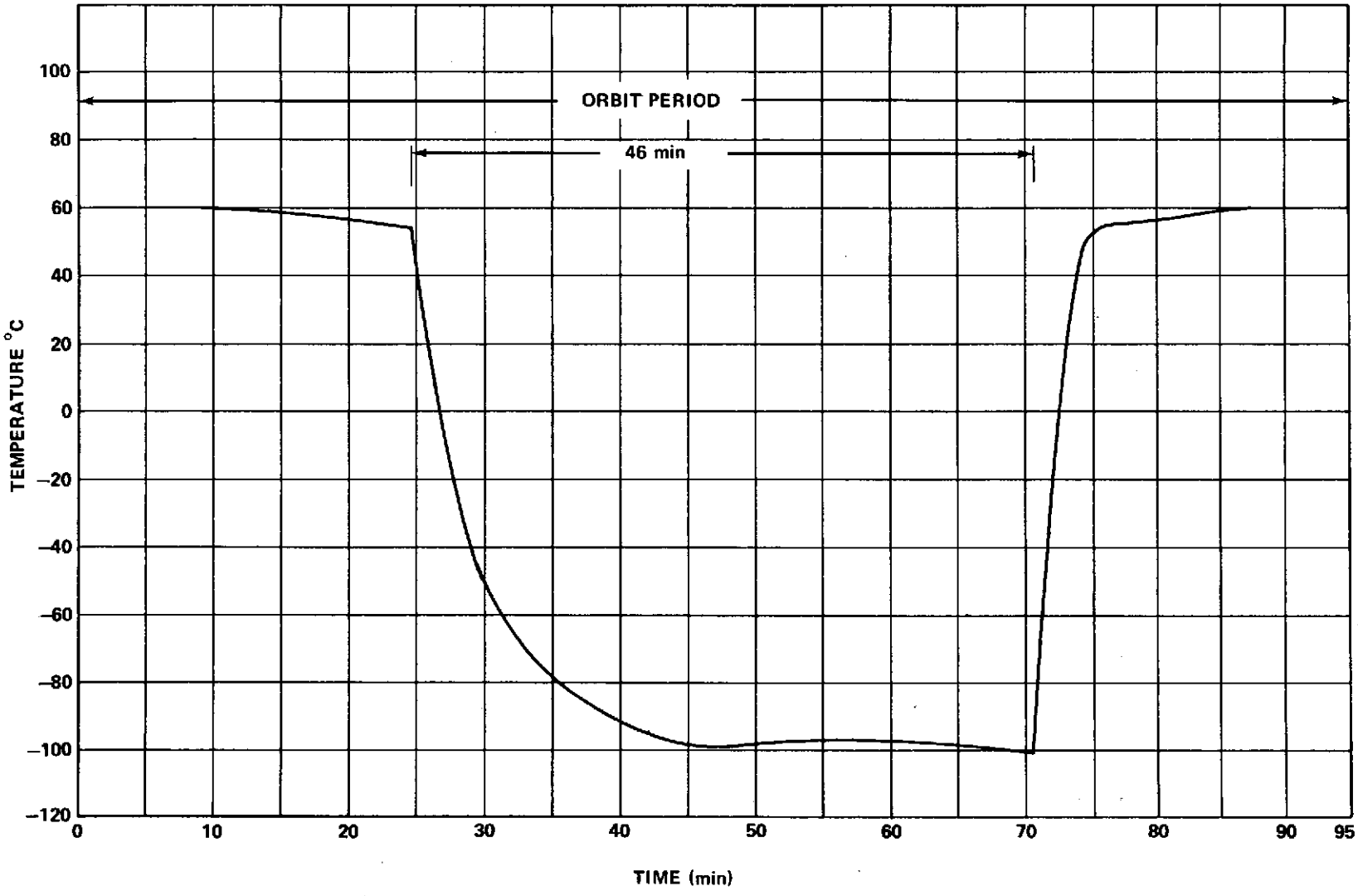

Figure 25. Solar-array temperature variation extremes due to earth-orbital shadowing at a 500-km altitude and array normal to sun (β = 0 deg).

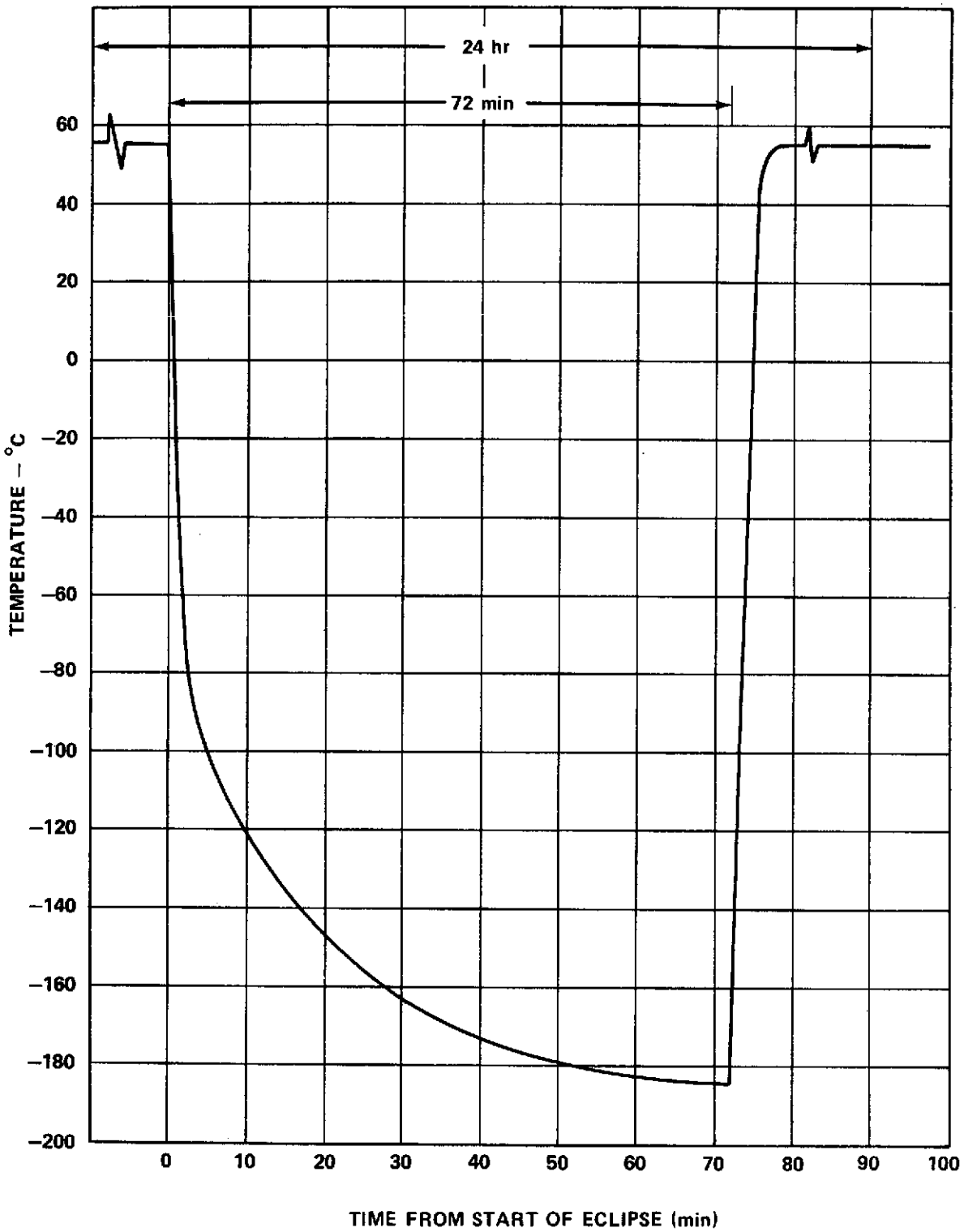

Figure 26. Solar-cell temperatures — SEPS solar array — β = 0 deg, 72-min eclipse, geosynchronous equatorial orbit, array normal to sun.

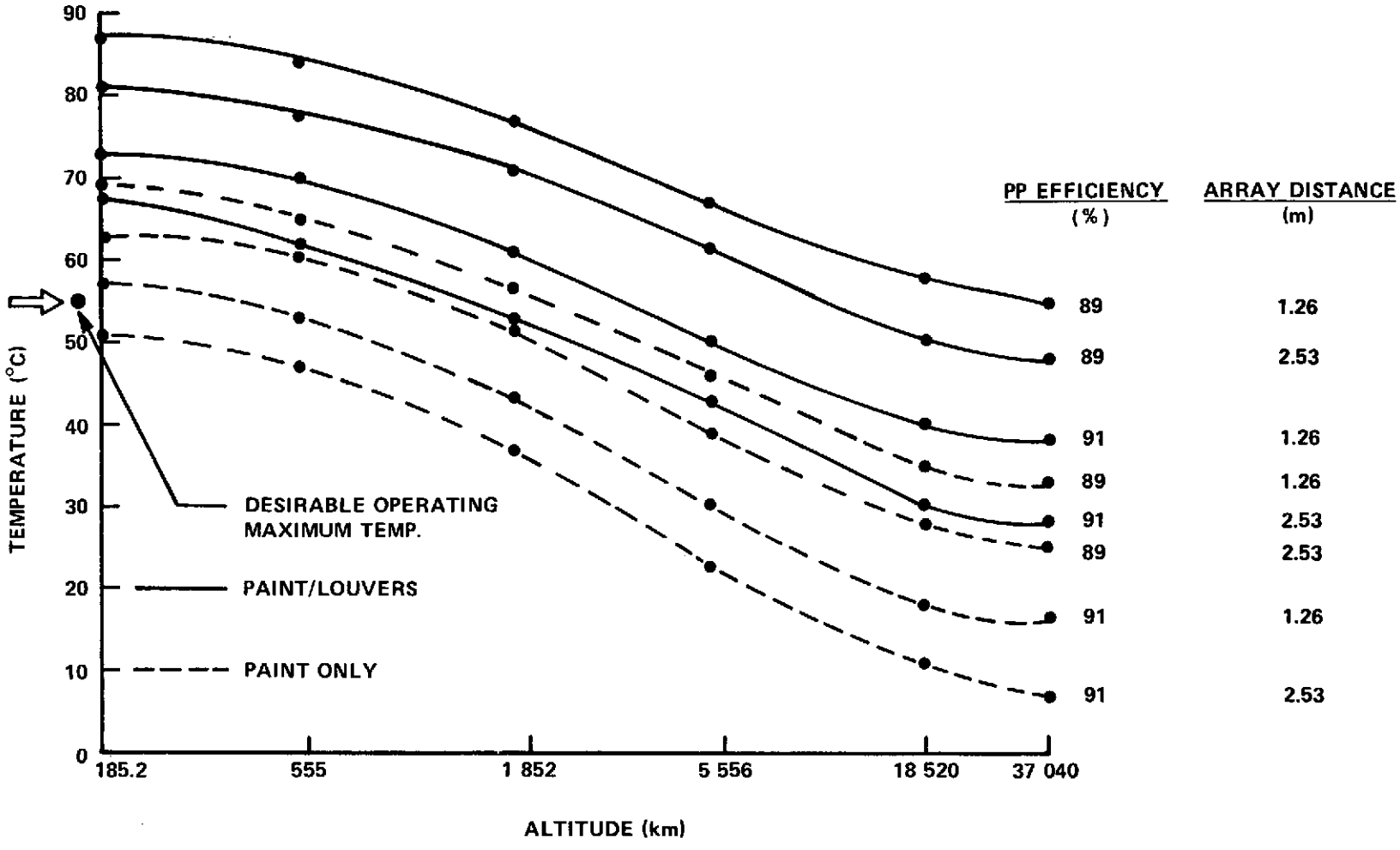

Figure 27. Power processor (PP) radiator surface temperatures for a 1.0-m^2 baseline PP surface area as a function of operating altitude.

solar-array temperature of 50° C, (3) a light power processor configuration with maximum heat leak into each PP of 15 W (other than from solar array), and (4) a 20° C maximum gradient on the radiator surface.

The varying parameters as indicated on Figure 27 include power processor efficiency and array distance from the power processor, along with reflective paint and louver combinations. The purpose of the louvers is to prevent excessive heat leaks when the concern is minimum temperature constraints on some missions. However, the presence of louvers increases maximum operating temperatures significantly for low earth orbits. Louvers also increase the weight of a power processor by approximately 20 to 25 percent.

The maximum desirable radiator surface temperature of 55° C along with the assumption of a ± 10° C temperature gradient mean that peak temperatures of 65° C may be expected, according to these analyses. At present, a maximum of 65° C surface-area temperature satisfies the maximum allowable temperature constraints associated with other components of the SEPS baseline power processor. It should be emphasized that these preliminary SEPS thermal analyses are intended to point out serious problem areas affecting stage and component design and to suggest ways to deal with severe environmental extremes associated with some projected SEPS missions.

Additional information concerning the electromagnetic environment and other atmospheric thermal properties may be found in References 11 and 12.

(6) Thruster and Power Conditioner Thermal Tests at Lewis Research Center and Jet Propulsion Laboratory. Thermal tests and analyses for the SEPS baseline 30-cm mercury ion thruster and power processors are currently underway at LeRC, JPL, and MSFC. The Lewis Research Center's effort includes an updated thermal analysis of the Solar Electric SERT II Rocket Test Flight in 1970.[8] Preliminary indications of some of the data are that some component temperatures during flight were as much as 25 percent higher than predicted by earlier thermal modeling of the system, i.e., about 93° C. Modifications of the analytical model have produced better agreement with the flight data and discrepancies at present are about 10 percent (according to LeRC).

8. Presentation by LeRC representatives at MSFC during AST Technical Working Group meeting on April 1, 1974.

Heat-rejection problems associated with thrusters operating in clusters are currently being studied by LeRC and JPL, as presented in the work referenced in footnote 5. Preliminary baseline configurations include a 2-by-N and a 3-by-3 thruster array. Preliminary indications are that since most of the generated heat is expended out of the rear of the thrusters, the clustering of thrusters is a feasible concept. The thruster arrays are simulated at LeRC by providing heated baffles over a wide temperature range which surrounds the engineering test model thruster. Thruster body temperature rises range up to 30° C for baffle temperatures of up to 200° C, considering a no-sun influence on background temperatures.

Figure 28, which shows a comparative thermal study by JPL on thruster clustering, gives some interesting results when the thruster array is subjected to the effect of sun rays incident on the rear end of the thrusters. These tests were conducted with the engineering model thruster operating at 2 A. Instead of a thruster body temperature increase of about 30° C over a background temperature range of 0° C to 200° C, some thruster components' temperatures showed an increase of about 57° C over the same background temperature environment and when further subjected to the equivalence of 2 sun illumination incident on the rear of the thrusters. A cerium chord lamp, providing up to 3 sun illumination, was used as the solar simulator. The results of such tests should reveal relative thruster and component performances when subjected to these environments. Significant SEPS performance degradation may result when considering the impact of optimum thrust vector pointing requirements along with thruster pointing thermal constraints over the range of the SEPS mission model.

The LeRC thruster thermal tests indicate thruster restarts from temperatures as low as -95° C. Further information on the delay in startup time will be forthcoming. Of specific interest are thruster startup delays while operating in geosynchronous eclipse conditions, which cause solar-array temperatures to be as low as -196° C.

c. Pressure.

(1) Electromagnetic Radiation Pressure. Electromagnetic radiation pressure is apparently the dominant environmental pressure for interplanetary cruise conditions; however, large solar-flare events and cometary encounter environments could become of great concern for some projected SEPS missions. Electromagnetic radiation pressure has a range at 1 AU from 4.5×10^{-6} to 9.02×10^{-6} N/m^2, depending on the reflective properties of the spacecraft and component surface. A $1/R^2$ variation is assumed. A full-capability SEPS base-

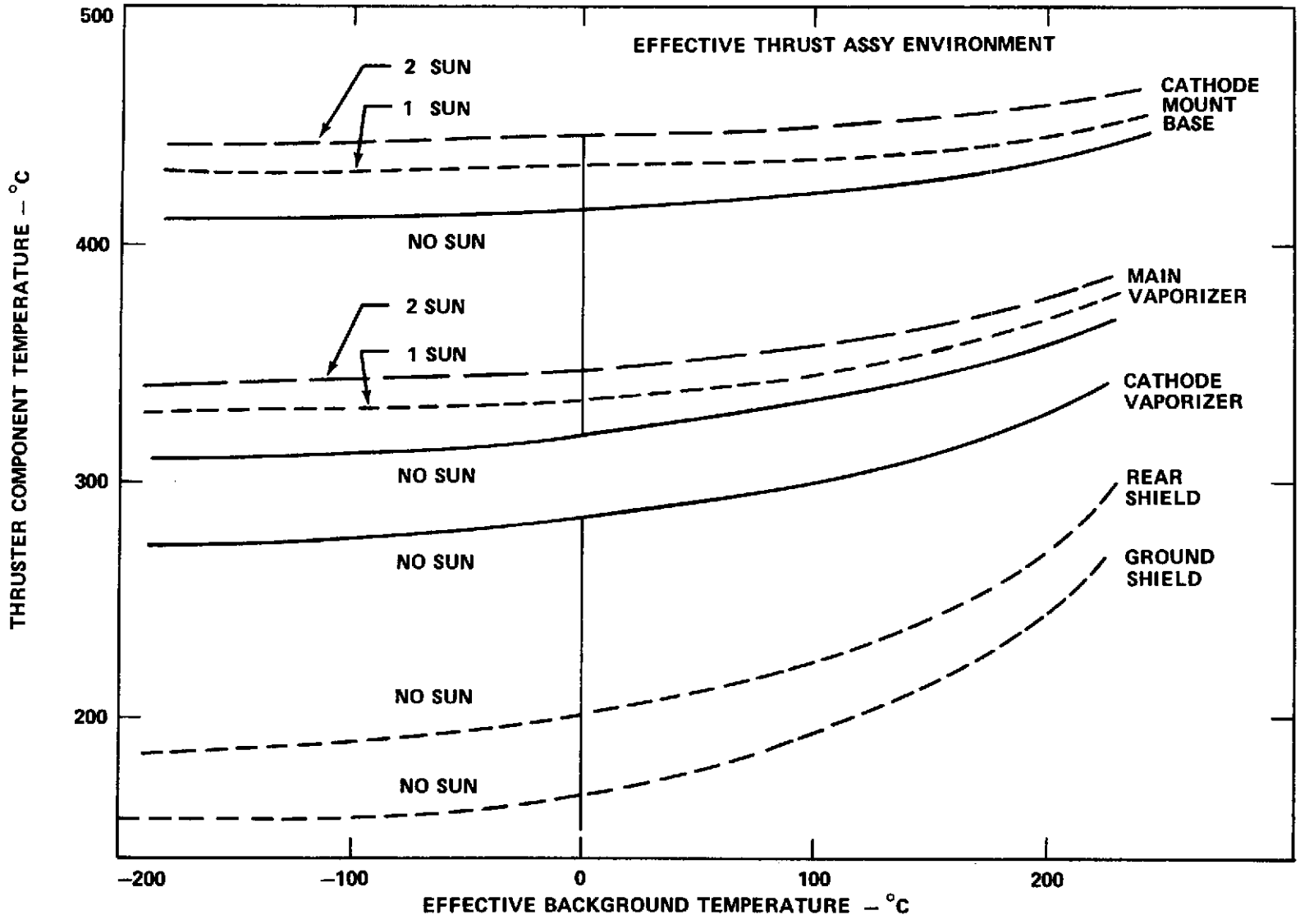

Figure 28. Preliminary results of JPL engineering model 30-cm thruster (EMT) thermal performance at 2 A.

line solar array has an approximate 250-m^2 surface area. Thus, using a baseline propulsion thrust level for seven full-power baseline thrusters, electromagnetic radiation pressure is expected to have a range of 0.2 to 3 percent of this thrust level at 1 and 0.3 AU respectively.

(2) Solar-Wind Pressure. Quiet sun solar-wind proton pressure is considerably less than the electromagnetic radiation pressure, being about 1.5×10^{-9} N/cm^2 at 1 AU. However, for large solar-flare events, this pressure is increased probably by orders of magnitude and may become a significant factor in spacecraft performance, especially at close solar distances.

Solar-wind electron pressure, which is smaller and omnidirectional compared with the radially directed solar proton pressure, has a range of 1×10^{-12} to 3×10^{-11} N/cm^2 during normal quiet sun activity.

(3) Neutral Gas Pressure. The composition of netural kinetic gases in interplanetary space is primarily hydrogen, proton, helium, and alpha particles. Pressure produced by these gases is on the order of 1×10^{-11} N/m^2 for a general cruise environment; however, for comet-tail encounter environments, these gas pressures may exceed 10^5 N/m^2, as indicated by JPL for the comet Encke (see footnote 5). The total pressure on the spacecraft may be reduced by several orders of magnitude by retracting the solar array.

(4) Atmospheric Drag. Atmospheric drag for low earth-orbital SEPS missions could become a factor because of the large solar-array surface areas. In fact, drag force would equal the full-capability SEPS thrust level at altitudes of from 185 to 222 km (100 to 120 n.mi.). This means essentially that there would be little or no orbit-raising capability. However, at initial altitudes of 555 km (300 n.mi.) and higher, drag effect has fallen to an almost negligible factor, being on the order of 8.9×10^{-3} N or effectively 1 percent of the spacecraft's thrust level.

(5) Perturbing Effects on Vehicle Dynamic and Attitude Control. From a vehicle performance and mission analysis standpoint, the effects of these environmental pressures will have to be assessed as a function of specific missions for the SEPS. It is possible, however, that normally expected trajectory perturbing influences will be far greater than the effects of these specific pressures. Attitude control and other vehicular dynamics will be influenced by these pressures to some extent.

d. Cometary and Asteroidal Meteoroids.

(1) Cometary Meteoroids. The large surface area of a SEPS solar array (250 m^2) and the need to minimize changes in surface properties necessitate some concern about meteoroids. The particle fluxes and masses of most of these encountered meteoroids are small enough so that the penetration power of these particles is negligible. Nevertheless, particles with a mass of 10^{-6} gm are sufficiently abundant to cause degradation effects to the solar-array surfaces. The flux of these cometary particles is about 10^{-8} particles/m^2-sec. Cometary meteoroids that are not members of a stream have an apparent isotropic distribution. At 1 AU, a 10^{-2}-gm cometary meteoroid can penetrate approximately 400 mils of aluminum but the flux of such particles is about 10^{-12} particles/m^2 sec, rendering the encounter probability quite small even for long-duration missions. In fact, it is possible that not one particle of this size will hit the solar array at 1 AU for a 5-year SEPS mission lifetime. Since shield thicknesses for solar arrays are baselined at 6 to 12 mils, cometary particles with lower masses and higher flux intensities may cause some concern during some SEPS missions.

(2) Asteroidal Meteoroids. Asteroidal meteoroids have relatively higher densities than cometary ones, i.e., up to 8 gm/cm^3 compared with 0.5 gm/cm^3. Because of this density differential, approximately 10 mils more of aluminum are required to stop asteroidal particles than are required to stop cometary particles for an equivalent mass of 10^{-5} gm. Most asteroidal particles have heliocentric orbits lying between Mars and Jupiter but a few have orbits reaching > 5 AU. Since at 1 AU the flux of cometary particles of equivalent masses is several orders of magnitude greater than asteroidal particles, the probability of solar-array encounter is negligible. However, at 3-AU distance, asteroidal particles with masses greater than 10^{-3} gm show a significant increase in population with a flux of approximately 4×10^{-10} particles/m^2 sec. For additional information on meteoroids, see References 11 and 12.

e. Magnetic Fields. The maximum geomagnetic field for SEPS cruise environments extending out to 10 earth radii will not be greater than $5 \cdot 10^{-5}$ T. Interplanetary magnetic fields are small, i.e., approximately 10^{-8} T at 1 AU. The external magnetic field of the sun changes with time and solar activity. For quiet-sun conditions the solar magnetic field exhibits a spiral pattern in the ecliptic plane with a radial and angular component. This angular component is about 45 degrees at 1 AU. During solar-flare activity, the interplanetary magnetic field becomes distorted and influences the bounds of the earth's magnetosphere. For more details on magnetic-field environments, see References 11 and 12.

2. INDUCED CRUISE ENVIRONMENTS

Specific values for induced cruise environments will be forthcoming as an agreed-upon preliminary design of the SEPS or module emerges from the total SEP/AST development programs.

The solar arrays will produce electrical and magnetic fields and generate heat that will affect other components of the stage. The thrusters will exhaust mercury ions at the rate of 0.03 gm/sec from an initial propellant tank capacity of approximately 1500 kg for a full-capability SEPS. Each thruster will emit approximately 6×10^{15} molybdenum ions per second from the grid. Plume impingement, resulting from thruster-array configuration and actuator gimbaling techniques, will also cause aluminum contamination on spacecraft surfaces. The JPL engineering model thruster testing (see footnote 5) has indicated that up to 2 mils of aluminum and molybdenum contamination may accumulate on other spacecraft surfaces during 1000 hours of thruster operation. Thus, the accumulated thickness is about 10^4 nm (10^5 Å) whereas 1 nm (10 Å) can affect the thermal properties of some surfaces. These potential problems are being addressed in detail by the AST and other MSFC SEPS activities.

Problems associated with mission aborts, launch-vehicle failures, and possible mercury-tank ruptures in the Shuttle cargo bay are also being investigated. Studies are under way concerning possible environmental impacts for the general public as well as launch operation crews and power processor heat generation characteristics are also being studied.

B. Planetary Natural and Induced Environments

Because the SEPS mission model is tentative, it is not practical to include the environments associated with all possible SEPS planetary missions. However, much of the information needed for preliminary performance is available in References 10 through 12.

SECTION III. CONCLUSIONS

In this report the analyses have been focused on the possible degrading effects of the natural space environments (near earth and interplanetary) on candidate baseline configurations and concepts of a SEPS and related subsystem components.

Potential system/subsystems performance problem areas have been identified as being associated with the specific mission model used.

A hazardous near-earth charged-particle operating zone of from 1852 km to 14 000 km (1000 to 7500 n.mi.) which impacts subsystem design considerations, particularly the high-powered solar arrays, has been identified. This "hot" radiation zone produces excessively high power degradations over short periods of time in the solar-cell arrays, which results in considerable performance anomalies for the SEPS spacecraft operating in this region.

Much of the data presented in these analyses has a potentially broad application to solar-electric-propulsion-oriented spacecrafts and payloads, as well as conventional spacecrafts and payloads.

For increased reliability and a high mission success probability, system/subsystem designers should consider these and similar analyses as valuable input impacting the final design considerations.

APPENDIX A

ANALYTICAL APPROXIMATION METHODS FOR OPTIMIZED LOW-THRUST TRAJECTORY GENERATION

Summary

The following analyses describe a method for analytically approximating solutions to the problems of optimum low-thrust steering and trajectory generation for a solar electric or nuclear propulsion space vehicle. The computational results of these methods have been compared with solutions obtained by exact calculus-of-variation methods with a high degree of accuracy. One immediate advantage of analytical methods is that the computer time requirement for comparable problem solutions is reduced by orders of magnitude. These analytical methods are also more easily applied to problems which consider the effects on trajectory shaping due to solar-cell degradation and thrust loss from Van Allen charged-particle radiation. The thrust vector pointing or steering profile dictated by these approximation methods is considerably softer than that required by exact optimum solutions.

Earth-orbital SEPS vehicle dynamics and performance studies have indicated that because of manuever rate requirements with expected thrust levels, a softer-than-optimum steering profile will have to be considered for some projected SEPS missions. Thus the steering requirements of the approximation methods become more realistic even though there is a slight degradation in performance, depending on the initial orbital parameters.

The Lagrangian perturbation equations as derived in Reference 5 are repeated below. These six linear differential equations define the time rates of change of the defining orbital elements as a function of the particular nature of the perturbing function R.

$$\dot{a} = \frac{2}{na} \frac{\partial R}{\partial M} \cdot \tag{A-1}$$

$$\dot{e} = \frac{1}{na^2 e} \left[(1-e^2) \frac{\partial R}{\partial M} - (1-e^2)^{1/2} \right] \frac{\partial R}{\partial \omega} \tag{A-2}$$

$$\dot{M} = n - \left(\frac{1-e^2}{na^2e}\right)\frac{\partial R}{\partial e} - \frac{2}{na}\left(\frac{\partial R}{\partial a}\right)_M \tag{A-3}$$

$$\dot{\Omega} = \frac{1}{na^2\,(1-e^2)^{1/2}\sin i}\,\frac{\partial R}{\partial i} \tag{A-4}$$

$$\dot{\omega} = \left[\frac{-\cos i}{na^2 \sin i\,(1-e^2)^{1/2}}\right]\frac{\partial R}{\partial i} + \left[\frac{(1-e^2)^{1/2}}{na^2 e}\right]\frac{\partial R}{\partial e} \tag{A-5}$$

$$\frac{di}{dt} = \left[\frac{\cos i}{na^2 \sin i\,(1-e^2)^{1/2}}\right]\frac{\partial R}{\partial \omega} - \left[\frac{1}{na^2 \sin i\,(1-e^2)^{1/2}}\right]\frac{\partial R}{\partial \Omega} \tag{A-6}$$

where a, e, M, Ω, ω, and i are classical orbital elements and n is the orbital mean motion.

Forces acting on an orbiting body which dictate the explicit mathematical form of the perturbing function partials may be in the form of specifically defined low-thrust force vectors referenced to an inertial orthogonal coordinate system.

The inertial coordinate reference frame used in these analyses is shown in Figure A-1.

To expedite the generation of a low-thrust trajectory it is necessary to resolve the thrust force vector $\overline{F}$ into component magnitudes F_1, F_2 and F_3 along the desired set of orthogonal axes.

Using the coordinate system shown in Figure A-1, a rotating orthogonal set of unit vectors is defined along the radial $\overline{x}_r$, transverse $\overline{y}_\theta$ and orthogonal $\overline{z}_a$ directions.

$$\begin{pmatrix} \overline{x}_r \\ \overline{y}_\theta \\ \overline{z}_a \end{pmatrix} = \begin{pmatrix} \cos\omega^* & \sin\omega^* & 0 \\ -\sin\omega^* & \cos\omega^* & 0 \\ 0 & 0 & 1 \end{pmatrix} \begin{pmatrix} 1 & 0 & 0 \\ 0 & \cos i & \sin i \\ 0 & -\sin i & \cos i \end{pmatrix} \begin{pmatrix} \cos\Omega^* & \sin\Omega^* & 0 \\ -\sin\Omega^* & \cos\Omega^* & 0 \\ 0 & 0 & 1 \end{pmatrix} \begin{pmatrix} \overline{i} \\ \overline{j} \\ \overline{k} \end{pmatrix}. \tag{A-7}$$

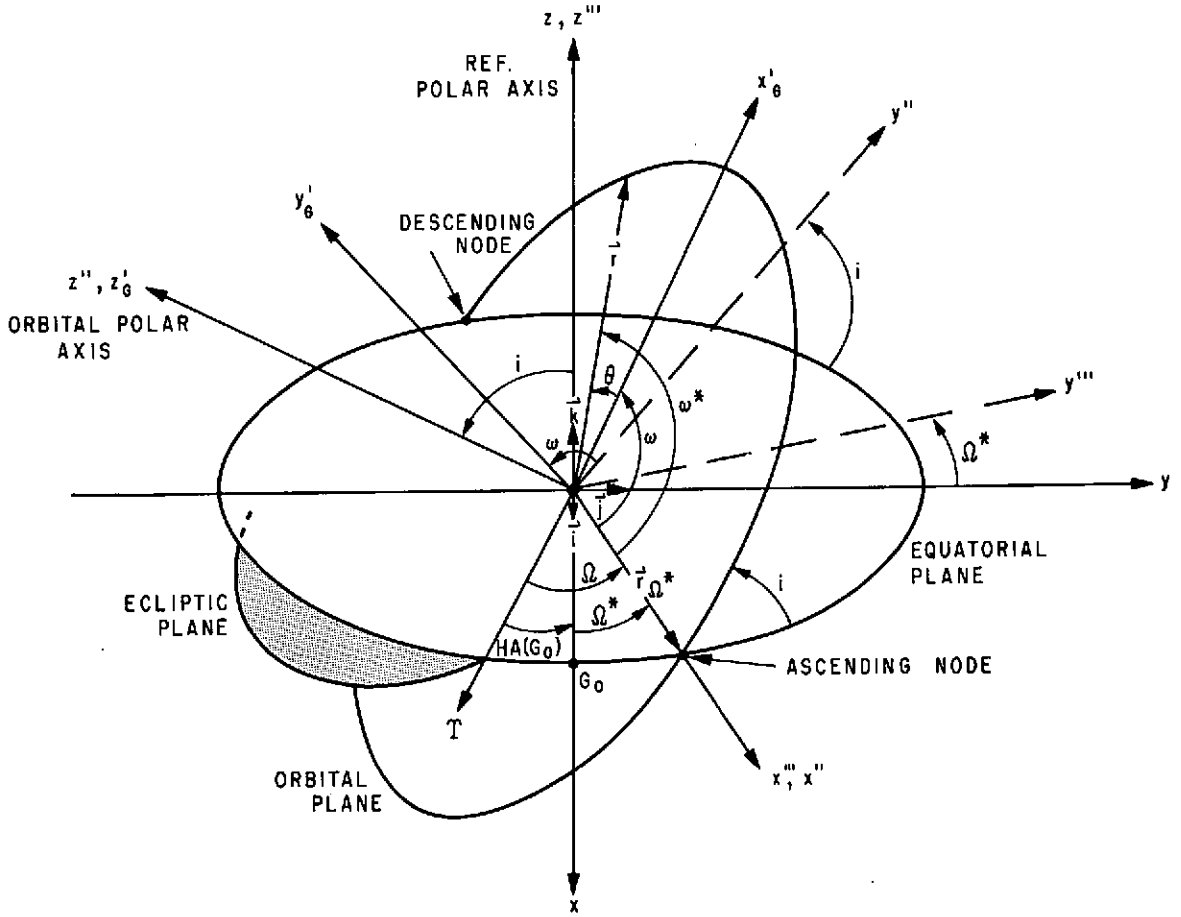

Figure A-1. Geocentric reference coordinate system.

Thus a thrust force vector $\overline{F}$ at any point in the orbit may be resolved into its component parts by

$$\overline{F} = F_1 \overline{x}_r + F_2 \overline{y}_\theta + F_3 \overline{z}_a \quad . \tag{A-8}$$

$\overline{F}$ is further resolved into component magnitudes with respect to the inertial reference frame defined by Figure A-1 as the set of unit vectors,

$$\begin{pmatrix} \bar{P} \\ \bar{Q} \\ \bar{R} \end{pmatrix} = \begin{pmatrix} \cos\omega & \sin\omega & 0 \\ -\sin\omega & \cos\omega & 0 \\ 0 & 0 & 1 \end{pmatrix} \begin{pmatrix} 1 & 0 & 0 \\ 0 & \cos i & \sin i \\ 0 & -\sin i & \cos i \end{pmatrix} \begin{pmatrix} \cos\Omega^* & \sin\Omega^* & 0 \\ -\sin\Omega^* & \cos\Omega^* & 0 \\ 0 & 0 & 1 \end{pmatrix} \begin{pmatrix} \bar{i} \\ \bar{j} \\ \bar{k} \end{pmatrix} \tag{A-9}$$

where the difference between ω and ω^* is just the true anomaly angle θ,

$$\omega^* = \omega + \theta \quad . \tag{A-10}$$

Since the transformation indicated by matrix equation (A-9) also represents the transformation to orbital axes coordinates X_0, Y_0 and Z_0, the following relationship may be designated: $\bar{P}$ lies along X_0, $\bar{Q}$ along Y_0, and $\bar{R}$ along Z_0. Thus an inertial position may be written as

$$\bar{r} = X_0 \bar{P} + Y_0 \bar{Q} \tag{A-11}$$

where

$$X_0 = r\cos\theta = a\cos E - a e \tag{A-12}$$

$$Y_0 = r\sin\theta = a(1-e^2)^{1/2}\sin E \quad . \tag{A-13}$$

The components of the acceleration force $\bar{F}$ from equation (A-8) may be expressed in ∇ operator form as a function of the perturbing function R as

$$\nabla R = \frac{\partial R}{\partial x}\bar{i} + \frac{\partial R}{\partial y}\bar{j} + \frac{\partial R}{\partial z}\bar{k} = \bar{F} \quad .$$

Also, the partial derivatives of the perturbing function R with respect to the orbital elements α_i may be written as derived in Reference 5 as

$$\frac{\partial R}{\partial \alpha_i} = \nabla R \cdot \frac{\partial \bar{r}}{\partial \alpha_i} = \bar{F} \cdot \frac{\partial \bar{r}}{\partial \alpha_i} \quad ; \quad (i = 1, 2, \ldots 6) \; . \tag{A-14}$$

Using equation (A-11) we now have

$$\frac{\partial R}{\partial \alpha_i} = \bar{F} \cdot \bar{P} \frac{\partial X_0}{\partial \alpha_i} + \bar{F} \cdot \bar{Q} \frac{\partial Y_0}{\partial \alpha_i} \quad ; \quad (i = 1, 2, \ldots 6) . \tag{A-15}$$

The relationship between the inertial unit vectors $\bar{P}$, $\bar{Q}$, $\bar{R}$ and the rotating unit vectors $\bar{x}_r$, $\bar{y}_\theta$, $\bar{z}_a$ may be expressed as the simple rotation,

$$\begin{pmatrix} \bar{P} \\ \bar{Q} \\ \bar{R} \end{pmatrix} = \begin{pmatrix} \cos\theta & -\sin\theta & 0 \\ \sin\theta & \cos\theta & 0 \\ 0 & 0 & 1 \end{pmatrix} \begin{pmatrix} \bar{x}_r \\ \bar{y}_\theta \\ \bar{z}_a \end{pmatrix} \; . \tag{A-16}$$

Thus the following scalar products are obvious:

$$\bar{F} \cdot \bar{P} = \frac{1}{r} (F_1 X_0 - F_2 Y_0) \tag{A-17}$$

$$\bar{F} \cdot \bar{Q} = \frac{1}{r} (F_1 Y_0 + F_2 X_0) \; .$$

Equation (A-15) now takes the form,

$$\frac{\partial R}{\partial \alpha_i} = \frac{1}{r} (F_1 X_0 - F_2 Y_0) \frac{\partial X_0}{\partial \alpha_i} + \frac{1}{r} (F_1 Y_0 + F_2 X_0) \frac{\partial Y_0}{\partial \alpha_i} \quad ; \quad (i = 1, 2, \ldots 6) . \tag{A-18}$$

Performing the above partial derivatives with respect to each of the six orbital elements a, e, M, Ω, ω, and i; recalling also that X_0 and Y_0 are functions of a, e, and M and not of Ω, ω, and i, and that from equation (A-16) the unit vectors $\bar{R}$ and $\bar{z}_a$ coincide, the explicit mathematical forms are developed and substituted into equations (A-1) through (A-6). This yields the time rates of change of an initial set of orbital elements a_0, e_0, M_0, Ω_0, ω_0, and i_0 as a function of a low-thrust force vector resolved into inertial orthogonal components F_1, F_2, and F_3.

$$\dot{a} = \frac{2a^2}{(\mu p)^{1/2}} [F_1 e \sin\theta + F_2(1 + e\cos\theta)] \tag{A-19}$$

$$\dot{e} = \left(\frac{p}{\mu}\right)^{1/2} [F_1 \sin\theta + F_2(\cos\theta + \cos E)] \tag{A-20}$$

$$\dot{M} = \left[\frac{P\cos\theta - 2re}{(a\mu)^{1/2} e}\right] F_1 - \frac{p\sin\theta}{(a\mu)^{1/2} e}\left[1 + \frac{r}{p}\right] F_2 \tag{A-21}$$

$$\dot{\Omega} = \frac{r}{(\mu p)^{1/2}} \frac{\sin\omega^*}{\sin i} F_3 \tag{A-22}$$

$$\dot{\omega} = \frac{1}{e}\left(\frac{p}{\mu}\right)^{1/2}\left[-F_1\cos\theta + F_2\left(1 + \frac{r}{p}\right)\sin\theta\right] - \frac{r F_3}{(\mu p)^{1/2}} \cot i \sin\omega^* \tag{A-23}$$

$$\frac{di}{dt} = \frac{r F_3}{(\mu p)^{1/2}} \cos\omega^* \tag{A-24}$$

where F_1 is the low-thrust perturbing force component per unit mass along the radius vector, F_2 is the force component normal to the radius vector and in the osculating orbital plane, and F_3 is the force component normal to the orbital plane and in the direction of the unit vectors R and z_a. Also, E is the eccentric anomaly, $p = a(1-e^2)$, $\mu^{1/2} = a^{3/2} n$, and $\omega^* = \omega + \theta$.

For computational application we need the magnitudes of F_1, F_2, and F_3 in acceleration units which for meter-kilogram units become

$$(\text{acceleration})\ \bar{A}(t) = \frac{F_i(t)\ \ (\text{newtons})}{m(t)\ \ (\text{kilograms})} \qquad ; \qquad i = 1,\ 2,\ 3 \quad .$$

An inspection of equations (A-19) through (A-24) reveals a variation in magnitude of the time rates of change for the orbital elements at various points along the orbit. The nature of low-thrust propulsion dictates that the total secular change of any orbital element will be small over one revolution of the orbit. This will allow certain assumptions to be made with the consequence of eliminating the angular dependence in most of these equations, arriving at a constant change over a single revolution.

It is also possible to independently adjust a single orbital element while keeping all other elements constant by selective use of the thrust components F_1, F_2 and F_3 along with a variation or switching of thrust directions at specific points in the orbit, as discussed in Reference 13.

Defining the orbital position as a function of the eccentric anomaly E we have

$$r = a(1-e\cos E) \quad . \tag{A-25}$$

If it is assumed that $\dot{a}$ and $\dot{e}$ are small, it is clear that

$$\frac{dE}{dt} = \left(\frac{\mu}{a}\right)^{1/2} \frac{1}{r} = \frac{n}{1 - e\cos E} \quad . \tag{A-26}$$

Using the fact that

$$\frac{d\alpha_i}{dt} = \frac{d\alpha_i}{dE}\,\frac{dE}{dt} \qquad ; \qquad i = 1,\ 2,\ 3 \ldots 6 \quad , \tag{A-27}$$

along with the relationships between true anomaly θ and eccentric anomaly E, which are

$$\cos \theta = \frac{\cos E - e}{1 - e \cos E} \tag{A-28}$$

and

$$\sin \theta = \frac{(1 - e^2)^{1/2} \sin E}{1 - e \cos E} \quad , \tag{A-29}$$

equations (A-19 through A-24) are transformed from time-dependent equations to integrable forms of the order

$$\Delta\alpha_i = \int_0^{2\pi} f(E)\, dE \quad ; \quad i = 1, 2, 3 \ldots 6 \quad . \tag{A-30}$$

Performing the indicated integrals, simplifying, and dividing the results by one orbital period

$$\Delta t = \frac{2\pi}{n} \quad , \tag{A-31}$$

we arrive at time rates of change for each of the orbital elements for one complete revolution, thereby eliminating periodic variations along each orbit. Thus the time rates of change for the elements become primarily a function of the distance that the orbiting spacecraft is away from the attractive center (earth) as well as functions of the magnitudes of the components of thrust acceleration F_1, F_2 and F_3. We are now able to compute these secular variations as a function of time.

Secular Variations in the Semimajor Axis a and Eccentricity e

$$\frac{\Delta a}{\Delta t} = 2a\left(\frac{p}{\mu}\right)^{1/2} F_2 = \frac{2(1 - e^2)^{1/2}}{n} F_2 \qquad (A-32)$$

$$\frac{\Delta e}{\Delta t} = -\tfrac{3}{2}\left(\frac{p}{\mu}\right)^{1/2} e\, F_2 \quad . \qquad (A-33)$$

For a unidirectional thrust F_2, a simultaneous change in a and e occurs.

The variation of e with a may be obtained from the ratio of equations (A-32) and (A-33) which gives

$$\frac{\Delta e}{\Delta a} = -\frac{3e}{4a} \quad , \qquad (A-34)$$

which integrates to

$$e = e_0\left(\frac{a_0}{a}\right)^{3/4} \qquad (A-35)$$

where e_0 and a_0 are the initial values of eccentricity and the semimajor axis.

Equation (A-32) may now be rewritten as

$$\frac{\Delta a}{\Delta t} = \frac{2}{n}\left[1 - e_0^2\left(\frac{a_0}{a}\right)^{3/2}\right]^{1/2} F_2 \quad . \qquad (A-36)$$

It is evident from these approximations that F_2 is the only thrust component that produces secular changes in either a or e. In fact, maximum thrust in the direction of F_2 is optimum for orbit raising and reducing if it is not desirable to change the orientation of the orbit. Note, however, that the F_2 direction is by definition tangential only for circular orbits.

During many conceivable low-thrust missions, it may be highly desirable to vary the semimajor axis a and the eccentricity e independently from initial conditions a_0 and e_0 to projected final conditions a_f and e_f. This may be accomplished by a series of thrust-vector reversals at specific points in the orbit.

The independent variation of e while maintaining a constant a is shown as follows. Looking simultaneously at equations (A-19) and (A-20) for $\dot{a}$ and $\dot{e}$; putting them in differential form expressed in equation (A-30), and integrating over one complete revolution while reversing the thrust vector along F_2 at values of eccentric anomaly $E = \pm \pi/2$, i.e., on the minor axis, the results will be

$$\frac{\Delta a}{\Delta t} = 0 \tag{A-37}$$

because any change in a over the first one-half orbit is negated by the reversal of thrust direction over the second half of the orbit. However, the functional form of the equation for $\dot{e}$ upon integration in the precise manner described above produces

$$\frac{\Delta e}{\Delta t} = (\operatorname{sgn} F_2)_{E=0} \frac{4}{\pi} \left(\frac{a}{\mu}\right)^{1/2} (1-e)^{1/2} |F_2| \tag{A-38}$$

which, when integrated over time from an initial eccentricity e_0 to e, yields a time rate of change for e only,

$$e = (\operatorname{sgn} F_2)_{E=0} \sin\left[\frac{4}{\pi} \left(\frac{a}{\mu}\right)^{1/2} |F_2| \, \Delta t + \sin^{-1} e_0\right] \tag{A-39}$$

where $(\operatorname{sgn} F_2)_{E=0}$ is used only to specify an increasing or decreasing eccentricity, i.e., plus or minus e depending on the initial positive or negative F_2 direction at the orbital point $E = 0$.

It is possible, though not necessarily efficient, to vary the semimajor axis a while holding e constant by the similar method just described involving the reversal of the thrust component F_1. This method will not be explained here since for eccentricities less than 0.8 (which is usually the case) it is more optimum to use the F_2 direction steering which gives a maximum change in a [equation (A-32)] plus a simultaneous change in e [equation (A-33)]. Any final adjustments in e needed after the final altitude is reached may be performed as indicated in equation (A-39), which produces a greater magnitude rate change for e than does equation (A-33) with both rates becoming quite small and tending to zero as the orbit becomes more circular.

Independent Secular Variations of Orientation Element Inclination, i, and the Ascending Node, Ω^*

It is apparent from equations (A-22) and (A-24) that only the thrust component orthogonal to the orbital plane in the F_3 direction produces secular changes in either i or Ω^*. It is also possible by reversing the direction of F_3 at specific points in the orbit to vary independently either i or Ω^*.

Using methods previously defined, we can, by reversing the direction of the thrust component F_3 at the points in orbit $\omega^* = \theta + \omega = \pm \pi/2$ and integrating over one complete revolution, obtain for near-circular orbits the composite results,

$$\frac{\Delta i}{\Delta t} = (\operatorname{sgn} F_3)_{\omega^*=0} \frac{2}{\pi} \left(\frac{a}{\mu}\right)^{1/2} |F_3| \qquad \text{(A-40)}$$

and

$$\frac{\Delta \Omega^*}{\Delta t} = 0 \quad . \qquad \text{(A-41)}$$

For more eccentric orbits, additional terms involving e and trigonometric functions of ω become multiplicative factors in equation (A-40).

If F_3 is reversed at the equatorial crossings, i.e., $\omega^* = 0$, we arrive at a new set of composite conditions for i and Ω^* for near circular orbits,

$$\frac{\Delta i}{\Delta t} = 0 \tag{A-42}$$

and

$$\frac{\Delta \Omega^*}{\Delta t} = (\operatorname{sgn} F_3)_{\omega^* = \frac{\pi}{2}} \frac{2}{\pi} \left(\frac{a}{\mu}\right)^{1/2} \frac{|F_3|}{\sin i} \quad . \tag{A-43}$$

A unidirectional F_3 produces simultaneous changes in i and Ω^* but with significantly smaller magnitudes than those shown by equations (A-40) and (A-43).

Simultaneous Adjustment of Semimajor Axis a and Orbital Inclination i

For low-thrust orbit-raising missions that require a plane change, a more efficient way to utilize the available thrust is to maintain a simultaneous inplane F_2 and out-of-plane F_3 component of constant thrust determined by the end conditions which are to be met.

For an out-of-plane steering angle β, we may write the two components of total thrust F_T as

$$F_2 = F_T \cos \beta \tag{A-44}$$

$$F_3 = F_T \cos \beta \quad . \tag{A-45}$$

Equations (A-32) and (A-40) now assume the following forms:

$$\frac{\Delta a}{\Delta t} = \frac{2(1 - e^2)^{1/2}}{n} F_T \cos \beta \tag{A-46}$$

and

$$\frac{\Delta i}{\Delta t} = (\operatorname{sgn} F_T \sin\beta)_{\omega^*=0} \frac{2}{\pi} \left(\frac{a}{\mu}\right)^{1/2} |F_T \sin\beta| \quad . \tag{A-47}$$

Using the differential form of equation (A-27), we obtain

$$\frac{\Delta i}{\Delta a} = \frac{n}{\pi} \frac{\left(\frac{a}{\mu}\right)^{1/2}}{(1-e^2)^{1/2}} \tan\beta \quad , \tag{A-48}$$

which yields, upon integration between the limits i_0 to i and a_0 to a for near-circular orbits,

$$i - i_0 = \frac{\tan\beta}{\mu^{1/2} \pi (1-e^2)^{1/2}} \ln \frac{a}{a_0} \quad . \tag{A-49}$$

An out-of-plane steering angle β may now be determined according to desired end condition changes in a and i. It has been demonstrated by exact optimization methods that a variable out-of-plane steering angle β as a function of spacecraft velocity is optimum for simultaneous orbit raising and plane change.

The functional form is derived to be

$$\sin\beta = \frac{V_0}{V} \sin\beta_0 \quad , \tag{A-50}$$

which, for circular orbits, becomes

$$\sin\beta = \left(\frac{a}{a_0}\right)^{1/2} \sin\beta_0 \quad . \tag{A-51}$$

Thus, from equation (A-49) we arrive at a best-guess β_0 and allow it to vary according to equation (A-51) as the computations for Δa and Δi are made from equations (A-46) and (A-47).

Observe also from equation (A-51) that each succeeding orbital revolution produces a different value of β as the semimajor axis a increases. For low-altitude orbits this increase is small per orbit but for high-altitude orbits, β changes quite rapidly and produces rapid changes in the relative thrust components F_2 and F_3. The magnitudes of F_2 and F_3 are held constant for one revolution; however, the direction of F_3 relative to the plane of the orbit is reversed at the points $\omega^* = \pm \pi/2$.

Secular Variation in the Argument of Perigee

From equation (A-23) we observe that the time rate of change of the perigee point ω is a function of all three components of the perturbing acceleration F_1, F_2 and F_3.

Proceeding as before, we arrive at a rate of change for one revolution by integrating over the eccentric anomaly E with no thrust reversals considered for any component:

$$\frac{\Delta\omega}{\Delta t} = \left(\frac{p}{\mu}\right)^{1/2} F_1 + 3/2 \frac{a\,e}{(\mu p)^{1/2}} \cot i \sin\omega\ F_3 \quad . \tag{A-52}$$

If F_2 is reversed at $E = 0$ and π, we obtain an additional term for the secular variation in ω due to F_2 alone.

$$\frac{\Delta\omega}{\Delta t} = (\operatorname{sgn} F_2)_{E=\frac{\pi}{2}} \frac{2}{\pi} \left(\frac{a}{\mu}\right)^{1/2} \frac{(2-e^2)}{e} |F_2| \quad . \tag{A-53}$$

Further, if F_3 is reversed at $\omega^* = 0$, which is at each equatorial crossing, we have a rate change per revolution only as a function of F_3 which for near-circular orbits becomes

$$\frac{\Delta\omega}{\Delta t} = -(\operatorname{sgn} F_3)_{\omega^* = \frac{\pi}{2}} \frac{2}{\pi} \left(\frac{a}{\mu}\right)^{1/2} \cot i \, |F_3| \quad . \tag{A-54}$$

However, this specific steering profile also produces a $\Delta\Omega^*$ as shown by equation (A-43).

If we measure the flight-path angle γ with respect to the local vertical, i.e., the angle between $\bar{r}$ and $\bar{v}$, we may designate the relative components of the in-plane thrust F_1 and F_2 as

$$F_1 = F_T \cos\gamma \tag{A-55}$$

$$F_2 = F_T \sin\gamma \tag{A-56}$$

which means that F_2 is exactly tangential for circular orbit, i.e., $\gamma = \pi/2$.

Note that it is not necessary to develop specific equations for the time rate of change of the mean anomaly M from equation (A-21) as a function of F_1 and F_2 since our approximation methods mean that at any instant we can compute

$$M = n\,\Delta t \tag{A-57}$$

where t_0 is reckoned from the beginning of each revolution.

A computer program was developed by the author, as referenced in footnote 4, applying the foregoing analyses to the performance and environmental problems associated with earth-orbital low-thrust propulsion mission analyses for a SEPS. The computational results are shown in the previous sections of this report.

APPENDIX B

SHADOWING EFFECTS ON SEPS TRAJECTORIES

When a SEPS passes through the shadow portion of its orbit because of the earth's occultation, the thrust becomes zero since there is no power from the solar arrays at this time. The fractional part of each orbit that a satellite spends in the shadow is a function of the orbital parameters and the position of the sun with respect to the earth. Precise calculation of this shadow time requires intricate analyses; however, using certain stated assumptions, we may calculate with very good accuracy the resulting thrust losses for each revolution of our low-thrust trajectory and thereby assess the effects on performance of the vehicle as a result of this occurrence.

From Figure B-1 we observe that maximum shadow chord C_s is simply

$$\max C_s = 2 r_E \quad , \tag{B-1}$$

where r_E is the earth's radius. This maximum occurs when the sun lies in the orbit plane.

The minimum shadow chord occurs when the sun is 90 deg from the line of nodes formed by the orbit and the ecliptic planes. From the shadow chord geometry of Figure B-1, we observe a trivial solution of

$$\min C_s = 0 \qquad \text{if} \qquad r_s \sin I > r_E \quad ,$$

i.e., no shadowing when the component of the satellite altitude with respect to the perpendicular to the ecliptic is greater than the radius of the earth. However, if this component is less than or equal to the radius of the earth ($r_s \sin I \leq r_E$), the following trigonometric relationship holds and a functional relationship for a minimum shadow chord becomes apparent:

$$a^2 \sin^2 \theta \sin^2 I = r_E^2 - a^2 \cos^2 \theta \tag{B-2}$$

where I is defined as the angle between the orbital and ecliptic planes.

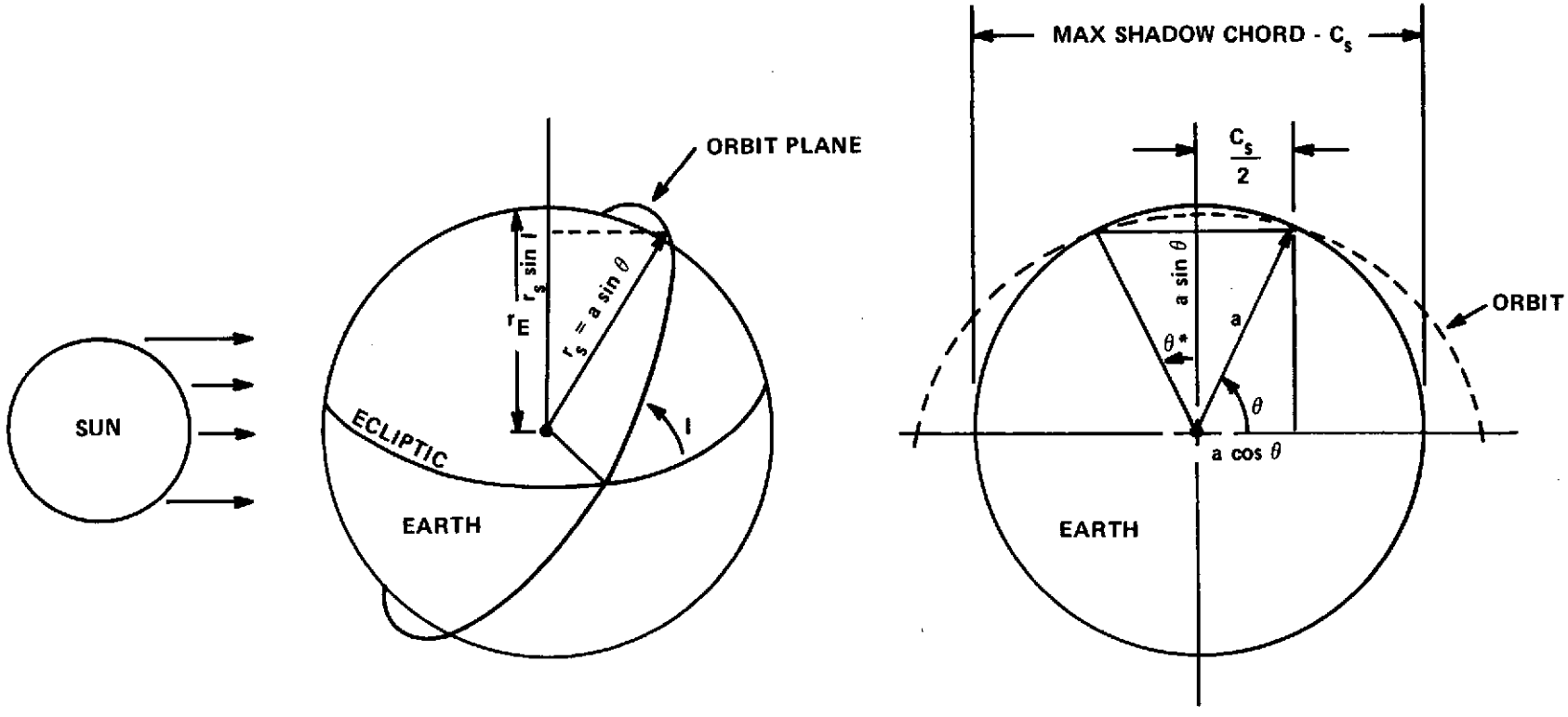

$$\min C_s = 0$$

$$\min C_s = 2\, a \cos\theta = 2\, \frac{\left(r_E^2 - a^2 \sin^2 I\right)^{1/2}}{\cos I}$$

if $r_s \sin I > r_E$

if $r_s \sin I \leq r_E$

$$\max c_s = 2\, r_E$$

Figure B-1. Shadow chord geometry.

Equation (B-2) simplifies to

$$2a \cos\theta = \min C_s = 2 \frac{(r_E^2 - a^2 \sin^2 I)^{1/2}}{\cos I} \quad \text{if} \quad r_s \sin I \leq r_E \quad . \tag{B-3}$$

A simplified average value for the angle I is often applied but we can compute a functional form for calculating I using the coordinate system shown in Figure A-1.

We may define an inertial reference frame or transformation between the orbital plane and the ecliptic plane by performing one additional positive rotation about the X-axis through the ecliptic angle ϵ to the transformation shown in Figure A-1 and matrix equation (A-9) of Appendix A. This gives

$$\begin{pmatrix} \bar{x}_0 \\ \bar{y}_0 \\ \bar{z}_0 \end{pmatrix} = \begin{pmatrix} A_{11} & A_{12} & A_{13} \\ A_{21} & A_{22} & A_{23} \\ A_{31} & A_{32} & A_{33} \end{pmatrix} \begin{pmatrix} 1 & 0 & 0 \\ 0 & \cos\epsilon & \sin\epsilon \\ 0 & -\sin\epsilon & \cos\epsilon \end{pmatrix} \begin{pmatrix} \bar{i}_\epsilon \\ \bar{j}_\epsilon \\ \bar{k}_\epsilon \end{pmatrix} \tag{B-4}$$

where $\bar{i}_\epsilon$, $\bar{j}_\epsilon$, and $\bar{k}_\epsilon$ are orthogonal ecliptic system unit vectors. Now the angle I between the orbital plane and the ecliptic plane may be defined simply as the angle between their perpendiculars whose direction cosine is given by the matrix element

$$\bar{k}_0 \cdot \bar{k}_\epsilon = \cos I = A_{32} \sin\epsilon + A_{33} \cos\epsilon \tag{B-5}$$

and

$$\cos I = \sin i \cos \Omega^* \sin\epsilon + \cos i \cos\epsilon \quad . \tag{B-6}$$

Obviously, angle I is a function of the orientation elements i and Ω^* which produces a periodic variation in the magnitude of I as well as an initial magnitude difference, depending on the relative launch time each day.

Computing a minimum shadow chord from equation (B-3) we may now complete the calculation for the dimensionless fraction of the spacecraft's shadow time per revolution.

From Figure B-1,

$$\sin \theta^* = \frac{C_s}{2a} \tag{B-7}$$

$$\frac{\theta^*}{\pi} = \frac{1}{\pi} \sin^{-1} \frac{C_s}{2a} \tag{B-8}$$

where C_s is the $\min C_s$ as calculated from equation (B-3) or because of the varying positions of the sun with respect to the orbital plane, C_s may be defined as an average rate,

$$C_s = \frac{\max C_s + \min C_s}{2} \tag{B-9}$$

Using the above-described methods, the average fractional shadow portion and subsequent loss thrust time per revolution for a SEPS is computed to be approximately 35 percent (35 min) at an altitude of 463 km (250 n. mi.), 25 percent (30 min) at 1852 km (1000 n. mi.), and 5 percent (22 min) at a projected Tug/SEPS changeover altitude of 14 000 km (7500 n. mi.).

REFERENCES

1. Carter, J. R.; and Tada, H. Y.: The Solar Cell Radiation Handbook. Report No. 21945-6001-RU-00, JPL Contract No. 953362, TRW Systems Group, Redondo Beach, Calif., June 28, 1973.

2. Gaddy, E. M.: Flight Qualification Test Results for Violet Cells. Tenth IEEE Photovoltaic Specialists Conference Record, Palo Alto, Calif., November 1973, pp. 153-162.

3. Curtin, D. J.; and Cool, R. W.: Qualification Testing of Laboratory Produced Violet Solar Cells. Tenth IEEE Photovoltaic Specialists Conference Record, Palo Alto, Calif., November 1973, pp. 139-152.

4. Watts, J. W., Jr.; Burrell, M. O.; and Wright, J. J.: Charged Particle Radiation Environment for the LST. NASA TM X-64858, May 1974.

5. McGlathery, D. M.: Space Shuttle Rendezvous, Radiation, and Reentry Analysis Code. NASA TM X-64768, May 16, 1973.

6. Vette, J. I., et al.: Models of the Trapped Radiation Environment. NASA SP-3024, vol. 4-6, 1970.

7. Vette, J. I.; and Singley, G. W.: The AE-4 Model of the Outer Radiation Zone Electron Environment. Report No. NSSDC 72-06, National Space Science Data Center, Goddard Space Flight Center, Greenbelt, Md., August 1972.

8. Horne, W. E.; and Wilkinson, M. C.: Research Study on High Energy Radiation Effects and Environment — Solar Cell Degradation Methods. Boeing Report No. D180-18475 (NASA Contract NAS8-30378), The Boeing Co., Seattle, Wash., Oct. 24, 1974.

9. Burrell, M. O.: The Risk of Solar Proton Events to Space Missions. NASA TN D-6600, June 1971.

10. Divine, T. N.: Interplanetary Charged Particle Environments. JPL TM 33-637, Aug. 1, 1973.